

STRUCTURE AND DYNAMICS STUDIES USING NUCLEAR MAGNETIC
RESONANCE: FROM SIMPLE LIQUIDS TO EXTREME NETWORKS

Leah Marie Heist

A dissertation submitted to the faculty at the University of North Carolina at Chapel Hill in
partial fulfillment of the requirements for the degree of Doctor of Philosophy in the
Department of Chemistry.

Chapel Hill
2015

Approved by:
Edward T. Samulski
James W. Jorgenson
Louis A. Madsen
Sergei S. Sheiko
R. Mark Wightman

© 2015
Leah Marie Heist
ALL RIGHTS RESERVED

ABSTRACT

Leah Marie Heist: Structure and Dynamics Studies Using Nuclear Magnetic Resonance:
From Simple Liquids to Extreme Networks
(Under the direction of Edward T. Samulski)

Nuclear magnetic resonance is a powerful analytical tool utilized by chemists and biochemists to extract structural information. However, NMR has utility beyond structure determination: it is also a powerful technique for interrogating dynamics at the microscopic level. In this thesis, I have used NMR to study a diverse range of fluid systems:

- liquid state structure in molecular liquids using very high field NMR
- orientational order in nonlinear liquid crystal dimers
- molecular dynamics and structure in highly grafted “bottle-brush polymers”
- high performance liquid crystal thermosetting polymers.

NMR detects small changes in the magnetic energy of nuclei in different environments. With the advent of very-high field NMR spectrometers (i.e. 800, 950, and even 1000 MHz in recent years), extremely subtle interactions between nuclei and the magnetic field can be detected—interactions that are largely averaged out due to isotropic motion in lower field spectrometers. In Chapter 2, very high field NMR is exploited to measure field-induced nuclear quadrupolar interactions for prototypical molecular liquids. By measuring the field-induced biasing of molecular motion, it is possible to experimentally determine the leading tensor component of the pair correlation function in liquids, which provides a critical test of molecular dynamics simulation force fields.

The incompletely averaged, anisotropic NMR interactions described in Chapter 2 for simple isotropic liquids are significant for anisotropic molecules (liquid crystals). One type of liquid crystal, the nematic phase, is characterized by molecules that tend to align their long axis on average parallel to one another in the fluid, but have no spatial correlations—no positional order. In Chapter 3, I attempt to describe the nature of a new nematic phase found in nonlinear liquid crystal dimers, introduced in 1991 by Hiro Toriumi, professor of chemistry at Tokyo University, by supplementing recent simulation data from Photinos and coworkers at the University of Patras with extensive ^2H and ^{13}C NMR studies.

In Chapters 4 and 5, NMR studies on two very diverse soft matter networks are outlined: very soft, room temperature bottle-brush polymer networks and very tough high temperature ($>300^\circ\text{C}$) liquid crystal thermosets.

ACKNOWLEDGMENTS

My time at UNC has truly been a rewarding experience and I want to begin by thanking just some of the numerous people who have helped me along the way. First, I owe immense gratitude to my research advisor and mentor, Prof. Edward Samulski, who provided a wonderful environment to conduct research, constantly encouraged me to pursue my own ideas, and was always eager to discuss my results. Ed's extraordinary ability to think, write, and communicate science made him a wonderful mentor and he encouraged me to live up to this high standard. I also want to thank Ed's wife, Carol (an extraordinary writer and communicator herself), for her friendship and invaluable advice over the years. Additionally, my gratitude goes to my committee members Prof. Sergei Sheiko, Prof. James Jorgenson, and Prof. Mark Wightman who provided me with thoughtful suggestions and insights. I am glad to have Prof. Louis Madsen (Virginia Tech) join my committee; he generated my excitement for NMR and liquid crystals and as an undergraduate he made me feel like an invaluable member of his lab.

At Virginia Tech I also had the privilege of being a member of Prof. Webster Santos' lab. I want to thank him for being the first person to encourage me to do research and giving me a great experience in his lab. I also want to thank my high school chemistry teacher, Mrs. Stromwall. She was a compassionate teacher and I always loved going to her class.

I would not have been able to conduct my research without the help of the research facility directors at UNC who were always eager to lend their expertise to advance my projects, specifically, Dr. Marc TerHorst (NMR) for his patience and immense knowledge in

the intricacies of NMR and Collin McKinney (Electronics) for his many hours helping me set up a power supply for my high temperature NMR probe. I also want to thank Dr. Kevin Knagge (DHMRI) for helping to secure high field NMR data.

To the many collaborators that I have worked with during my time here: I want to thank you for your scientific curiosity and for enriching my knowledge in a wide range of topics: Prof. Demetri Photinos (University of Patras), Prof. Chi-Duen Poon (UNC), Prof. Jim Emsley (Southampton), Prof. Jukka Jokisaari (Oulu), and Prof. Moreno Lelli (ENS Lyon). Many people provided samples and were invaluable resources to me: Georg Mehl (Hull) who provided the cyanobiphenyl dimer samples and Krzysztof Matyjaszewski and Joanna Burdyńska who synthesized the labeled bottlebrushes. Lastly, to Theo Dingemans (TU Delft), an exceptional polymer chemist, who provided all the liquid crystal and LCT samples and who agreed to be on my orals committee.

Most importantly, I want to thank all of my family and friends who have been important parts of my life. Amy, thank you for being my best friend since the 2nd grade. Sarah, I am so glad we both decided to join the chemistry fraternity so we could become great friends. To my grandparents, thank you for your love and support and for being such a large part of my life. To my parents, I owe so much of my success to you for being a great example and for always wanting the best for me. Thank you for loving me and always giving me the confidence to pursue my dreams. To my husband, Chris, I am so blessed to have you in my life and I cannot wait to see what the future brings us. Thank you for always supporting and encouraging me in everything I do.

TABLE OF CONTENTS

LIST OF TABLES	xi
LIST OF FIGURES	xii
CHAPTER 1: INTRODUCTION	1
1.1 Introduction.....	1
1.2 Liquid Crystals.....	1
1.3 Polymer Networks	2
1.4 NMR Theory (Nuclear Spin Hamiltonian)	3
1.4.1 Quadrupolar Interaction	4
1.4.2 Spin Relaxation.....	5
1.4.3 Chemical Shift	7
CHAPTER 2: LIQUID STATE STRUCTURE VIA VERY HIGH-FIELD NMR.....	9
2.1 Introduction.....	9
2.2 High Field ^2H NMR Magnetic Field Induced Alignment of Deuterated Liquids..	11
2.2.1 ^2H NMR of Benzene at 1 GHz.....	15
2.3 Relation of Order Parameters to Molecular Pair Correlations in a Liquid in a High Magnetic Field	19
2.4 Evaluation of Correlation Factors from Measured Spectra	23
2.4.1 Binary mixtures (Case 1)	24
2.4.1.1 Benzene in TMS	26
2.4.1.2 Chloroform in TMS	27
2.4.2 Tertiary mixtures (Case 2)	29

2.4.2.1 Benzene:hexafluorobenzene 1:1 mixture in TMS	30
2.4.2.2 Chloroform:benzene 1:1 mixture.....	32
2.4.3 Binary mixtures (Case 3)	33
2.4.3.1 Thiophene in TMS	33
2.5 Calculated correlation factors from molecular dynamics simulations.....	35
2.5.1 Benzene-benzene pair correlations	35
2.5.2 Chloroform-chloroform pair correlations	39
2.5.3 The benzene/hexafluorobenzene complex	40
2.5.4 Insights from chloroform-d/benzene mixtures.....	43
2.6 Conclusions	44
CHAPTER 3: N _x PHASE OF CYANOBIPHENYL DIMERS	46
3.1 Introduction.....	46
3.1.2 Chiral phases	48
3.1.3 Nematic phases of non-linear cyanobiphenyl dimers	49
3.1.4 Experimental determination of the twist-bend nematic phase.....	51
3.1.4.1 Microscopy (FFTEM, Optical Microscopy)	51
3.1.4.2 Elastic constants in nematic phases	53
3.1.4.3 Experimental determination of chirality	55
3.1.5 An alternative structure for the N _x phase of odd cyanobiphenyl dimers	56
3.2 Experimental Methods	60
3.2.1 Materials	60
3.2.2 NMR Methods	61
3.3 Results and Discussion	62
3.3.1 ² H NMR of Liquid Crystals	62

3.3.2 Deuterated probes dissolved in liquid crystals.....	62
3.3.3 Comparison with chiral nematics.....	68
3.3.4 Demonstration of the odd-even effect of cyanobiphenyl dimers	70
3.3.5 Core order parameters.....	71
3.3.6 Direct determination of S_{core} using the chemical shift anisotropy of ^{13}C	72
3.3.7 ^{13}C NMR of cyanobiphenyl dimers	74
3.4 Conclusions.....	78
CHAPTER 4: LOCAL DYNAMICS OF BOTTLEBRUSH MACROMOLECULES VIA ^2H NMR	80
4.1 Introduction.....	80
4.2 Experimental Methods	82
4.2.2 NMR Methods	83
4.3 Results and Discussion	85
4.3.1 Solution Dynamics in Bottlebrush Backbone	85
4.3.2 Solution Dynamics in Bottlebrush Macromolecules	88
4.3.3 Bottlebrush Dynamics Inferred from NMR Linewidths	90
4.4 Conclusion	94
CHAPTER 5: LIQUID CRYSTAL THERMOSETS: HIGH PERFORMANCE THERMOSET RESINS	96
5.1 Introduction.....	96
5.1.1 High Performance Polymers	96
5.1.2 Current Polymer Matrix Composites	98
5.1.3 High Performance Thermosets	98
5.1.3.1 Liquid Crystal Thermosets.....	99
5.1.4. Curing of phenylethynyl based systems	101
5.2 NMR Methods	101

5.2.1 Solid State ^{13}C NMR.....	104
5.3 Results and Discussion	108
5.3.1 Solid-State Spectra of LCT oligomer precursor	108
5.3.2 NMR of Liquid Crystal Thermosets	112
5.3.2.1 Chemical Shift Anisotropy in Liquid Crystals.....	116
5.3.3. Exploitation of Chemical Shift Anisotropy in LCTs	122
5.3.3.1 LCT Model Compounds	123
5.3.2 Curing Kinetics	124
5.4 Conclusions.....	127
APPENDIX A: TABLES OF ^2H AND ^{13}C NMR DATA OF CYANOBIIPHENYL DIMERS	128
REFERENCES	136

LIST OF TABLES

Table 2.1. Quadrupolar splitting and $\Delta(\Delta\nu)$ for Figures 2.1-3.	18
Table 2.2. Constants used in the determination of correlation factors for benzene, chloroform, and thiophene.	24
Table 2.3. Calculated radial integral of leading tensor component of $g(\omega_1\omega_2r)$ with typical experimental constants used to discriminate force fields (ΔH_{vap} , density, and diffusion coefficient, D) for benzene.	36
Table 4. Results of toy model for benzene.	38
Table 2.4. Calculated radial integral of leading tensor component of $g(\omega_1\omega_2r)$ with typical experimental constants used to discriminate force fields (ΔH_{vap} , density, and diffusion coefficient, D) for chloroform.	39
Table 3.1. Calculated values of a and b in ppm for each ^{13}C nucleus in the phenyl rings and CN group of 5-CB.	74
Table 4.1. Relaxation data for decreasing concentrations of BBBs (Br_{600})-d ₄	87
Table 4.2. T_1 and T_2 data and calculated correlation times for (600-g-44)-d ₄	90

LIST OF FIGURES

Figure 1.1. Three categorical shapes: calamitic, nonlinear, and discotic, representing liquid crystals with primary structures, secondary structures, and idealized shapes.	2
Figure 2.0. Some contents of this chapter and additional information appear in two publications in <i>Journal of Magnetic Resonance</i> and <i>Journal of Physical Chemistry Letters</i>	9
Figure 2.1. The molecular axes system for benzene, chloroform, and thiophene.	15
Figure 2.2. ^2H spectra at 153.553 MHz of neat C_6D_6	16
Figure 2.3. $^2\text{H} - \{^1\text{H}\}$ spectrum at 153.553 MHz of deuterium nuclei present at natural abundance in neat C_6H_6	18
Figure 2.4. Observed $\Delta\nu/\nu_0$ versus x , the mole fraction of benzene- d_6 and chloroform- d in the diluent TMS	26
Figure 2.5. ^2H NMR spectrum of neat benzene- d_6 recorded at 22.3 T (Bruker Avance III 950 MHz proton NMR spectrometer at temperature, $T = 303$ K).	27
Figure 2.6. ^2H NMR spectrum of neat chloroform- d recorded at 22.3 T (Bruker Avance III 950 MHz proton NMR spectrometer at temperature, $T = 303$ K).	29
Figure 2.7. Observed $\Delta\nu/\nu_0$ versus x , the mole fraction of benzene- d_6 and hexafluorobenzene diluent TMS	30
Figure 2.8. ^2H NMR spectrum of neat 1:1 mixture of benzene- d_6 /hexafluorobenzene (no TMS) recorded at 22.3 T (Bruker Avance III 950 MHz proton NMR spectrometer at temperature, $T = 303$ K).	31
Figure 2.9. ^2H NMR spectrum of neat 1:1 mixture of chloroform- d /benzene (no TMS) recorded at 22.3 T (Bruker Avance III 950 MHz proton NMR spectrometer at temperature, $T = 303$ K).	32
Figure 2.10. ^2H NMR spectrum of thiophene- d_4 (deuterons 6,9 and 7,8 labeled) recorded at 22.3 T (Bruker Avance III 950 MHz proton NMR spectrometer at temperature, $T = 303$ K).	34
Figure 2.11. Concentration dependence of thiophene pair correlation factors versus x , the mole fraction of thiophene- d_4 in TMS.	35
Figure 2.12. Spatial distribution function of benzene calculated with MD simulation using the AMOEBA force field. The two most probable dimer states are mutually perpendicular ring planes (T) and parallel ring planes (P).	37

Figure 2.13. The four possible dimer configurations for two benzene molecules.	38
Figure 2.14. Spatial distribution function of chloroform calculated with MD simulation using the AMOEBA force field. The two most probable dimer states are parallel ($\theta_{1,2} = 0^\circ$) and antiparallel ($\theta_{1,2} = 180^\circ$).	40
Figure 2.15. Schematic representation of the crystal structure between (a) identical quadrupolar molecules and (b) two quadrupolar molecules with opposite quadrupole moment configurations	41
Figure 2.16. Spatial distribution function of chloroform calculated with MD simulation using the AMOEBA force field. The most probable dimer state is overwhelming parallel ($\theta_{1,2} = 0^\circ$).	43
Figure 3.1. Examples of phases formed from calamitic mesogens: uniaxial nematic (N), uniaxial smectic-A (S_A) and biaxial smectic-C (S_C).	47
Figure 3.2. Examples of phases formed from discotic mesogens: nematic (D_N), hexagonal ordered (D_{ho}), and hexagonal disordered (D_{hd}).	48
Figure 3.3. Approximate shape of a non-linear liquid crystal dimer and structure of CB-C7-CB.	49
Figure 3.4a. Uniaxial nematic phase, N, b. twist-bend nematic phase, N_{TB} , and c. chiral nematic phase, N^*	51
Figure 3.5a. Schierlen texture of the uniaxial nematic phase of a liquid crystal (N) b. Focal conic texture of the chiral nematic phase of a liquid crystal (N^*) when viewed under a polarizing optical microscope	53
Figure 3.6. Structure and phase transition map for M2.	54
Figure 3.7. Prochiral molecule where X and Y substituents are different.	55
Figure 3.8. AFM images of (left) the N_X phase showing a focal conic domain covered with layers spaced ~ 8 nm apart with the crystallographic structure (right) the crystalline phase showing clear evidence of 8.3 nm periodicity of the crystallographic planes. .	57
Figure 3.9a. 2H NMR of the N_X phase of deuterated CB-C9-CB (pictured) before (red) and immediately after (blue) rotation of the sample by 90° . b. A hypothetical picture of the proposed twist-bend confirmation undergoing a rotation by 90°	59
Figure 3.10. Chemical structure and respective transition temperatures of CB-Cn-CB for $n=7,8,9,10,11,12$, taken from the first DSC heating scans and cooling scans (10 Kmin^{-1}).	60
Figure 3.11. 2H NMR Quad echo pulse sequence.	61

Figure 3.12. Inverse gated ^1H decoupled ^{13}C NMR pulse sequence.....	62
Figure 3.13. ^2H NMR spectra of decane- d_{22} in CB-C11-CB at decreasing temperatures	63
Figure 3.14. The temperature dependence (in reduced temperature) of the quadrupole splitting of the methyl and methylene group of decane- d_{22} in CB-C11-CB	64
Figure 3.15. ^2H NMR spectra of decane- d_{22} in CB-C9-CB at decreasing temperatures	65
Figure 3.16. The temperature dependence (in reduced temperature) of the quadrupole splitting of the methyl and methylene group of decane- d_{22} in CB-C9-CB	65
Figure 3.17. ^2H NMR spectra of decane- d_{22} in CB-C7-CB at decreasing temperatures	66
Figure 3.18. The temperature dependence (in reduced temperature) of the quadrupole splitting of the methyl and methylene group of decane- d_{22} in CB-C7-CB	67
Figure 3.19. A possible arrangement of mesogenic units within each chiral domain for odd cyanobiphenyl dimers.	68
Figure 3.20. ^2H spectra of 2 wt% decane- d_{22} dissolved in cholesteryl nonanoate (CN) cooled into the smectic phase and heated to access the cholesteric phase	69
Figure 3.21. The temperature dependence (in reduced temperature) of the quadrupole splitting of the α -methylene group of decane- d_{22} in all samples including the monomer, 5-CB and the even dimer, CB-C10-CB.	71
Figure 3.22. ^{13}C spectra of CB-C11-CB at decreasing temperature with ^1H decoupling.	75
Figure 3.23. ^{13}C spectra of CB-C11-CB at decreasing temperature without ^1H decoupling.	76
Figure 3.24. The temperature dependence (in reduced temperature) of the order parameter of CN in CB-C11-CB, CB-C9-CB, CB-C7-CB, and the monomer 5-CB.....	77
Figure 3.25. ^{13}C NMR of CB-C10-CB in the nematic phase.....	78
Figure 4.1. Schematic diagram of bottlebrush macromolecule (BBM) showing label in backbone, grafted “bristles” and “hair” on each of the bristles.	81
Figure 4.2 The synthetic pathway for the preparation of a. ATRP diinitiator- d_4 ($\text{Br}-\text{d}_4-\text{Br}$) and b. labeled BBMs and PnBA side chains ((600-g-5/44)- d_4).....	83
Figure 4.3. Inversion recovery pulse sequence. Values of τ are varied for measuring the spin-lattice relaxation time, T_1	84
Figure 4.4. Car-Purcel-Meiboom-Gill (CPMG) pulse sequence. Values of n are varied for measuring the spin-spin relaxation time, T_2	84
Figure 4.5. ^2H NMR Quad echo pulse sequence.....	85

Figure 4.6. ^2H 1D NMR spectra of (Br_{600})- d_4 (0.09g/mL in DCM), (600- <i>g</i> -5)- d_4 (10 wt% in DCM), and (600- <i>g</i> -44)- d_4 (12 wt% in DCM).	87
Figure 4.7. Experimental data for determination of T_1 (a) and T_2 (b) for three concentrations of BBB. Shaded line represents the estimated error in the exponential fit.	88
Figure 4.8. Experimental and simulated spectra of the bottle-brush (600- <i>g</i> -44)- d_4 in DCM. 92	
Figure 4.9. Experimental and simulated spectra of the neat bottle-brush (600- <i>g</i> -5)- d_4	94
Figure 5.1a. All-aromatic high performance polymers and b. melt processable high performance polymers.	97
Figure 5.2 The LCP Vectra TM	99
Figure 5.3 LCT reactive oligmer.....	100
Figure 5.4. Liquid crystal thermoset a. before and b. after curing with preferred direction along n.	100
Figure 5.5. ^1H broadband decoupling ^{13}C NMR pulse sequence using cross polarization..	102
Figure 5.6. ^1H broadband decoupled ^{13}C pulse sequence.	103
Figure 5.7. Home-built oven for ^{13}C NMR probe capable of reaching over 400°C.	104
Figure 5.8. ^{13}C powder pattern of the LCT precursor oligomer	105
Figure 5.9. Representative, idealized spectra from single crystals with one orientation (left) and powders with random orientations (right). From ref 3.....	106
Figure 5.10. ^{13}C NMR spectra of the LCT oligomer.	108
Figure 5.11. ^1H broadband decoupled ^{13}C CP/MAS spectrum of a. HBA, b. HNA, c. PE-COOH, and d. PE-OAc.....	110
Figure 5.12. Sum of ^{13}C CP/MAS spectra of HBA, HNA, PE-COOH, and PE-OAc (scaled to ratios of monomers and end-groups).	111
Figure 5.13. Overlay of Figures 5.12 (sum, blue) and 5.10 (red).	112
Figure 5.14. Simplified picture of a liquid crystal polymer melt before and after a magnetic field is applied.....	113
Figure 5.15. Proposed di- ($f = 2$) and tri- ($f = 3$) functionalized cure products of the phenylethynyl end-group chemistry.	114
Figure 5.16. ^{13}C NMR spectra of 1000 g/mol LCT precursor. Isotropic CP/MAS (red) Oriented 250°C (blue).....	116

Figure 5.17. ^1H decoupled ^{13}C spectra of TBBA in the isotropic phase and various oriented phases.....	117
Figure 5.18. ^1H decoupled ^{13}C spectra of TBBA in the nematic phase using different ^1H decoupling schemes.	119
Figure 5.19. Proton-decoupling ^{13}C NMR of 5-CB in the isotropic and nematic phases....	120
Figure 5.20. Dimethylacetylene structure and axes system with the z -axis along the acetylene bond.....	121
Figure 5.21. ^{13}C spectra of DPDA-OC ₅ in the nematic and isotropic phases.....	122
Figure 5.22. ^{13}C NMR of LCT after curing at 300°C for 75 min for various time intervals	123
. A qualitative loss of the ethynyl carbon peak intensity is observed.	123
Figure 5.23. CP/MAS (isotropic) spectrum in red and oriented (anisotropic) spectrum in blue of the PE-napthalenediol-PE model compound.....	124
Figure 5.24. ^{13}C NMR of LCT precursor model compound (PE-napthalenediol-PE). Different durations of curing in minutes at 300°C and plot of concentration of ethynyl peak vs. cure time used to determine kinetic rate constants.	125
Figure 5.25. Kinetic plot of the natural log of concentration vs. cure time in minutes. First-order rate constants are found from linear fits to the data.	126

CHAPTER 1: INTRODUCTION

1.1 Introduction

Nuclear magnetic resonance (NMR) is a powerful analytical tool for studying a wide range of materials from simple liquids to complicated polymer structures and architectures both in solutions and in the solid state. Additionally, NMR provides information about structure as well as dynamics over various length and time scales.¹ In this thesis, the attributes of NMR are clearly demonstrated by studies of four very different materials: simple liquids like benzene and chloroform, nematic liquid crystals, and extreme polymer networks: very tough liquid crystal thermosets and very soft bottlebrush elastomers. A brief description of the materials considered in this thesis and the underlying NMR theory used is described.

1.2 Liquid Crystals

Liquid crystals differ from normal isotropic liquids in that they possess some degree of orientational order or anisotropy. Fluid phases can be liquid crystalline with or without translational order whereas crystal phases contain both translational and orientational order. Liquid crystalline molecules have shape anisotropy and molecular shape determines long-range ordering. Molecular shapes can be categorized into (1) calamitic or rod-shaped, (2) discotic or disk-shaped, or (3) non-linear or bent-shaped as depicted in Figure 1.1 and each shape type can further be categorized into a hierarchy of fluid phases (i.e. nematic).²

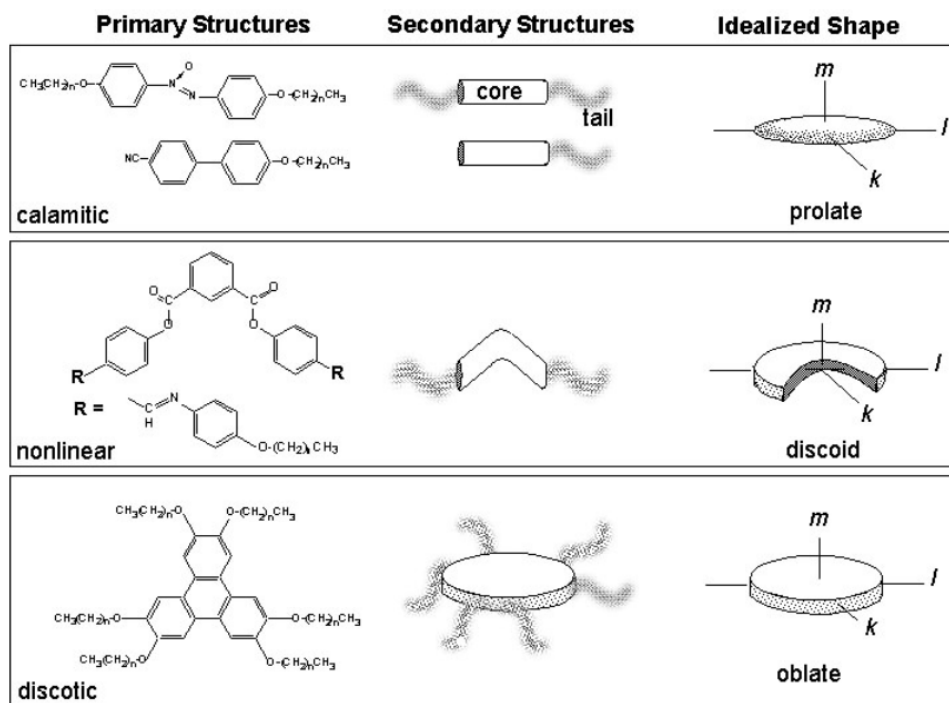


Figure 1.1. Three categorical shapes: calamitic, nonlinear, and discotic, representing liquid crystals with primary structures, secondary structures, and idealized shapes. From ref 2.

The most is known about phases formed from the two extreme shapes: calamitic and discotic. The primary structure is characterized by a mesogenic core, typically made up of aromatic groups, that facilitates into a fluid phase by lowering the melting temperature, T_m . The symmetry axis of the meson is represented by **l**. The symmetry axis of the fluid is termed the director, **n**. These primary molecular shapes can organize into a variety of fluid phases and some are discussed in Chapter 3 and a new nematic phase is explored.

1.3 Polymer Networks

Polymer networks are the result of a transition from a liquid to solid state through the formation of cross-links between polymer chains. Cross-links can be covalent, like in a thermoset, where a particular reaction takes place that creates bonds between polymer chains. Alternatively, physical cross-linking, in which no covalent bonds are made, can occur when ionic groups cluster (ionomers), semicrystalline polymers crystallize, and when amorphous,

flexible polymer chains form entanglements with their neighbors. The formation of either physical or chemical cross-links between polymer chains is generally known as gelation and results in a three-dimensional interconnected “single” macromolecule or network. The strength of these interactions determines the mechanical properties of the network. A typical property used to measure the “stiffness” is the shear modulus which describes the material’s response to shearing strains and is in units of pressure (force per sheared area). Liquids have a zero shear modulus and metals can have moduli up to hundreds of GPa. The modulus of polymeric materials falls in the middle of these two extremes; polymer networks are tailored to have moduli specific for a desired application. In Chapter 4, bottlebrush architectures forming super-soft (low modulus) elastomers are described and in Chapter 5, super-tough (high modulus) liquid crystal thermosets are described.

1.4 NMR Theory (Nuclear Spin Hamiltonian)

Nuclear spin interactions give rise to a breadth of information about chemical structure, chemical processes, and dynamics of molecules. These interactions are probed using NMR and will be used in the study of the two aforementioned polymer systems.

The quantum mechanical description of NMR uses the spin Hamiltonian to describe the various interactions involved when a sample is subjected to an external magnetic field. When this external field, \mathbf{B}_0 , is applied, the energy of the nuclear magnetic moments is perturbed. The spin Hamiltonian describes these changes in energy. The external spin Hamiltonian is purely magnetic and describes interactions between the spin system and the external magnetic field. This field causes the nuclear Zeeman splitting which splits spin quantum states that are normally degenerate.

$$\hat{H}_j^{\text{internal}} = \hat{H}_j^{CS} + \hat{H}_j^Q + \hat{H}_{jk}^{DD} + \hat{H}_{jk}^J \quad (1.1)$$

The internal spin Hamiltonian (Equation 1.1 for spin j interacting with spin k) is much more complicated because it involves all other spin interactions with its environment and other spins. These include the chemical shift (CS), which attenuates the external magnetic field through the motion of the electrons in the field. The quadrupolar coupling (Q) is a result of the interaction of a quadrupolar nucleus and the local electric field gradient formed by electrons in the chemical bond to quadrupolar nuclei. Direct dipole-dipole couplings (DD) are caused by the direct magnetic interaction of nuclear spins through space. Finally, the J-coupling (J), or indirect dipole-dipole coupling, involves the spin interactions through the bonding electrons.³

1.4.1 Quadrupolar Interaction

The nuclear quadrupole coupling manifests itself in ^2H NMR; deuterium has a spin quantum number of 1. The nuclear quadrupole moment of the ^2H nucleus (D) strongly interacts with the electric field gradient generated by the surrounding electron clouds (primarily the C—D bonding electrons), making it a purely intramolecular interaction. The relevant parameter is the quadrupole moment of the nucleus, which for ^2H is $0.2860 \times 10^{-28} \text{ m}^2$ and small enough to be observed by NMR (as opposed to nuclear quadrupole spectroscopy).

The first order nuclear quadrupole Hamiltonian for ^2H (spin, $I=1$) is given in terms of ω_Q (Equation 1.2).³ It is important to note that in many NMR descriptions, energies are given in natural (or angular frequency) units indicated by ω while units of Hz are usually specified by ν where $\nu = \omega/2\pi$.

$$\begin{aligned}\hat{H}_j^Q &= \omega_Q \frac{1}{6} (3\hat{I}_z^2 - 2) \\ \omega_Q &= \frac{3eQ\overline{V_{zz}}}{2\hbar}\end{aligned}\tag{1.2}$$

The ω_Q term is averaged over all molecular motion, so it averages to zero in isotropic liquids. Therefore, the Hamilton is zero and it does not influence the position of the NMR peaks in isotropic liquids. The quadrupolar interaction does, however, strongly influence the relaxation of nuclear spins. The relaxation for ^2H nuclei is solely influenced by the quadrupole interaction, which is purely intramolecular. Because the natural abundance of ^2H is so low ($\sim 0.015\%$), molecules are usually labeled with ^2H at particular hydrogen positions to probe molecular dynamics by the reorientations at those labeled positions.³

1.4.2 Spin Relaxation

By ^2H -labeling, the dynamics of local motion can be probed at the site of the C—D bond. This technique is used to study dynamics in polymer bottlebrushes (Chapter 4). And, by considering some simple theoretical relations, relaxation can give information about this local motion.

Spin relaxation proceeds by two different mechanisms. When an external magnetic field is introduced (\mathbf{B}_0), the spins reach thermal equilibrium where there is a slight preference for the lower energy spin state caused by the Zeeman splitting. This causes a slight excess of magnetization parallel to the external magnetic field, which is defined to be the z -axis. When spins are subjected to this external magnetic field, they begin to precess at the Larmor frequency, ω_0 , which is linearly related to the magnetic field strength (Equation 1.3) where γ is the gyromagnetic ratio (ratio of the magnetic moment of the nucleus to its angular momentum) in units of $\text{rad s}^{-1} \text{ T}^{-1}$.⁴

$$\omega_0 = \gamma B_0 \quad (1.3)$$

The slight excess in magnetization in the positive z -direction is given by the Boltzmann distribution (Equation 1.4).³

$$\frac{N_{lower}}{N_{upper}} = e^{\frac{\Delta E}{kT}} = e^{\frac{\hbar \gamma B_0}{kT}} \quad (1.4)$$

The spin lattice relaxation characterizes the evolution of the spin populations to thermal equilibrium in the presence of the field. It is the buildup of longitudinal spin excess population and is described by the time constant, T_1 . T_1 is measured by an NMR experiment known as inversion recovery in which a radiofrequency pulse effectively torques the bulk (excess) magnetization into the $-z$ direction. The inversion recovery experiment tracks the bulk magnetization as it relaxes back to its equilibrium position along $+z$.

The spin-spin relaxation process has to do with the fact that the magnetization is actually measured in the transverse direction (xy -plane instead of along z). The magnetization cannot be measured along the z -axis because the large external magnetic field, \mathbf{B}_0 , is too overwhelming to measure the small magnetization caused by the spins. The NMR experiment proceeds as follows: a radiofrequency pulse torques the magnetization into the xy -plane for detection. After some time (described by the spin-spin relaxation time T_2), this transverse magnetization decays to zero because once the radiofrequency pulse is turned off, the transverse magnetization begins to precess about the \mathbf{B}_0 field at the Larmor frequency. However, it is impossible for the spins to maintain exact synchrony due to small fluctuations in the local field strength. This decay of the transverse magnetization to zero is described by the time constant, T_2 . The spin-echo experiment, which measures the decay of the NMR signal in the transverse plane, measures T_2 .⁴

1.4.3 Chemical Shift

Magnetic fields tend to vary on a sub-molecular distance scale due to the contribution of electron-generated currents. The external magnetic field induces circulating currents in the electron density distribution within molecules which, in turn, creates an additional induced and opposing (diamagnetic) magnetic field. The local magnetic field at a certain nucleus is given in Equation 1.5.³ The induced field (shielding) is about 10^{-4} the size of \mathbf{B}_0 .

$$\mathbf{B}_j^{loc} = \mathbf{B}_0 + \mathbf{B}_j^{induced} \quad (1.5)$$

The chemical shift (δ) is described by a tensor, specifically a 3 x 3 matrix of real numbers. Typically principal axes are assigned to each nuclei that correspond to structural features of the molecule. The principal values are defined when the axis of the induced field is along the external magnetic field (Equation 1.6). Equation 1.6 applies if the external field is along the z principal axis; analogous equations can be written for δ_{xx}^j and δ_{yy}^j where the external field is along the x and y principal axes, respectively. Each nuclear site has a different chemical shift tensor with a different principal axis system. All off-diagonal terms of the chemical shift tensor are zero for the principal axis system.

$$\mathbf{B}_j^{induced} = \delta_{zz}^j \mathbf{B}_0 \quad (1.6)$$

The isotropic chemical shift is the average of the 3 principal values $(\delta_{xx}^j, \delta_{yy}^j, \delta_{zz}^j)$ because the chemical shift is orientation-dependent and fast molecular motion samples all orientations. Chemical shift anisotropy (CSA) quantifies deviation from isotropy. This occurs when some orientations are preferred, as in anisotropic liquids and solids. Therefore, if molecular motion changes from isotropic to anisotropic, e.g., when a liquid crystal is cooled below its nematic-to-isotropic transition temperature, the NMR peak frequencies will change. The

chemical shift is no longer an average over all orientations with equal probability, but biased orientations are sampled relative to \mathbf{B}_0 because in the nematic phase the molecules are partially oriented. The theory of CSA is used when describing liquid crystals that have preferred orientations as in liquid crystals dimers described in Chapter 3 and liquid crystal thermosets described in Chapter 5.

CHAPTER 2: LIQUID STATE STRUCTURE VIA VERY HIGH-FIELD NMR

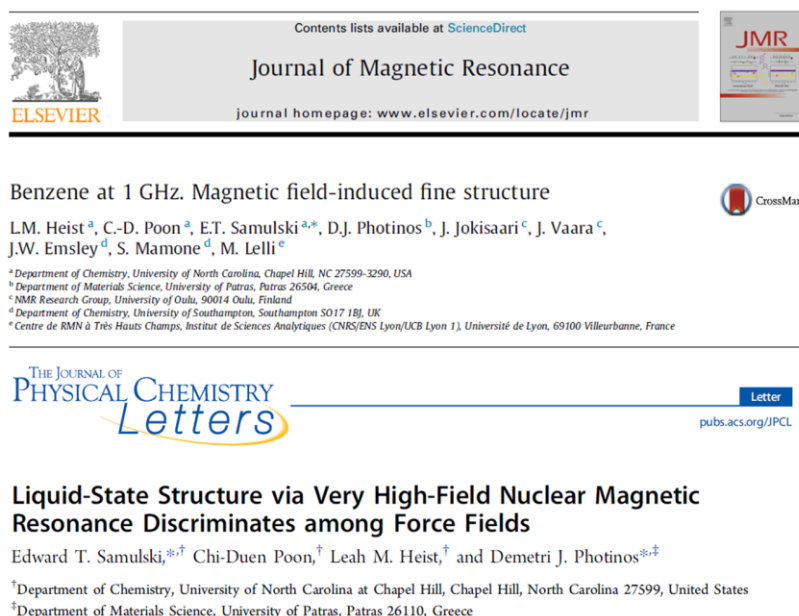


Figure 2.0. Some contents of this chapter and additional information appear in two publications in *Journal of Magnetic Resonance* and *Journal of Physical Chemistry Letters*.

2.1 Introduction

Efforts to describe the structure of the liquid phase followed far behind those applied to solids and gases.⁵ By the 1950s, however, the liquid state received more attention and attempts to develop a theory of liquids increased.^{6–9} Previous work in liquid state structure included explanations of various thermal and mechanical experimental observations via the use of crystal and gas structural ideas with an assumption that liquids were primarily composed of local crystalline-like short-range order. Sophisticated experimental measurements of liquid state structure have largely been restricted to X-ray and neutron diffraction. With increasing interest in modeling the liquid state, J.D. Bernal proposed his

theory for a geometric model of liquid state structure and hoped that it could be adapted for computer simulations, which was steadily growing at the time.¹⁰

Molecular dynamics (MD) simulations have provided the most progress in developing a complete molecular description of the liquid state.^{11,12} However, computer simulations are reliant on the accuracy of the force field used. MD simulates the movement of atoms; the force field replaces true forces and potential energies between atoms with a simplified model of pairwise “atomistic” interactions.¹³ Force fields describing those interactions have differing levels of complexity and the choice of force field is a balance between maximization of accuracy of simulations with minimization of computing time. As computing power has grown, force fields have improved^{14–16} and are continuously optimized. Optimization includes fitting simulated data to available experimental results (i.e. heat of vaporization, density, self-diffusion, X-ray, and neutron scattering) or performing quantum calculations.¹⁷ With this limited set of experimental parameters, it is often difficult to discriminate between force fields for a given system. Therefore, it is of use to find additional experimental parameters that simulated results can be fit to in order to improve the reliability of a chosen force field. Specifically, molecular simulations benefit from experimental parameters that probe subtle intermolecular interactions.

We show that very high-field ^2H nuclear magnetic resonance (NMR) yields an additional experimental parameter that discriminates against force fields. The technique uses deuterated liquids and their mixtures to extract the leading tensor component of the pair correlation function, a parameter that can readily be calculated from MD simulations. These experimental parameters are very sensitive to the choice of force field because they are a directional probe of molecular interactions. This is demonstrated here for a several

molecular liquids and mixtures showing that experimental parameters found using the high-field NMR method are very sensitive to the choice of simulation force field. This new experimental parameter is a directional probe of molecular interactions whereas many experimental parameters are dominated by isotropic interactions (i.e. density, self-diffusion, and heat of vaporization).

Herein we describe the application of high field NMR observations for the prototypical liquids benzene and chloroform, in binary and tertiary mixtures. Results are also presented for thiophene, which provides an example of less symmetric molecule and, consequently, a richer set of measurable quantities.

2.2 High Field ^2H NMR Magnetic Field Induced Alignment of Deuterated Liquids

It is well understood that anisotropic liquids (liquid crystals) can align when an external field is applied. Molecular orientation in ordinary liquids, however, is less studied. With the advent of high strength magnetic fields,¹⁸ very small molecular alignments due to the molecular magnetic anisotropy—the magnetizability—can be detected with NMR by measuring associated nonzero averages of dipolar and quadrupolar interactions.

This molecular alignment effect in isotropic liquids was first described by MacLean and co-workers in 1978.¹⁹ A strong external magnetic field will align magnetically anisotropic molecules relative to the field direction. Brownian motion of these molecules disturbs this alignment, however, so only a very small residual alignment results.²⁰ Dipolar interactions are, relative to quadrupolar interactions, small and make detection of the alignment in simple liquids difficult. Quadrupolar couplings are the dominant interactions in ^2H NMR. The ^2H nucleus has an asymmetric nuclear charge distribution (quadrupole moment) and interactions between the electric field gradient formed by bonding electrons

and the nuclear quadrupole moment perturb the Zeeman magnetic energy levels and are readily detected.³

Magnetic field-induced molecular alignment may be described by an “order parameter” given by the average, $S = \langle 3/2 \cos^2 \theta - 1/2 \rangle$, where θ is the angle between the applied magnetic field direction and the principal axis of the molecular magnetizability.¹⁹ The approximate alignment imposed by a magnetic field on aromatic molecules (with anisotropic magnetic magnetizability) is around $S = 10^{-5}$ to 10^{-6} . To put that in perspective, order parameters exhibited by liquid crystals in a magnetic field are between $S = 10^{-2}$ and 1. The alignment of aromatic molecules studied here are similar to that experienced by polar molecules in an electric field (10^{-4} to 10^{-6}).²¹ Although not as strong as that of liquid crystals, these alignments are still large enough to be detected using high-resolution, high-field NMR.

The alignment described is detected because of the non-zero average nuclear interactions present in an aligning medium—a liquid crystal or merely a very high magnetic field. The complete Hamiltonian (Equation 2.1) describes the nuclear interactions in a spin system and is the sum of the Zeeman interaction (Z), the interaction between the nuclear spin and the external magnetic field and the internal interactions from Equation 1.1.²²

$$\hat{H}_j = \hat{H}_j^Z + \hat{H}_j^{CS} + \hat{H}_j^Q + \hat{H}_{jk}^{DD} + \hat{H}_{jk}^J \quad (2.1)$$

The quadrupolar (\hat{H}_j^Q) and dipolar (\hat{H}_{jk}^{DD}) interactions are neglected in isotropic liquids due to isotropic averaging motions; however, they become apparent in NMR spectra of aligned molecules. The resonance line is split as a result of the alignment and its magnitude is dependent on the angle between the C—D bond axis and the principal molecular magnetizability direction.²³

From Equation 1.2, the resulting quadrupolar term of the spin Hamiltonian (Equation 2.2) is described in terms of $\overline{V_{z'z'}}$, the average electric field gradient formed by the electron distribution at the nucleus. The \hat{z}' unit vector is chosen so that it is parallel to the magnetic field axis (\mathbf{B}_0) in the laboratory axis system.¹⁹

$$\hat{H}_Q = \frac{3}{2} \frac{eQ}{6h} \overline{V_{z'z'}} (3\hat{I}_{z'}^2 - 2) \quad (2.2)$$

The resonance line splitting is given by Equation 2.3.¹⁹

$$\Delta\nu = \frac{3}{2} \left(\frac{eQ}{h} \right) \overline{V_{z'z'}} \quad (2.3)$$

The simplified expression for $\overline{V_{z'z'}}$ is expressed in terms of the molecular field gradients $V_{\alpha\beta}$ and the polar angles θ and φ , where θ is the angle between the \hat{z} and \hat{z}' axes (Equation 2.4).²¹ The principal axes ($\hat{x}, \hat{y}, \hat{z}$) are chosen so that V_{zz} is the largest component and V_{yy} is the smallest component. This makes the EFG asymmetry parameter, $\eta_{EFG} = (V_{xx} - V_{yy})/V_{zz}$, positive.

$$\overline{V_{z'z'}} = V_{zz} \left\langle \frac{3}{2} \cos^2 \theta - \frac{1}{2} \right\rangle + \frac{1}{2} (V_{xx} - V_{yy}) \langle \sin^2 \theta \cos 2\varphi \rangle \quad (2.4)$$

It is common to introduce a third axis system: the molecular axes $\hat{a}, \hat{b}, \hat{c}$ that all deuterated sites on the molecule have in common. The molecular axis is chosen so that one of its axes is identified with the molecular symmetry axis and the other two are taken perpendicular to the symmetry planes. The molecular and local frames do not always coincide, so sometimes it is necessary to transform axes by relating V_{zz} and $(V_{xx} - V_{yy})$ in Equation 2.4 to components in the local frame where l is the direction cosine of the molecular axis α , $(V_{xx} - V_{yy})/V_{zz}$ is the asymmetry parameter, η_{EFG} , and V_{zz} is eq (Equation 2.5).²¹

$$V_{\alpha\alpha} = eq \left\{ \left[\frac{3}{2} (l_{z\alpha})^2 - \frac{1}{2} \right] + \frac{1}{2} \eta \left[(l_{x\alpha})^2 - (l_{y\alpha})^2 \right] \right\} \quad (2.5)$$

In aromatic molecules (i.e. benzene), the principal molecular axis is the axis where the magnetizability is the largest (z-axis). In molecules similar to benzene this corresponds to the C₆ axis of symmetry. It follows that the resonance line splitting of benzene can be described by Equation 2.6.²¹

$$\Delta\nu = -\frac{3}{4} \left(\frac{e^2 q Q}{h} \right) (1 + \eta_{EFG}) \left\{ \left\langle \frac{3}{2} \cos^2 \theta - \frac{1}{2} \right\rangle + c \langle \sin^2 \theta \cos 2\varphi \rangle \right\} \quad (2.6)$$

In Equation 2.6, c is a constant that accounts for the transformation from the molecular axis to the local axis. The quadrupolar coupling constant is $e^2 q Q / h$ and the angular brackets $\langle \dots \rangle$ denote motional averages of the direction of the magnetic field relative to the principal EFG axes at the deuterated site. The two orientational averages in Equation 2.6 are referred to as the molecular orientation order parameters, S and R , and are given in Equation 2.7.

$$S = \left\langle \frac{3}{2} \cos^2 \theta - \frac{1}{2} \right\rangle, \quad R = \langle \sin^2 \theta \cos 2\varphi \rangle \quad (2.7)$$

where θ is the angle of the magnetic field direction \hat{z}' relative to the \hat{c} molecular axis and φ is the angle between the \hat{a} axis and the projection of the magnetic field direction \hat{z}' on the \hat{a}, \hat{b} plane. The average term can be calculated with Boltzmann statistics (Equations 2.8 and 2.9).²¹

$$\left\langle \frac{3}{2} \cos^2 \theta - \frac{1}{2} \right\rangle = \frac{1}{15} \frac{\Delta\chi B^2}{kT} \quad (2.8)$$

$$\langle \sin^2 \theta \cos 2\varphi \rangle = \frac{1}{15} \frac{\delta\chi B^2}{kT} \quad (2.9)$$

In Equation 2.8, $\Delta\chi$ is the anisotropy of the molecular magnetizability and in Equation 2.9, $\delta\chi$ describes the asymmetry of the molecular magnetizability (Equation 2.10).

$$\Delta\chi = \chi_{cc} - 1/2(\chi_{aa} + \chi_{bb}), \quad \delta\chi = \chi_{aa} - \chi_{bb} \quad (2.10)$$

The deuterated liquids and their mixtures studied here include benzene, chloroform, and thiophene. The molecular axes system for each is shown in Figure 2.1.

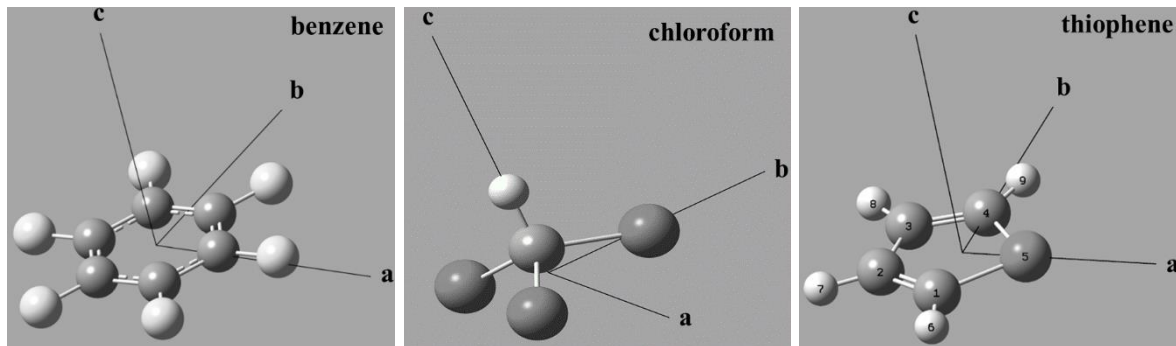


Figure 2.1. The molecular axes system for benzene, chloroform, and thiophene.

2.2.1 ^2H NMR of Benzene at 1 GHz

The quadrupolar splitting $\Delta\nu$ that results from the small alignment effect in benzene- d_6 is ~ 1 Hz at 22.3 T. We also observed the ^2H NMR spectrum of benzene- d_6 in a slightly higher field spectrometer (23.4 T, 1 GHz protons) (Figure 2.2). Three split resonances are observed: the splitting of the central resonance $\Delta\nu'$ and two ^{13}C satellite doublets $\Delta\nu$. The magnitude of $\Delta\nu'$ is smaller than $\Delta\nu$ and this difference, $\Delta(\Delta\nu - \Delta\nu')$ is due to the unresolved fine structure; the direct dipole-dipole interactions are negligible (~ 0.01 Hz). In our report in *Journal of Magnetic Resonance*²⁴ we determine the origins of and simulate this difference, and report pulse sequences that exploit the connectivity of the peaks in the ^{13}C and ^2H spectra to determine the relative signs of the indirect coupling, J_{CD} , and $\Delta\nu$. The result: a positive sign for $\Delta\nu$ is consistent with the expected orientation of benzene in the magnetic field. The

magnetic energy of the aromatic ring is lowest for configurations where the C_6 axis is normal to the field.

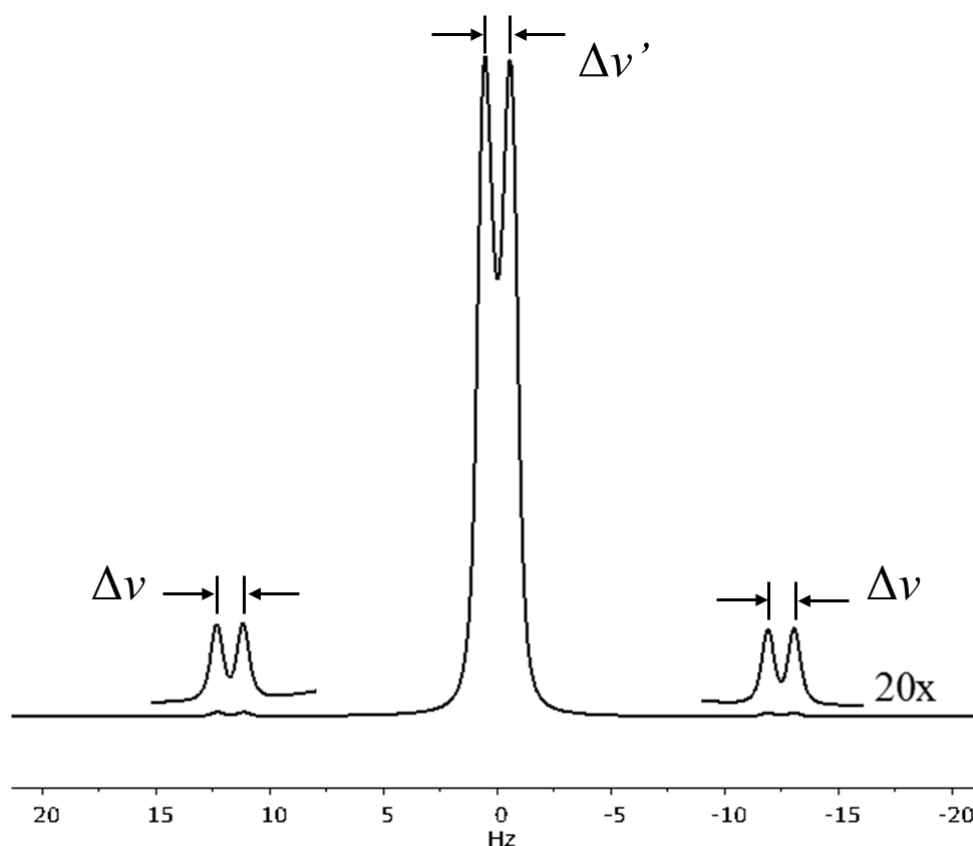


Figure 2.2. ^2H spectra at 153.553 MHz of neat C_6D_6 acquired with a standard single-pulse sequence by using the tuned ^2H lock channel and stopping the lock signal acquisition during the experiment. The low radiofrequency power allowed for the lock channel has limited the $\pi/2$ pulse to 174.0 μs (1.43 kHz), but this is sufficiently long to uniformly excite the narrow spectral width in all of the present experiments. Both spectra were obtained averaging 64 scans with 32k complex points for an acquisition time of 8.53 s and a recycle delay of 2.0 s.

The origin of this difference, $\Delta(\Delta\nu)$, was perplexing at first because the ^{13}C satellites should have the same splitting as the central line if we assume the quadrupolar interaction is dominant. At first we thought this could be an issue with the data analysis- the splittings of the center and satellite peaks were obtained by fitting the line shapes with the program MestreNova (version 9.0.1). The program defines an optimized Lorentzian-Gaussian function for each peak that varies the chemical shift, height, width, and area of the peak.

There is some variation in the splittings calculated from the direct measurement of the separation of the peak maxima, fitting the full spectrum, or fitting each doublet separately. The fitting routines were tested by generating a spectrum consisting of 6 lines centered approximately at the same positions as those in the experimental spectrum. The model spectrum had equal line separations and linewidths. The fitting routines obtained the correct line positions, and linewidths, and it was concluded that these routines were not introducing errors for the line positions. Hence, in agreement with the experimental spectra, the magnitude of double splitting of the central line is different from those of the ^{13}C satellite peaks.

Another proposal for the origin of this difference was that the C—D bond length differs for ^{13}C and ^{12}C , which impacts the quadrupolar coupling constant.^{25–27} However, even using dramatic estimates for bond lengths, this could not explain the difference in the quadrupolar splitting between the ^{13}C satellites and the central peak. Another consideration was the effect of a single ^{13}C on the molecular magnetizability tensor and its putative influence on the molecular order tensor. The question was whether or not the presence of ^{13}C breaks the 6-fold symmetry of benzene. However, this difference vanishes for the proton decoupled natural abundance ^2H NMR spectrum of neat benzene (Figure 2.3). For this spectrum the quadrupolar splitting measured from the ^{13}C satellites and from the central doublet are equal within an experimental error of ± 0.02 Hz, and the linewidths are equal within the larger error range of ± 0.1 Hz.

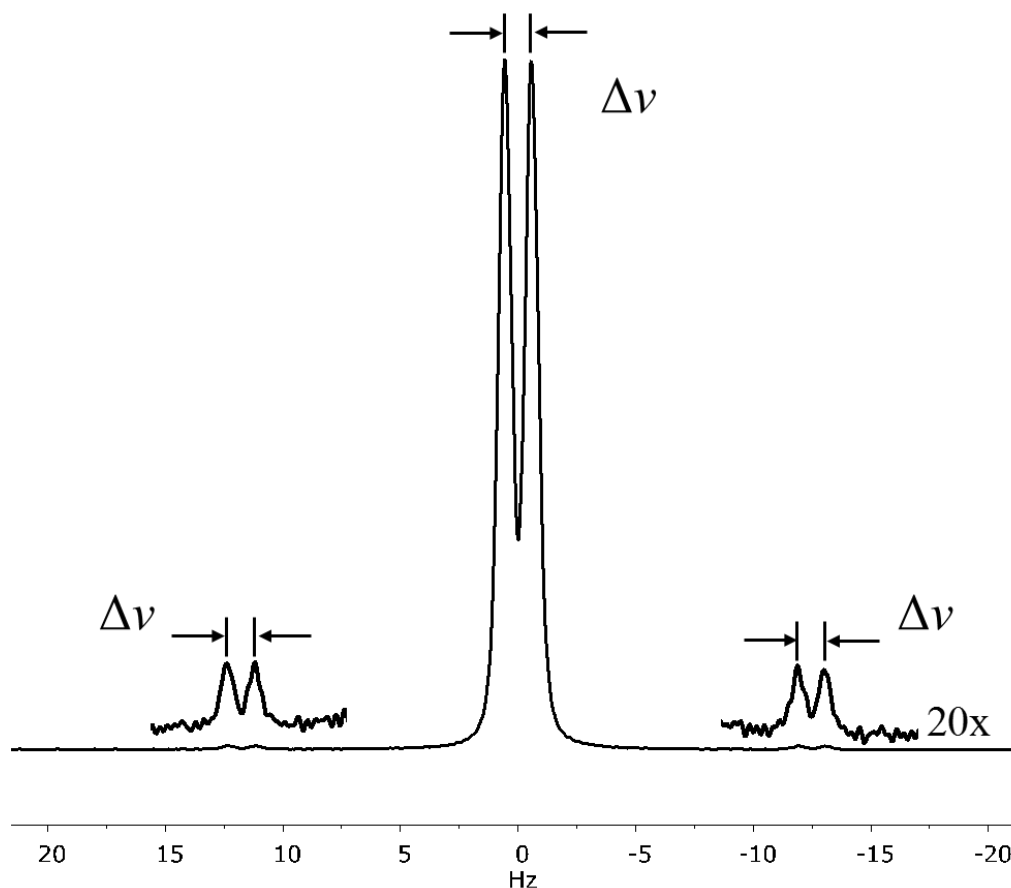


Figure 2.3. $^2\text{H} - \{^1\text{H}\}$ spectrum at 153.553 MHz of deuterium nuclei present at natural abundance in neat C_6H_6 obtained by addition of 23168 scans as described in the text. The spectrum was acquired using the ^2H lock channel by stopping the lock acquisition during the experiment. The ^2H $\pi/2$ pulse was 155.0 μs (1.61 kHz). The acquisition time was 3.2s, collecting 12288 complex points. During the acquisition time a ^1H WALTZ-65 decoupling at 2.77 kHz of power was applied. The recycle delay was set to 0.5 s. The magnitudes of the apparent doubles and $\Delta(\Delta\nu)$ are given in Table 2.1.

Table 2.1. Quadrupolar splitting and $\Delta(\Delta\nu)$ for Figures 2.1-3.

spectrum	left satellite doublet (Hz)	center doublet (Hz)	right satellite doublet (Hz)	$\Delta(\Delta\nu)$ (Hz)
Figure 2.2	1.16	1.06	1.15	0.10 ± 0.01
Figure 2.3	1.15	1.14	1.12	-0.02 ± 0.02

In sum, the difference in the splittings observed in Figure 2.2 derives from indirect and residual dipolar couplings in neat C_6D_6 where the envelope of the unresolved fine

structure for the central doublet leads to an apparent difference between the satellite splittings and that of the central doublet. This is consistent with the lower apparent resolution for the central doublet of C₆D₆ compared to the natural abundance ²H spectrum of C₆H₆.

Fortuitously, the envelope of the fine structure in the satellite doubles is an excellent approximation to the actual quadrupolar splitting.²⁴ For this reason, the ¹³C satellite doublets for benzene are used as the true quadrupolar splitting for relation to molecular pair correlations in the remaining sections.

2.3 Relation of Order Parameters to Molecular Pair Correlations in a Liquid in a High Magnetic Field

The orienting potential of a molecule in a magnetic field with diamagnetic anisotropy tensor $\tilde{\chi}$ is on the order of 10⁻⁴kT. Starting from the formal statistical mechanics definition of the order parameter of molecule of species A in a liquid consisting of N_J molecules ($N_J = N_A + N_B + N_C + \dots$) S_A , the first-order perturbation result is given in Equation 2.11.

$$S_A = \left(\frac{B^2}{10kT} \right) \left(\chi_A^{cc} \left(1 + x_A (\bar{g}_{AA}^{00} + \frac{1}{2} \eta_A^z \bar{g}_{AA}^{02}) \right) + x_B \chi_B^{cc} (\bar{g}_{AB}^{00} + \frac{1}{2} \eta_B^z \bar{g}_{AB}^{02}) + x_C \chi_C^{cc} (\bar{g}_{AC}^{00} + \frac{1}{2} \eta_C^z \bar{g}_{AC}^{02}) + \dots \right) \quad (2.11)$$

Here $x_J = N_J / N$ is the mole fraction of species $J (= A, B, C, \dots)$, $\eta_j^z = (\chi_j^{aa} - \chi_j^{bb}) / \chi_j^{cc}$ denotes the magnetic biaxiality of the molecule and $\chi_j^{aa}, \chi_j^{bb}, \chi_j^{cc}$ denote the principal values of $\tilde{\chi}$, with $\chi_j^{aa} + \chi_j^{bb} + \chi_j^{cc} = 0$ and the principal axes $\hat{a}, \hat{b}, \hat{c}$ assigned so that

$|\chi_j^{cc}| \geq |\chi_j^{aa}| \geq |\chi_j^{bb}|$. The magnetic biaxiality is zero for an axially symmetric molecule and

Equation 2.11 can be reduced to Equation 2.12 (even for a magnetically biaxial molecule, this term is very small and in most cases can be neglected).

$$S_A = \left(\frac{B^2}{10kT} \right) (\chi_A^{cc} (1 + x_A \bar{g}_{AA}^{00}) + x_B \chi_B^{cc} \bar{g}_{AB}^{00} + x_C \chi_C^{cc} \bar{g}_{AC}^{00} + \dots) \quad (2.12)$$

The correlation factors expressed as \bar{g}_{AJ}^{00} are integrals of the pair correlation function

$g_{AJ}(\vec{r}; \omega_1, \omega_i)$, specifically

$$\bar{g}_{AJ}^{00} = \frac{N}{V 8\pi^2} \int d\omega_1 \int d\omega_i d\vec{r} \left(\frac{3}{2} \cos^2 \theta_1 - \frac{1}{2} \right) \times \left(\frac{3}{2} \cos^2 \theta_i - \frac{1}{2} \right) \times g_{AJ}(\vec{r}; \omega_1, \omega_i) \quad (2.13)$$

Equivalently, these correlation factors can be directly identified with the radical integrals of the second rank function of the tensor expansion²⁸ of the pair correlation function for axially symmetric molecules

$$g(\omega_1 \omega_2 \mathbf{r}) = \sum_{l_1 l_2 l} \sum_{m_1 m_2 m} g(l_1 l_2 l; r) C(l_1 l_2 l; m_1 m_2 m) Y_{l_1 m_1}(\omega_1) Y_{l_2 m_2}(\omega_2) Y_{lm}^*(\omega) \quad (2.14)$$

where $C(l_1 l_2 l; m_1 m_2 m)$ denotes the Clebsch-Gordan coefficients and Y_{lm} is the spherical harmonics. In particular,

$$\bar{g}_{AJ}^{00} = \left(\frac{N}{V} \right) \sqrt{5\pi} \int r^2 g_{AJ}(220; 00; r) d\mathbf{r} \quad (2.15)$$

Similarly, starting from the counterpart of the formal statistical mechanics definition of S_A for the order parameter R_A for a molecule of species A we obtain the result

$$R_A = \left(\frac{B^2}{10kT} \right) \left(\chi_A^{cc} \left(\frac{2}{3} \eta_A^\chi + x_A \left(\bar{g}_{AA}^{20} + \frac{1}{2} \eta_A^\chi \bar{g}_{AA}^{22} \right) \right) + x_B \chi_B^{cc} \left(\bar{g}_{AB}^{20} + \frac{1}{2} \eta_B^\chi \bar{g}_{AB}^{22} \right) + x_C \chi_C^{cc} \left(\bar{g}_{AC}^{20} + \frac{1}{2} \eta_C^\chi \bar{g}_{AC}^{22} \right) + \dots \right) \quad (2.16)$$

where the correlation factors \bar{g}_{AJ}^{20} are obtained from the Wigner expansion second rank components analogously to Equation 2.15.

The order parameter S_A has a concentration independent part, which does not involve molecular pair correlations $[S_A]_0 = B^2 \chi_A^{cc} / 10kT$, describing the ordering of an isolated

molecule at infinite dilution. For benzene this value matches what is found in Equation 2.8.

The ratio $S_A/[S_A]_0$ is often²⁹⁻³² expressed as a ratio $g_2 = [\chi_A^{cc}]_{eff} / \chi_A^{cc}$ where $[\chi_A^{cc}]_{eff}$ is an effective magnetizability anisotropy and g_2 is the Kirkwood correlation factor, given explicitly in Equation 2.17 using the expression for S_A found in Equation 2.11.

$$g_2 = \frac{S_A}{[S_A]_0} = \left(1 + \sum_{J=A,B,\dots} x_J \frac{\chi_J^{cc}}{\chi_A^{cc}} \left(\bar{g}_{AJ}^{00} + \frac{1}{2} \eta_J^z \bar{g}_{AJ}^{02} \right) \right) \quad (2.17)$$

Similarly, for magnetically biaxial molecules, the concentration independent (infinite dilution) part of the order parameter is $[R_A]_0 = (B^2 \chi_A^{cc} / 10kT)(2/3\eta_A^z)$ (matching Equation 2.9 for benzene) and the ratio $[\eta_A^z]_{eff} / \eta_A^z$ where $[\eta_A^z]_{eff}$ is an effective biaxiality (Equation 2.18).

$$\frac{R_A}{[R_A]_0} = \frac{[\eta_A^z]_{eff}}{\eta_A^z} = \left(1 + \sum_{J=A,B,\dots} x_J \left(\frac{3\chi_J^{cc}}{2\eta_A^z \chi_A^{cc}} \right) \left(\bar{g}_{AJ}^{20} + \frac{1}{2} \eta_J^z \bar{g}_{AJ}^{22} \right) \right) \quad (2.18)$$

The liquid systems studied here fall under the following symmetry categories with their respective values of S_A and R_A .

1. Binary mixtures where the molecules of species A are magnetically uniaxial meaning the \hat{c} axis is a symmetry axis with greater than twofold symmetry and molecules of species B are magnetically isotropic ($\chi_B^{cc} = 0$). This is the case for A = benzene-d₆ and B = tetramethylsilane (TMS) and for A = chloroform-d and B = TMS.

Expressions for the order parameters in Equations 2.11 and 2.16 reduce to Equation 2.18.1.

$$S_A = \left(\frac{B^2 \chi_A^{cc}}{10kT} \right) (1 + x_A \bar{g}_{AA}^{00}) ; R_A = 0 \quad (2.18.1)$$

2. Tertiary mixtures is which the molecules of species A and B are uniaxial and of equal concentrations, $x_A = x_B = x \leq 1/2$ and molecules of species C are magnetically

isotropic. This is the case for $A = \text{benzene-d}_6$, $B = \text{hexafluorobenzene (C}_6\text{F}_6\text{)}$, and $C = \text{TMS}$. Expressions for the order parameters in Equations 2.11 and 2.16 reduce to Equation 2.18.2.

$$S_A = \left(\frac{B^2 \chi_A^{cc}}{10kT} \right) \left(1 + x \left(\bar{g}_{AA}^{00} + \left(\frac{\chi_B^{cc}}{\chi_A^{cc}} \right) \bar{g}_{AB}^{00} \right) \right); \quad R_A = 0 \quad (2.18.2)$$

3. Binary mixtures where the molecules of species A are magnetically biaxial meaning the \hat{c} axis is not a symmetry axis and molecules of species B are magnetically isotropic. This is the case for $A = \text{thiophene-d}_4$ and $B = \text{tetramethylsilane (TMS)}$. Expressions for the order parameters in Equations 2.11 and 2.16 reduce to Equation 2.18.3.

$$S_A = \left(\frac{B^2 \chi_A^{cc}}{10kT} \right) \left(1 + x_A \left(\bar{g}_{AA}^{00} + \frac{1}{2} \eta_A^z \bar{g}_{AA}^{02} \right) \right); \quad R_A = \left(\frac{B^2 \chi_A^{cc}}{10kT} \right) \left(\frac{2}{3} \eta_A^z + x_A \left(\bar{g}_{AA}^{20} + \frac{1}{2} \eta_A^z \bar{g}_{AA}^{22} \right) \right) \quad (2.18.3)$$

In addition to the explicit dependence of S_A and R_A on concentration, there is an implicit concentration dependence of correlation factors. The concentration dependence on correlation factors is generally weak for the systems studied here because the measurements are taken far away from any phase transitions and can be estimated by the leading terms in the Taylor expansion. The variation with concentration x is obtained from the pure compound ($x = 1$) values (Equation 2.19).

$$\bar{g}_{AJ}^{n_1 n_2}(x) \approx \bar{g}_{AJ}^{n_1 n_2}(x=1) + (1-x) \left[\frac{\partial \bar{g}_{AJ}^{n_1 n_2}}{\partial x} \right]_{x=1} + \frac{1}{2} (1-x)^2 \left[\frac{\partial^2 \bar{g}_{AJ}^{n_1 n_2}}{\partial T^2} \right]_{x=1} \quad (2.19)$$

As is evident in the next section, the quadratic terms of the Taylor series in Equation 2.19 are mostly below the resolution of the experimental measurements.

2.4 Evaluation of Correlation Factors from Measured Spectra

In the following we present the results from the study of four mixtures: (i) benzene in TMS, (ii) chloroform in TMS, (iii) benzene/hexafluorobenzene 1:1 mixture in TMS, and (iv) thiophene in TMS. Each mixture matches one of the cases laid out in Section 2.3 (Equations 2.18.1, 2.18.2, and 2.18.3). Table 2.2 gives all of the constants used to evaluate the data and calculate the order parameters in Equations 2.18.1-3. Benzene-d₆ has magnetically equivalent deuterons, chloroform-d has only one deuteron, and thiophene has two types of inequivalent deuterons. The deuterons 7,8 and 6,9 are labeled in Figure 2.1.

Table 2.2. Constants used in the determination of correlation factors for benzene, chloroform, and thiophene. Thiophene has inequivalent deuterons (see labeling in Figure 2.1) where deuterons 6 and 9 have their C—D bond adjacent to the sulfur atom.

molecule	constant	value
	B	22.3 T
	k	$1.38 \times 10^{-23} \text{ JT}^{-1}$
	T	303 K
benzene-d ₆	χ^{cc}	$-7.1 \times 10^{-28} \text{ JT}^{-2}$
	χ^{aa}	$+3.6 \times 10^{-28} \text{ JT}^{-2}$
	χ^{bb}	$+3.6 \times 10^{-28} \text{ JT}^{-2}$
	η_{EFG}	0.054 ³³
	ν_Q	$187 \pm 0.4 \text{ kHz}$ ³⁴
chloroform-d	χ^{cc}	$+1.5 \times 10^{-28} \text{ JT}^{-2}$
	χ^{aa}	$-0.76 \times 10^{-28} \text{ JT}^{-2}$
	χ^{bb}	$-0.76 \times 10^{-28} \text{ JT}^{-2}$
	η_{EFG}	0
	ν_Q	$167 \pm 0.6 \text{ kHz}$ ³⁵
thiophene-d ₄	χ^{cc}	$-5.7 \times 10^{-28} \text{ JT}^{-2}$
	χ^{aa}	$+2.8 \times 10^{-28} \text{ JT}^{-2}$
	χ^{bb}	$+2.9 \times 10^{-28} \text{ JT}^{-2}$
	η^z	0.016
	$\nu_Q(7,8)$	190.4 kHz
	$\eta_{EFG}(7,8)$	0.058
	$\nu_Q(6,9)$	193.6 kHz
	$\eta_{EFG}(6,9)$	0.080
	$\varphi(7,8)$	$(180 \pm 34)^\circ$
	$\varphi(6,9)$	$\pm 74^\circ$

2.4.1 Binary mixtures (Case 1)

In the cases of benzene and chloroform mixtures with TMS (a tetrahedral, magnetically isotropic molecule), the magnetically relevant \bar{g}_{AA}^{00} pair correlations are simply attenuated by the TMS diluent and for both mixtures the expression for the quadrupolar

splittings of the deuterated species at temperature T and mole fraction x_A is given in Equation 2.20.

$$\Delta \nu_A(T, x_A) = \nu_{0,A}(T) \left(1 + x \bar{g}_{AA}^{00} \right) \quad (2.20)$$

where $\nu_{0,A}(T)$ is the splitting of the isolated molecule (infinite dilution). According to Equations 2.3-5, the values of $\nu_{0,A}(T)$ for benzene and chloroform are given in Equations 2.20.1 and 2.20.2.

$$\nu_{0,benz}(T) = \left(\frac{-3}{4} \right) \nu_Q \left(\frac{B^2 \chi_{benz}^{cc}}{10kT} \right) (1 + \eta_{EFG}) \quad (2.20.1)$$

$$\nu_{0,clfm}(T) = \left(\frac{3}{2} \right) \nu_Q \left(\frac{B^2 \chi_{benz}^{cc}}{10kT} \right) \quad (2.20.2)$$

As stated previously, there is an implicit concentration dependence of \bar{g}_{AA}^{00} because pair correlations depend on whether species A (here benzene or chloroform) is predominantly surrounded by molecules of species A or the magnetically isotropic diluent TMS. This concentration dependence is described in Equation 2.19 and simplified here:

$$\bar{g}_{AA}^{00}(x) \approx \bar{g}_{AA}^{00}(x=1) + (1-x) \bar{g}_{AA}^{00'} + \frac{1}{2} (1-x)^2 \bar{g}_{AA}^{00''} . \quad (2.21)$$

The concentration dependence of the splittings of benzene and chloroform normalized to the infinite dilution splitting, $\Delta \nu / \nu_0$, is shown in Figure 2.4. It is clear that the concentration dependence is real, but moderate and using the Taylor series in Equation 2.21 is valid.

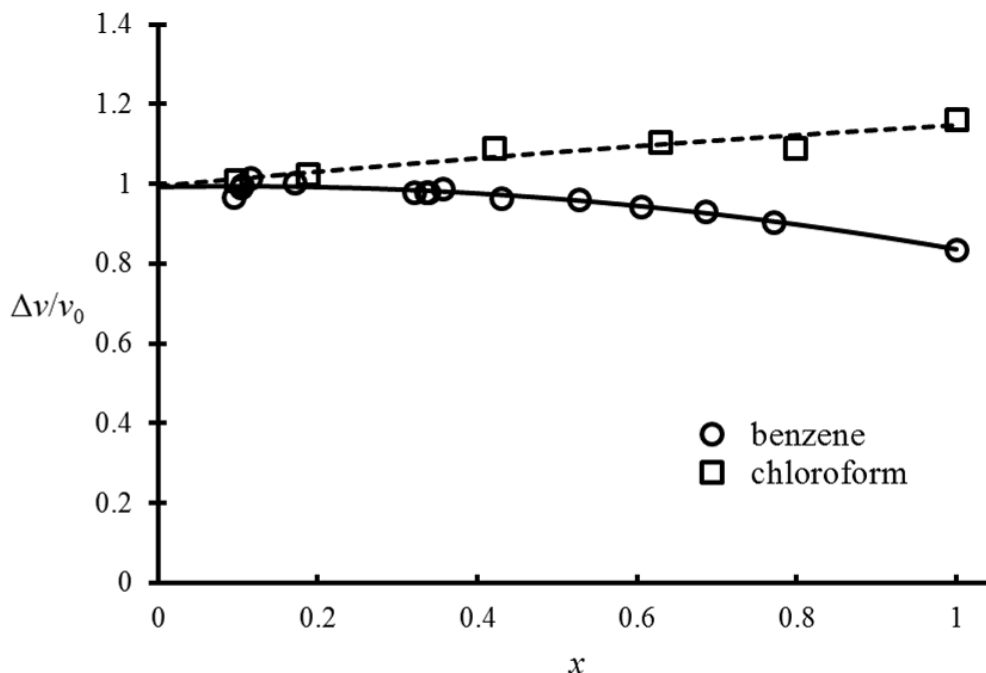


Figure 2.4. Observed $\Delta\nu/\nu_0$ versus x , the mole fraction of benzene- d_6 and chloroform- d in the diluent TMS; the respective lines are fits of Equation 2.21 to the data.

Details in this section on the benzene and chloroform analysis are given in our manuscript in the *Journal of Physical Chemistry Letters*.³⁶

2.4.1.1 Benzene in TMS

According to Equation 20.1 and using the constants for benzene listed in Table 2.2, $\nu_{0,benz}(T=T_0)_{calc} = 1.25 \text{ Hz}$. This calculated value is in agreement with experiment ($\Delta\nu/\nu_0$ extrapolates to 1 in Figure 2.4). The ^2H spectrum of neat benzene- d_6 is shown in Figure 2.5.

Using Equation 20 for neat benzene ($x = 1$) and the quadrupolar splitting

$(\Delta\nu_{benz}(T=T_0, x=1) = 1.04_5 \pm 0.00_5 \text{ Hz})$, $\bar{g}_{benz-benz}^{00}(x=1) = -0.16 \pm 0.01$. It is noted that the splitting measured here for neat benzene, when scaled to the magnetic field strength

$|\mathbf{B}| = 14.1 \text{ T}$ and temperature $T = 296 \text{ K}$ of previous measurements by Maclean and

coworkers is reduced to 0.43 Hz, which is very close to the value in ref 30 of 0.41 Hz. The

concentration dependence of the benzene splitting (Figure 2.4, circles) shows a slight deviation from linearity. The data can be fit adequately to Equation 2.21 (Figure 2.4, solid line) with $\bar{g}_{\text{benz-benz}}^{00'} = -0.21 \pm 0.07$; $\bar{g}_{\text{benz-benz}}^{00''}$ is less than the experimental resolution of the data points.

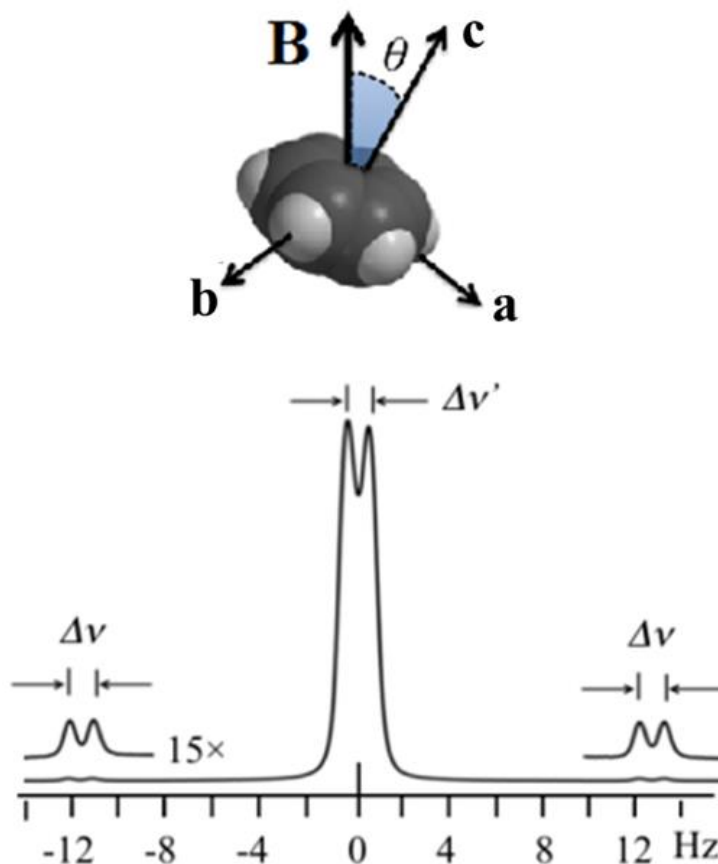


Figure 2.5. ^2H NMR spectrum of neat benzene- d_6 recorded at 22.3 T (Bruker Avance III 950 MHz proton NMR spectrometer at temperature, $T = 303$ K). The molecule-fixed frame specifies the angle θ that the magnetic field \mathbf{B} makes with the symmetry axis, \hat{c} , of the molecule. The outer ^{13}C satellite resonances show the true quadrupolar splittings $\Delta\nu$.²⁴

2.4.1.2 Chloroform in TMS

According to Equation 2.20.2 and using the constants for chloroform listed in Table

2.2, $\nu_{0,\text{clfm}}(T = T_0)_{\text{calc}} = 0.456\text{Hz}$. This calculated value is in agreement with experiment

($\Delta\nu/\nu_0$ extrapolates to 1 in Figure 2.4). The ^2H spectrum of neat chloroform-d is shown in Figure 2.6. Using Equation 2.20 for neat chloroform ($x = 1$) and the quadrupolar splitting ($\Delta\nu_{clfm}(T = T_0, x = 1) = 0.524 \pm 0.010 \text{ Hz}$), $\bar{g}_{clfm-clfm}^{00}(x = 1) = +0.15 \pm 0.02$. It is noted that the splitting measured here for neat chloroform, when scaled to the magnetic field strength $|\mathbf{B}| = 14.1 \text{ T}$ and temperature $T = 296 \text{ K}$ of previous measurements by Maclean and coworkers is reduced to 0.222 Hz, which is very close to the value in ref 29 of 0.223 Hz. The concentration dependence of the chloroform splitting (Figure 2.4, squares) shows no appreciable deviation from linearity; the data is fit to Equation 21 (Figure 2.4, dashed line) with $\bar{g}_{clfm-clfm}^{00\prime} = -0.03 \pm 0.06$ and $\bar{g}_{clfm-clfm}^{00''} \approx 0$.

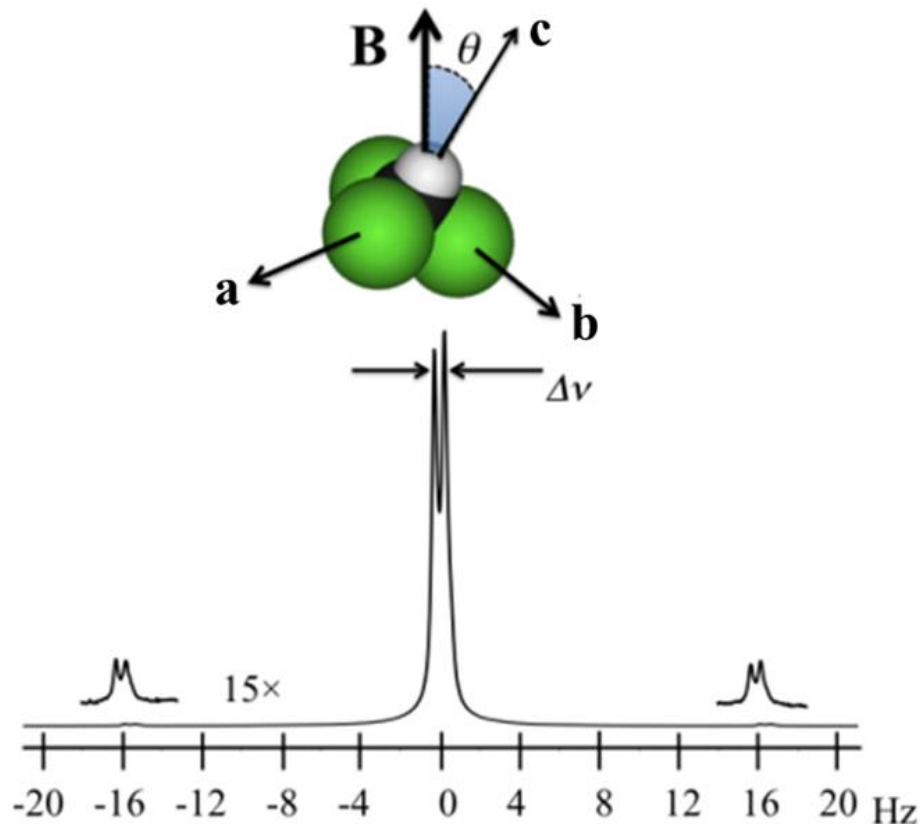


Figure 2.6. ^2H NMR spectrum of neat chloroform-d recorded at 22.3 T (Bruker Avance III 950 MHz proton NMR spectrometer at temperature, $T = 303$ K).

The molecule-fixed frame specifies the angle θ that the magnetic field \mathbf{B} makes with the symmetry axis, \hat{c} , of the molecule. The central resonance in addition to the outer ^{13}C satellite resonances show the true quadrupolar splittings $\Delta\nu$.

2.4.2 Tertiary mixtures (Case 2)

The tertiary mixtures studied are 1:1 mixtures diluted with the magnetically isotropic molecule TMS. The expression for the quadrupolar splittings of the deuterated species in a tertiary mixture at temperature T and mole fraction x (where $x = x_A = x_B$), where molecules A and B are uniaxial and molecule C is magnetically isotropic, is given in Equation 2.22.

$$\Delta\nu_A(T, x_A) = \nu_{0,A}(T) \left(1 + x \left(\bar{g}_{AA}^{00} + \left(\frac{\chi_B^{cc}}{\chi_A^{cc}} \right) \bar{g}_{AB}^{00} \right) \right) \quad (2.22)$$

where $\nu_{0,A}(T)$ is the splitting of the isolated molecule (infinite dilution). Since the molecule studied is benzene, the value of $\nu_{0,A}(T)$ is given in Equation 2.20.1 and the concentration dependence of \bar{g}_{AA}^{00} is given in Equation 2.21.

2.4.2.1 Benzene:hexafluorobenzene 1:1 mixture in TMS

The molecule of species A in this case is benzene-d₆, so that infinite dilution splitting in the mixture case should represent a single benzene molecule; $\nu_{0,benz}(T = T_0)_{calc} = 1.25 \text{ Hz}$. The concentration dependence of the splittings of benzene in the benzene/hexafluorobenzene mixture normalized to the infinite dilution splitting, $\Delta\nu/\nu_0$, is shown in Figure 2.7. As a comparison, the concentration dependence of the splittings of benzene-d₆ is also shown. This calculated value is in agreement with experiment ($\Delta\nu/\nu_0$ extrapolates to 1 in Figure 2.7 for benzene and the benzene/hexafluorobenzene mixture). The ²H spectrum of the neat 1:1 mixture of benzene-d₆/hexafluorobenzene is shown in Figure 2.8.

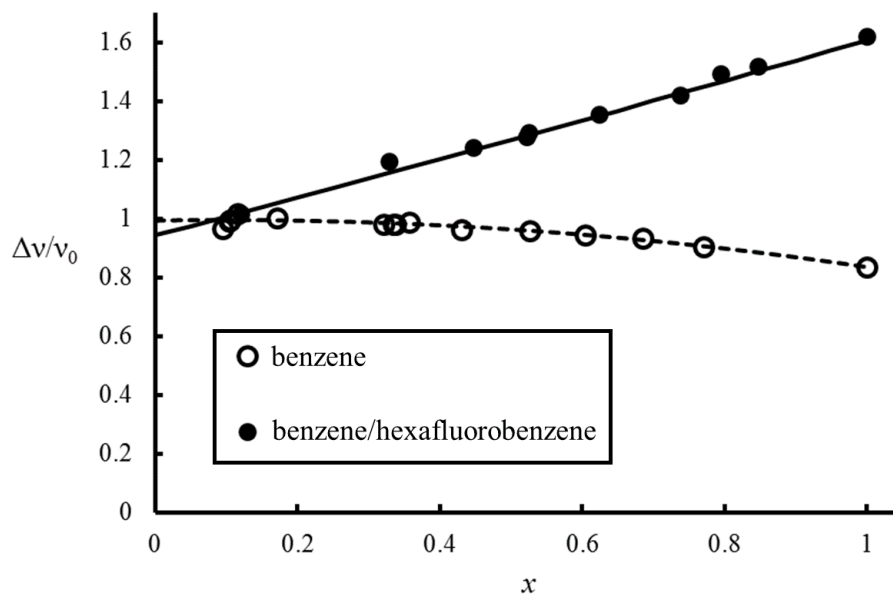


Figure 2.7. Observed $\Delta\nu/\nu_0$ versus x , the mole fraction of benzene-d₆ and hexafluorobenzene diluent TMS; the respective lines are fits of Equation 2.21 to the data.

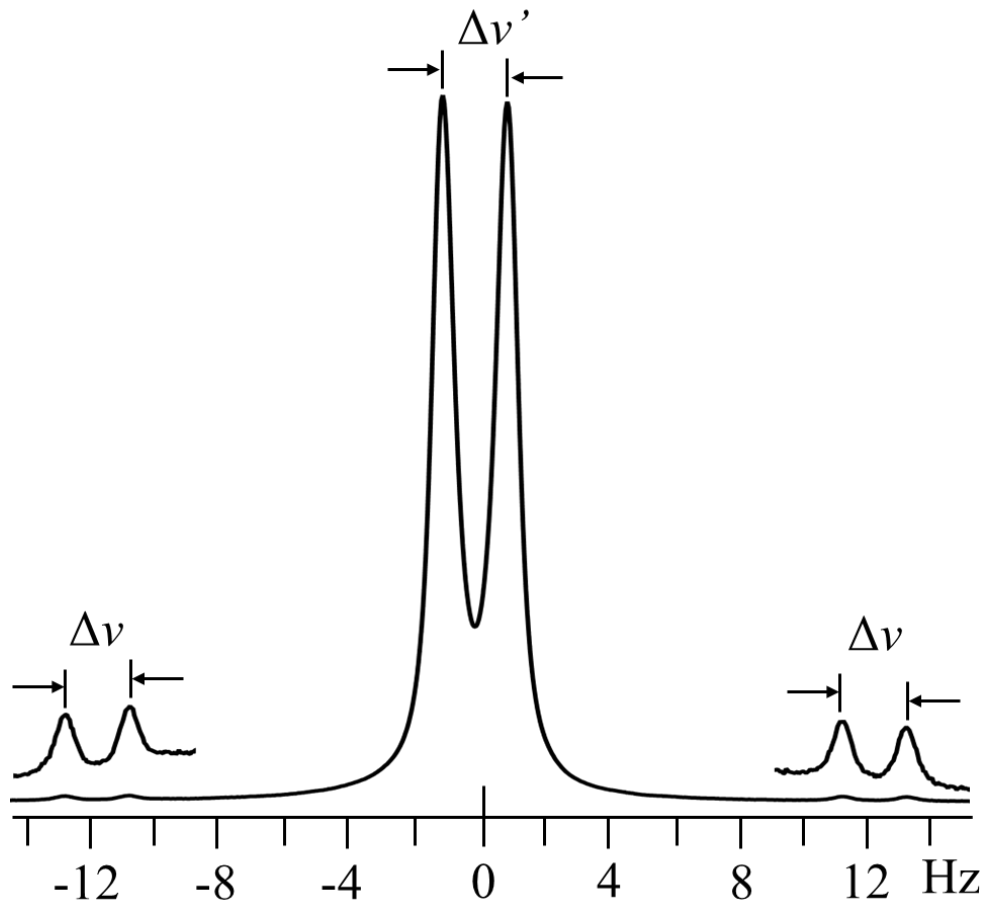


Figure 2.8. ^2H NMR spectrum of neat 1:1 mixture of benzene- d_6 /hexafluorobenzene (no TMS) recorded at 22.3 T (Bruker Avance III 950 MHz proton NMR spectrometer at temperature, $T = 303$ K). The outer ^{13}C satellite resonances show the true quadrupolar splittings $\Delta\nu$.

Using Equation 2.22 and the values in Table 2.2 for neat benzene- d_6 in the mixture (where $x = 1/2$) and the quadrupolar splitting ($\Delta\nu_{\text{benz}}(T = T_0, x = 1/2) = 2.01 \text{ Hz}$), the value for benzene in the mixture is

$$\bar{g}_{\text{benz}-\text{C}_6\text{F}_6}^{00} = \left[2 \left(\frac{\Delta\nu_A(T, x_A)}{\nu_{0,A}(T)} - 1 \right) - \bar{g}_{\text{benz}-\text{benz}}^{00} \right] \left(\frac{\chi_{\text{benz}}^{cc}}{\chi_{\text{C}_6\text{F}_6}^{cc}} \right) = +2.1 \quad (2.23)$$

where $\bar{g}_{\text{benz}-\text{benz}}^{00} = -0.16$ and $\chi_{\text{C}_6\text{F}_6}^{cc} = -4.6 \times 10^{-28} \text{ JT}^{-2}$. Interestingly, for this mixture the concentration dependence of the splitting (Figure 2.7) shows no appreciable deviation from

linearity; the data can be fit to a straight line (Figure 2.7, solid line) with $R^2 = 0.99$. This indicates that the *sum* of the pair correlation factors $\bar{g}_{benz-benz}^{00}$ and $\bar{g}_{benz-C_6F_6}^{00}$ shows no concentration dependence. The reason for this observation will be explained in more detail in Section 2.5.3 when the benzene/hexafluorobenzene complex is discussed.

2.4.2.2 Chloroform:benzene 1:1 mixture

The molecule of species *A* in this case is chloroform-d (the mixture is made up of protonated C_6H_6), so that infinite dilution splitting in the mixture case should represent a single chloroform molecule; $\nu_{0,clfm}(T = T_0)_{calc} = 0.456 \text{ Hz}$. The ^2H spectrum of the neat 1:1 mixture of chloroform/benzene is shown in Figure 2.9.

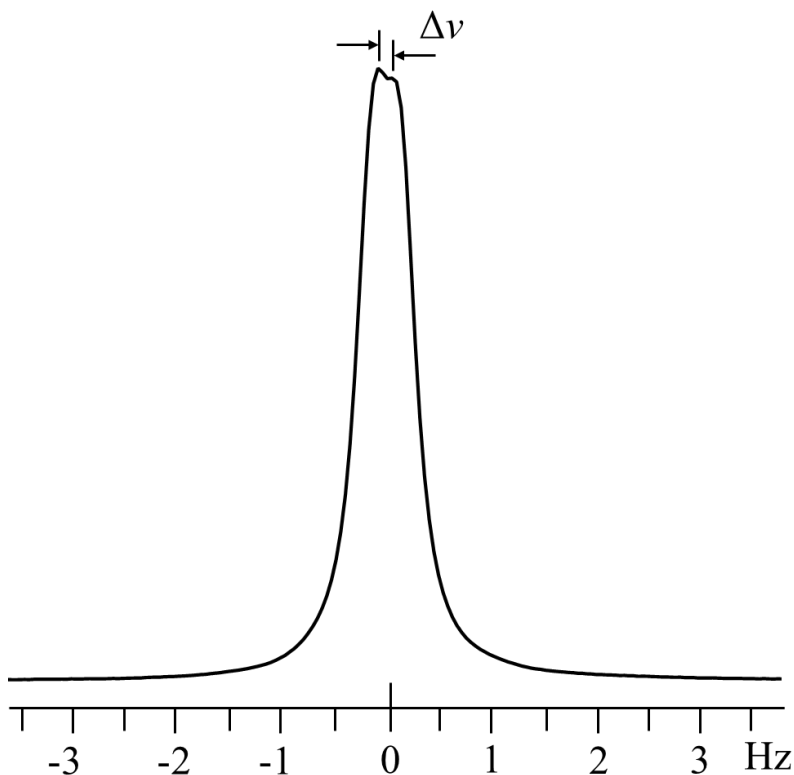


Figure 2.9. ^2H NMR spectrum of neat 1:1 mixture of chloroform-d/benzene (no TMS) recorded at 22.3 T (Bruker Avance III 950 MHz proton NMR spectrometer at temperature, $T = 303 \text{ K}$). The single central resonance shows the true quadrupolar splittings $\Delta\nu$ (^{13}C satellites not shown here).

Using Equation 2.22 with the appropriate values for the chloroform/benzene mixture and the values in Table 2.2 for neat chloroform-d in the mixture (where $x = 1/2$) and the quadrupolar splitting ($\Delta\nu_{clfm}(T = T_0, x = 1/2) \approx 0.26 \text{ Hz}$), the value for benzene in the mixture is

$$\bar{g}_{clfm-C_6H_6}^{00} = \left[2 \left(\frac{\Delta\nu_A(T, x_A)}{\nu_{0,A}(T)} - 1 \right) - \bar{g}_{clfm-clfm}^{00} \right] \left(\frac{\chi_{clfm}^{cc}}{\chi_{C_6H_6}^{cc}} \right) = +0.21 \quad (2.24)$$

From Figure 2.9 it is clear that the splitting is just on the edge of the resolution of the experiment- so this is likely far from a qualitative result, however, it is clear that there is a qualitative difference in the spectrum of chloroform-d when mixed with benzene as opposed to TMS.

2.4.3 Binary mixtures (Case 3)

2.4.3.1 Thiophene in TMS

In the case of thiophene (a magnetically biaxial molecule), it is possible to obtain two separate pair correlation factors, $\bar{g}_{thio-thio}^{00}$ and $\bar{g}_{thio-thio}^{20}$. There are two groups of non-equivalent deuterated sites, these are symmetrically located relative to the twofold symmetry axis of the molecule, identified with the molecular axis a. The c axis is normal to the ring (see geometry in Figure 2.1). From the geometrical data of the molecule (Table 2.2) we obtain the following expressions for the two groups of splittings (s) where $s = 6, 9$ or $7, 8$ (Equation 2.25).

$$\Delta\nu^{(s)} = \frac{3}{2} \nu_Q^{(s)} \left[-\frac{1}{2} S_A \times (1 + \eta_{EFG}^{(s)}) + \frac{1}{4} R_A \cos 2\phi^{(s)} (3 - \eta_{EFG}^{(s)}) \right] \quad (2.25)$$

S_A and R_A can be found in Equation 2.18.3. It will be assumed that $\bar{g}_{thio-thio}^{02}$ and $\bar{g}_{thio-thio}^{22}$ can be neglected because they are below the resolution of the experiment and are multiplied by already small values. The simplified equations for the order parameters from Equation 2.18.3 are

$$S_A = \left(\frac{B^2 \chi_A^{cc}}{10kT} \right) (1 + x_A \bar{g}_{AA}^{00}); R_A = \left(\frac{B^2 \chi_A^{cc}}{10kT} \right) \left(\frac{2}{3} \eta_A^\chi + x_A \bar{g}_{AA}^{20} \right) \quad (2.26)$$

Combining Equations 2.25 and 2.26, the values of $\bar{g}_{thio-thio}^{00}$ and $\bar{g}_{thio-thio}^{20}$ can be determined using the splittings for the two deuterons in thiophene. A spectrum of thiophene-d₄ in TMS is shown in Figure 2.10 with the peaks labeled according to the deuteron position (6,9 or 7,8). The pair correlation factors for thiophene are plotted in Figure 2.11. There is a slight concentration dependence for values at low concentration, but level out at high concentrations to $\bar{g}_{thio-thio}^{00} \approx -0.21$ and $\bar{g}_{thio-thio}^{20} \approx -0.034$.

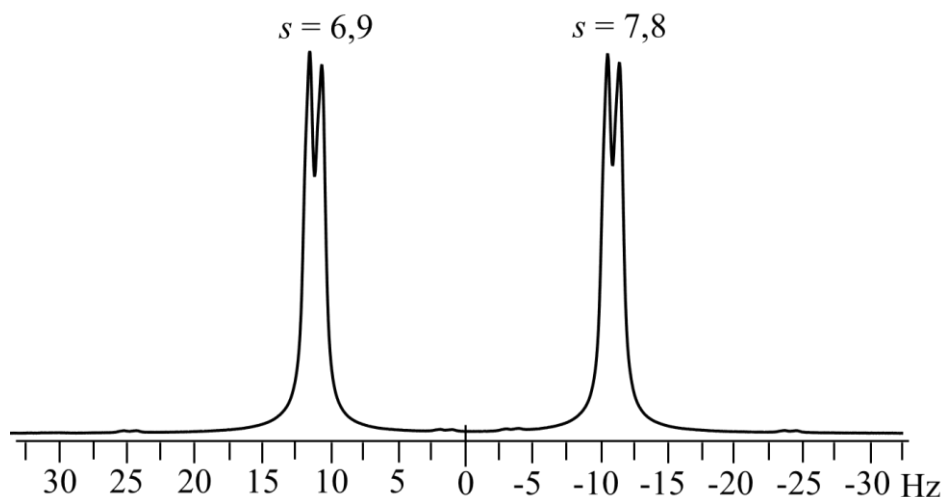


Figure 2.10. ^2H NMR spectrum of thiophene-d₄ (deuterons 6,9 and 7,8 labeled) recorded at 22.3 T (Bruker Avance III 950 MHz proton NMR spectrometer at temperature, $T = 303$ K).

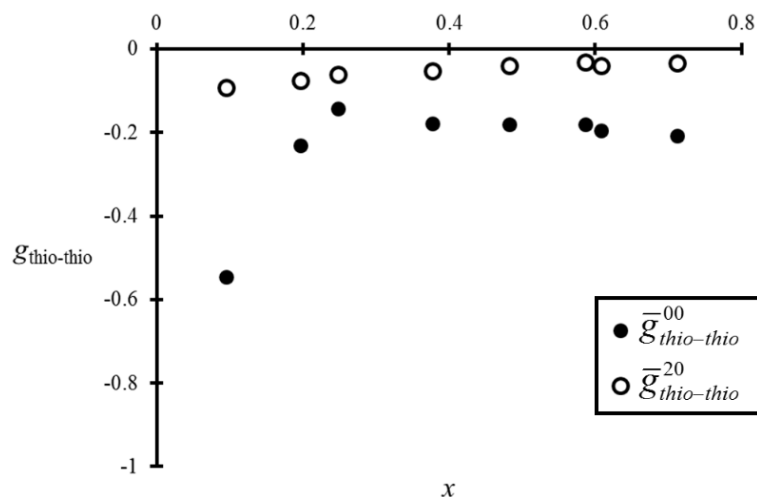


Figure 2.11. Concentration dependence of thiophene pair correlation factors versus x , the mole fraction of thiophene- d_4 in TMS.

2.5 Calculated correlation factors from molecular dynamics simulations

In this section the experimental results and observations are compared with results from computer simulations. The values obtained by experiment (\bar{g}_{AA}^{00} , \bar{g}_{AB}^{00} , and \bar{g}_{AA}^{20}) are obtained directly from the molecular dynamics simulations by integrating the simulated spatial distribution function (Equation 2.27).

$$\bar{g}_{AA}^{00} \equiv \frac{2\pi N}{V} \int_0^\infty r^2 dr \int_{-1}^1 d \cos \theta_{1,2} (P_2(\cos \theta_{1,2}) \tilde{g}(r; \theta_{1,2})) \quad (2.27)$$

where $\tilde{g}(r; \theta_{1,2})$ is the scaled integral of the pair correlation $g(\omega_1 \omega_2 \mathbf{r})$ over the direction of the intermolecular vector, with $\theta_{1,2}$ denoting the angle between the \hat{c} axis and their intermolecular distance, r .

2.5.1 Benzene-benzene pair correlations

Table 2.3 shows benzene simulation results for five force fields at $T = 298$ K and $P = 1$ atm. It is clear that the experimental value is a very sensitive probe of the accuracy of force

fields; only the AMOEBA and DANG force fields give the correct sign for $\bar{g}_{benz-benz}^{00}$. These two are the only force fields in this group that use many body polarization effects.

Table 2.3. Calculated radial integral of leading tensor component of $g(\omega_1\omega_2r)$ with typical experimental constants used to discriminate force fields (ΔH_{vap} , density, and diffusion coefficient, D) for benzene.

force field	ΔH_{vap} (kcalmol ⁻¹) ^{a,c}	density (gcm ⁻³) ^b	D (10 ⁻⁵ cm ² s ⁻¹)	$\bar{g}_{benz-benz}^{00}$ ^b
	7.89 ³⁷	0.874 ³⁴	2.27	-0.16 ^d
AMOEBA ³⁸	7.91	0.879	1.74	-0.14
DANG ³⁹	7.91	0.878	1.64	-0.15
OPLS-AA ⁴⁰	7.82	0.870	1.82	+0.08
CHARM22 ⁴¹	7.91	0.872	1.92	+0.15
MM3 ¹⁴	7.78	0.873	2.68	+0.37

^aNVT simulations ^bNPT simulations ^c $\Delta H_{vap} = E_{gas} - E_{liq} + RT$ ^dExperiment (this work)

The negative sign is important because it indicates that the magnetic energy is higher for the benzene dimer (compared to a single benzene molecule). This is in agreement with simulations of the spatial distribution function using the AMOEBA force field (Figure 2.12), which predicts the most probable structure of the benzene dimer as a T-shape (i.e. ring planes are perpendicular to each other). The presence of T-shaped dimers in neat benzene means that benzene dimers cannot have their molecules simultaneously in the lowest magnetic energy orientation (i.e. with its C₆ axis perpendicular to the magnetic field). As a result the potential magnetic energy of the system is increased leading to a reduced S_{benz} , and therefore a reduced quadrupolar splitting. This is apparent from experiment where neat benzene has a splitting of 1.04₅ Hz which increases to 1.25 Hz as benzene is diluted with the magnetically isotropic molecule TMS. As more of the TMS diluent is added, the probability of realizing the T-shaped dimer is reduced, and more benzene molecules can realize their lowest magnetic energy orientation.

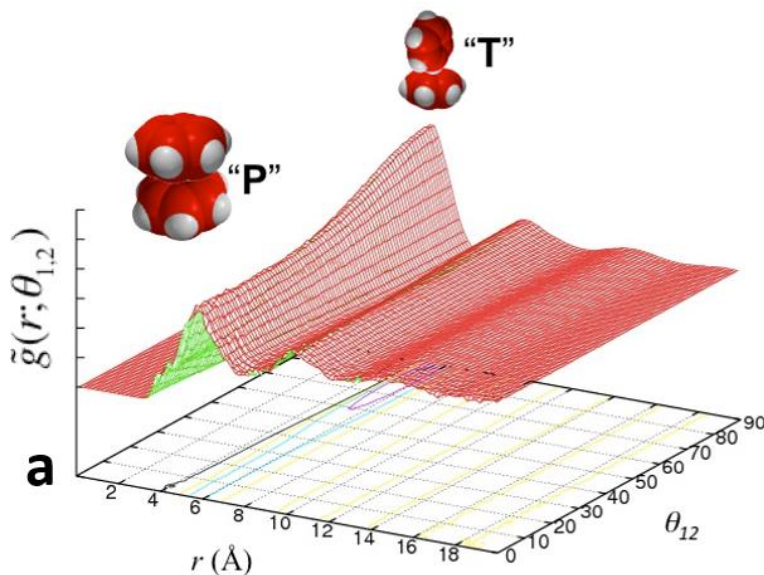


Figure 2.12. Spatial distribution function of benzene calculated with MD simulation using the AMOEBA force field. The two most probable dimer states are mutually perpendicular ring planes (T) and parallel ring planes (P).

In order to qualitatively assess the negative sign for $\bar{g}_{benz-benz}^{00}$, a “toy-model” of benzene is used where we look at two molecules of benzene and their corresponding dimer energies (we will call these molecules “molecule 1” and “molecule 2.” Instead of evaluating dimer energies by integrating over all the positions and orientations of molecule 2 relative to molecule 1, six positions are sampled by placing the center of molecule 2 along $\pm x, \pm y, \pm z$ at distances corresponding to the respective local minima of the intermolecular interaction. For each such position, three different orientations are sampled for molecule 2 relative to molecule 1: its ring-normal along the directions x, y, z . Consequently, there are 18 such dimer states. These fall into four categories to which statistical weights are assigned. For each dimer state, the components of the magnetizability tensor of molecule 2 are evaluated in the x, y, z frame of molecule 1 (molecule 1 has values of its magnetizability tensor

$\chi_{xx} = -1/2; \chi_{yy} = -1/2; \chi_{zz} = 1$ reduced to within a multiplicative factor. The results are

given in Table 4 where the dimer configuration names are “pd” for parallel displaced, “pf” for point faced, “cp” for co-planar, and “vt” for vertical (Figure 2.13).

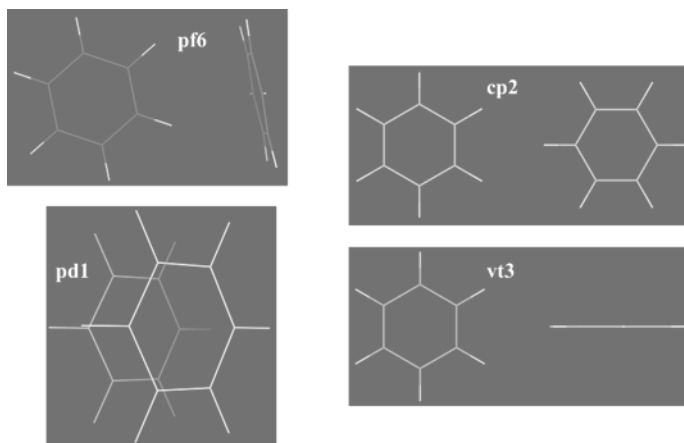


Figure 2.13. The four possible dimer configurations for two benzene molecules.

Table 4. Results of toy model for benzene. The first column gives the name of the dimer configuration (as depicted in Figure 2.13), the second column indicates the axis along which molecule 2 is placed, the third column indicates the axis along which the ring-normal of molecule 2 is directed, the fourth, fifth, and sixth columns indicate the reduced components of the magnetizability tensor of the molecule 2 in the molecular frame of molecule 1, the seventh column indicates the assigned weights for each of the four dimer states relative to the pd1 state (weight = 1), and the last column shows the multiplicity of each configuration from the equivalence of the (\pm) dispositions indicated in the second column.

Dimer state	CM position	Ring-normal	χ_{xx}	χ_{yy}	χ_{zz}	weight	multiplier
pd1	(\pm) z	z	-1/2	-1/2	1	1	2
pf6	(\pm) z	y	-1/2	1	-1/2	w_{pf6}	2
pf6	(\pm) z	x	1	-1/2	-1/2	w_{pf6}	2
cp2	(\pm) y	z	-1/2	-1/2	1	w_{cp2}	2
pf6	(\pm) y	y	-1/2	1	-1/2	w_{pf6}	2
vt3	(\pm) y	x	1	-1/2	-1/2	w_{vt3}	2
cp2	(\pm) x	z	-1/2	-1/2	1	w_{cp2}	2
vt3	(\pm) x	y	1	1	-1/2	w_{vt3}	2
pf6	(\pm) x	x	-1/2	-1/2	-1/2	w_{pf6}	2

The weighted sum of the magnetizability tensor components of all the 18 configurations of molecule 2 gives the average magnetizability tensor of the “molecular cage” surrounding molecule 1 as follows:

$$\langle \chi \rangle_{cage} = \kappa \begin{pmatrix} -1/2 & 0 & 0 \\ 0 & -1/2 & 0 \\ 0 & 0 & 1 \end{pmatrix} \quad (2.28)$$

with the proportionality factor κ determined from the relative weights according to the expression

$$\kappa = \frac{2(w_{cp2} - w_{pf6}) + (1 - w_{vt3})}{1 + 4w_{pf6} + 2w_{cp2} + 2w_{vt3}}. \quad (2.29)$$

The sign of κ indicates whether the effect of the “molecular cage” enhances ($\kappa > 0$) or weakens ($\kappa < 0$) the apparent coupling of molecule 1 to the magnetic field. For the benzene-benzene dimer, energies of pd1 and pf6 are approximately equal and are lower in energy than vt3 by a factor of 2 and cp2 by a factor of 5 meaning that $\kappa < 0$ and a weakening of the apparent coupling of molecule to the magnetic field results. This is in line with the negative value found experimentally for $\bar{g}_{benz-benz}^{00}$.

2.5.2 Chloroform-chloroform pair correlations

Table 2.4 shows chloroform simulation results for four force fields at $T = 298$ K and $P = 1$ atm.

Table 2.4. Calculated radial integral of leading tensor component of $g(\omega_1\omega_2r)$ with typical experimental constants used to discriminate force fields (ΔH_{vap} , density, and diffusion coefficient, D) for chloroform.

force field	ΔH_{vap} (kcalmol ⁻¹) ^{a,c}	density (gcm ⁻³) ^b	D (10 ⁻⁵ cm ² s ⁻¹)	$\bar{g}_{clfm-clfm}^{00}$ ^b
	7.50	1.489	2.45	+0.15 ^d
AMOEBA ³⁸	7.48	1.489	2.17	+0.15
DANG ³⁹	7.52	1.480	2.63	+0.07
OPLS-AA ⁴⁰	7.53	1.487	2.52	+0.19
MM3 ¹⁴	7.45	1.496	2.76	+0.14

^aNVT simulations ^bNPT simulations ^c $\Delta H_{vap} = E_{gas} - E_{liq} + RT$ ^dExperiment (this work)

Chloroform provides an example of a liquid with a positive value for \bar{g}^{00} meaning that pair correlations in chloroform enhance the magnetic alignment. This is in agreement with simulations of the spatial distribution function using the AMOEBA force field (Figure 2.14), which predicts the most probable structures of the chloroform dimer as parallel and antiparallel (low magnetic energy orientations).

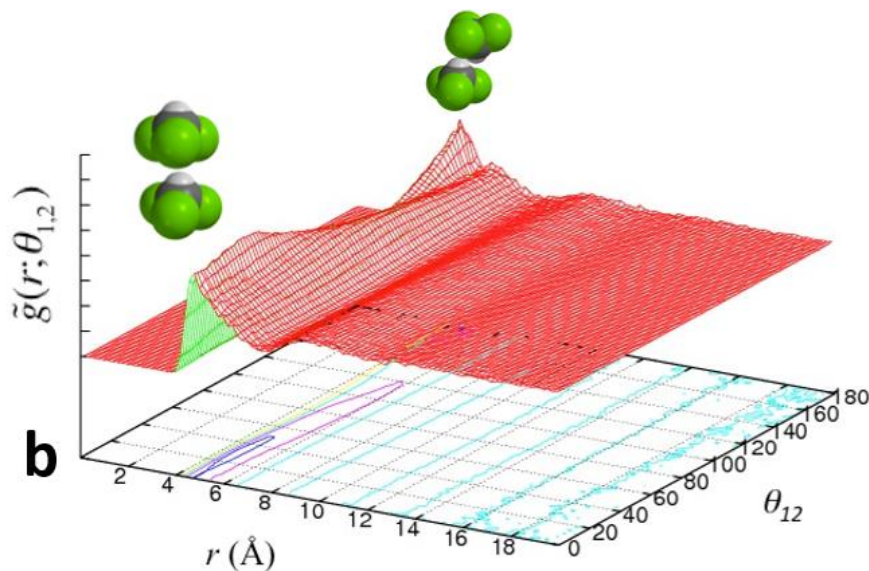


Figure 2.14. Spatial distribution function of chloroform calculated with MD simulation using the AMOEBA force field. The two most probable dimer states are parallel ($\theta_{1,2} = 0^\circ$) and antiparallel ($\theta_{1,2} = 180^\circ$).

2.5.3 The benzene/hexafluorobenzene complex

The motivation for investigating benzene/hexafluorobenzene mixtures was due to its interesting properties. A 1:1 mixture of benzene and hexafluorobenzene (0.5 mol fraction each) forms a solid at room temperature even though the melting points of benzene and hexafluorobenzene are 0.5° and -5.5°C , respectively.⁴² The complex has historically been explained as a Lewis base-Lewis acid or charge-transfer type complex.

In order to understand the origin of the benzene/hexafluorobenzene complex it is useful to discuss the molecular electric quadrupole moment and how it affects the solid-state architecture. The observed solid state structures of molecules with the same (a) and opposite (b) quadrupole moment configurations are shown in Figure 2.15.⁴³ The solid bar (main rotational axis) represents two like charges separated by opposite and balancing charges perpendicular to the main rotational axis.

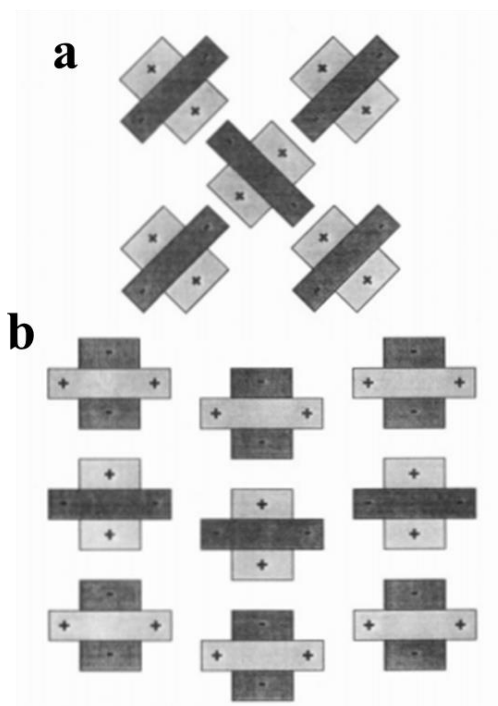


Figure 2.15. Schematic representation of the crystal structure between (a) identical quadrupolar molecules and (b) two quadrupolar molecules with opposite quadrupole moment configurations (from ref 43).

Benzene has a negative quadrupole moment of $-29.0 \times 10^{-40} \text{ Cm}^2$ and hexafluorobenzene has a positive quadrupole moment of $+31.7 \times 10^{-40} \text{ Cm}^2$.⁴⁴ The large negative quadrupole moment in benzene is due to the delocalized charge of electrons above and below the ring plane while the positive quadrupole moment of hexafluorobenzene is due to the high electronegativity of the fluorines on the periphery of the ring decreasing the electron density

in the center of the ring. Battaglia et al.⁴⁴ concluded that intermolecular polarization was the primary mechanism for the formation of the 1:1 benzene/hexafluorobenzene complex as opposed to it being a charge-transfer complex.

In summary, molecular quadrupole-quadrupole electrostatic interactions appear to underlie the benzene/hexafluorobenzene 1:1 complex; the observed solid state packing arrangement corroborates this.⁴³ Our experiment findings in solutions of benzene in hexafluorobenzene in conjunction with MD simulations in the 1:1 mixture (Figure 2.16) suggest that the electrostatic quadrupole-quadrupole interactions dominate the local liquid state structure. While neat benzene has a negative pair correlation factor, $\bar{g}_{benz-benz}^{00} = -0.16$, benzene in hexafluorobenzene has a pair correlation factor, $\bar{g}_{benz-C_6F_6}^{00} = +2.1$. This large positive value indicates that the magnetic alignment of benzene in the 1:1 complex is enhanced relative to neat benzene. This is displayed by the spatial distribution function calculate using MD simulations in Figure 2.16. The dimer state where the ring planes of benzene and hexafluorobenzene are parallel to each other is the most probable based on simulation whereas the “T-shaped” dimer found for benzene has near zero probability for the 1:1 mixture of benzene and hexafluorobenzene.

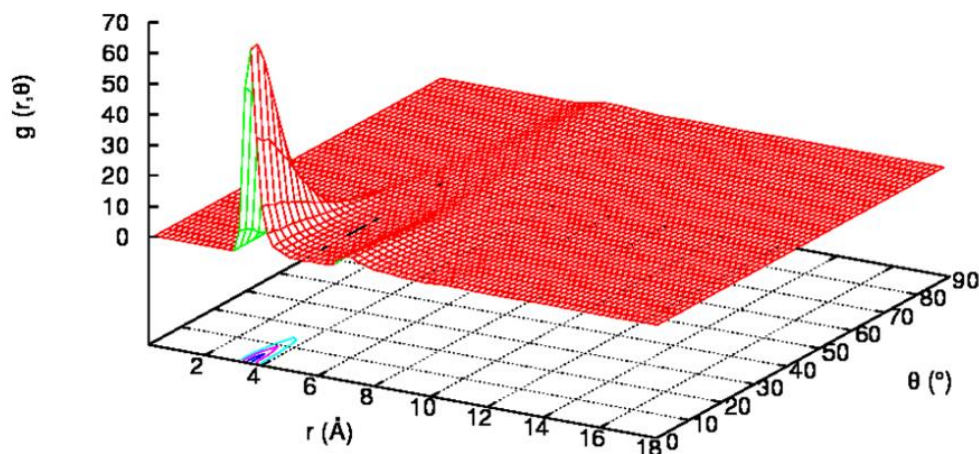


Figure 2.16. Spatial distribution function of chloroform calculated with MD simulation using the AMOEBA force field. The most probable dimer state is overwhelming parallel ($\theta_{1,2} = 0^\circ$).

2.5.4 Insights from chloroform-d/benzene mixtures

Another interesting complex is the chloroform/benzene complex. In 1957, Reeves and Schneider showed using ^1H NMR that the chloroform molecule in the chloroform/benzene complex was oriented with its hydrogen atom near the plane of the aromatic ring.⁴⁵ In 1969, Huntress described the anisotropic reorientation of CDCl_3 in mixtures with benzene using ^2H nuclear spin relaxation studies.⁴⁶ In the 2000s interest in this complex resurfaced and efforts to prove or disprove the presence of this complex in the liquid state using MD simulations began. Rothschild^{47,48} concludes that the structure proposed by earlier researchers like Reeves and Schneider (with H atom of chloroform pointing towards the center of the ring plane of benzene) has a “near-vanishing” probability to exist in solution.

Our results actually provide evidence for the existence of the “hydrogen bond”-like structure of the chloroform/benzene structure in which the hydrogen of chloroform forms a weak hydrogen bond with the π -orbitals of benzene acting as donors.⁴⁵ The splitting for neat

chloroform (~ 0.52 Hz) goes down by about half (~ 0.26 Hz) when benzene is added in a 1:1 ratio, which indicates that chloroform is less likely to assume its lowest magnetic energy configuration.

2.6 Conclusions

For the prototypical liquids benzene and chloroform, it is clear that the NMR method for calculating the leading second rank tensor component is robust. Comparing the experimental pair correlation factors to the computational results for benzene using the force fields in Table 2.3 suggest that the NMR method does an excellent job of discriminating against force fields. Alternately, comparing the experimentally derived pair correlation value of chloroform to the MD simulation results in Table 2.4 show little discrimination between force fields. However, for benzene some force fields do not calculate the correct sign of \bar{g}^{00} , while other experimental parameters (e.g. heat of vaporization, density, and diffusion coefficient) do not show much difference between force fields. Similarly, experimental radial distribution function from neutron scattering⁴⁹ and carbon-carbon atom-atom correlation function from X-ray scattering⁵⁰ compared to the MD simulation data that shows no appreciable difference between force fields. The MD simulated radial distribution functions for different force fields and comparisons with neutron and X-ray scattering are provided in the Supplementary Information of our *Journal of Physical Chemistry Letters* article.³⁶

Building on the promising the results of benzene and chloroform, the method was also successfully extended to mixtures with specific electrostatic interactions (e.g. mixtures of benzene and hexafluorobenzene and mixtures of chloroform and benzene) and liquids with lower molecular symmetry. With the advent of higher field NMR instruments,¹⁸ the NMR

method described here will enable the discrimination of force fields for a host of chemical systems as well as the ability to explore the subtleties of liquid-state structure in these systems.

CHAPTER 3: N_x PHASE OF CYANOBIPHENYL DIMERS

3.1 Introduction

3.1.1 Shape Anisotropy and Liquid Crystal Phases

Liquid crystal shape anisotropy was introduced in Chapter 1. Some of the fluid phases that can be formed from the primary molecular shapes in Figure 1.1 are described here. The simplest liquid crystalline phase formed by calamitics is the nematic (N) (Figure 3.1) where the **l**-axis is on average parallel to the director, **n**, but has translational (positional) disorder; note that Figure 3 consists of idealized “cartoons” of the molecular arrangements in liquid crystals. The more complex smectic phase has its **l**-axis parallel to **n** as in the nematic phase, but includes some degree of translational order or “layering”. Multiple variations of the smectic phase exist: Two common phases are the smectic A (S_A) and smectic C (S_C) and they differ in the angle that the director makes with respect to the layer normal. In S_A, **n** is on average perpendicular to the layers and in S_C, **n** makes an angle α with respect to the layer normal. Other smectic phases are possible⁵¹ including a cubic arrangement (S_D) that is manifested in “blue-phases” exhibited by chiral nematics. Chiral nematics are described in Section 3.1.2.

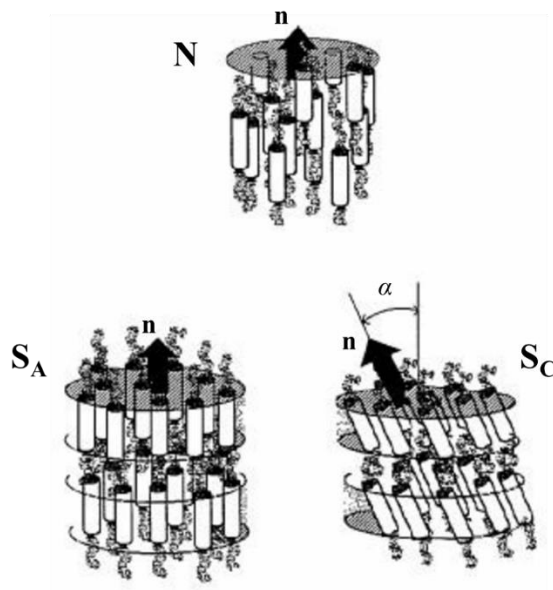


Figure 3.1. Examples of phases formed from calamitic mesogens: uniaxial nematic (N), uniaxial smectic-A (S_A) and biaxial smectic-C (S_C). Reproduced from ref 2.

Most phases formed by discoids draw analogies to the calamatic phases described previously. Discoids also can form a uniaxial nematic phase (D_N) in which the mesogen symmetry axis (in this case \mathbf{m}) is parallel to the director, \mathbf{n} . Layered phases are also possible including the discotic hexagonal ordered (D_{ho}) and discotic hexagonal disordered phases (D_{hd}) where the disk-shaped mesogens stack into columns (Figure 3.2).

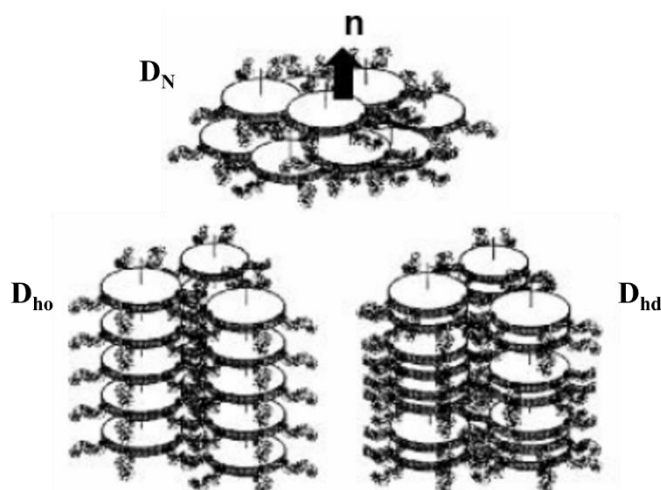


Figure 3.2. Examples of phases formed from discotic mesogens: nematic (D_N), hexagonal ordered (D_{ho}), and hexagonal disordered (D_{hd}). Reproduced from ref 2.

The intermediate non-linear or bent mesogens are less understood, but have garnered significant attention in recent years. These can be characterized as banana or “B” phases.⁵² The biaxial nematic is one mesophase exhibited by certain bent-core molecules.⁵³ This phase is characterized by translational disorder with two directors, **n** and **o**.

3.1.2 Chiral phases

Additional variation in the supramolecular organization of ordered phases is realized if a mesogen is chiral. The most common chiral nematic is the cholesteric phase (Figure 3.4c) in which the fluid phase often denoted N^* is made up of chiral molecules. The cholesteric is a twisted phase in which molecules are twisted slightly with respect to neighboring molecules. The director traces out a macroscopic “spiral” or helix and rotates through 180° after traversing a distance $P/2$ (one-half of the characteristic pitch length, P) in the N^* phase. The twist of the spiral is either right- or left- handed depending on the sense of the chiral center of the mesogen, levo or dextro-rotatory.

3.1.3 Nematic phases of non-linear cyanobiphenyl dimers

In an effort to better understand the oriented phases of non-linear mesogens, significant research has been performed on liquid crystal dimers. Figure 3.3 shows an example of a liquid crystal dimer contains two semi-rigid mesogenic units connected by a central flexible linker.

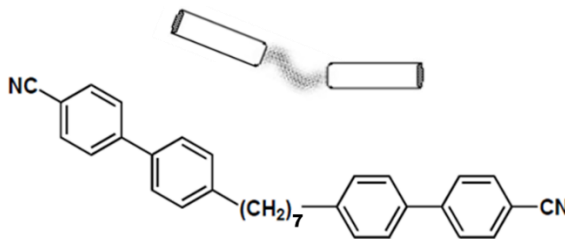


Figure 3.3. Approximate shape of a non-linear liquid crystal dimer and structure of CB-C7-CB.

The cyanobiphenyl dimers (CB-C_n-CB), where *n* is the length of the alkyl chain spacer, were first synthesized in the late 1980's at the Department of Chemistry at the University of Tokyo.⁵⁴ Subsequently, in 1991, Hiro Toriumi first reported⁵⁵ the nematic-nematic (N – N_X) phase transition in "odd dimers" CB-C_n-CB where *n* is an odd number; personal crises delayed the manuscript revisions suggested by the referee, and this seminal paper was never published. The liquid crystal dimer example in Figure 3.3 is the symmetric 1'',7''-bis(4-cyanobiphenyl-4'-yl)heptane or CB-C7-CB.

In addition to molecular shape (described in **Section 3.1.1**), molecular structure is also an important factor in determining organization of liquid crystalline phases; for example molecular flexibility (i.e. the tail in calamitic liquid crystals and flexible linker in dimer liquid crystals). The length and number of C—C bonds in the flexible linker has a significant bearing on the properties of the liquid crystal. For example, in dimers with very short core alkyl chains, the mesogen behaves like a rigid molecule, but for very long alkyl chains the

mesogenic groups become uncoupled and the dimer character of the mesogen goes away and properties are almost identical to the monomeric form. The number of C—C bonds also has a significant effect on properties. Dimers with an even number of units in the flexible linker have higher transition temperatures and higher transitional entropies than corresponding odd-dimers (i.e. CB-C6-CB and CB-C8-CB have much higher transition temperatures than CB-C7-CB); termed the odd-even effect. The origin of this difference comes from the fact that different anisotropic shapes are allowed for odd vs. even dimers.⁵⁶

Perhaps the most significant difference between odd and even dimers is the existence of an additional lower temperature nematic phase, N_X , described originally by Toriumi.⁵⁵ The nature of this phase is still under significant debate. Efforts to describe this phase have increased significantly in recent years ever since the first paper to describe the new nematic phase as a “twist-bend” nematic, N_{TB} .⁵⁷ The authors claim that in addition to CB-C7-CB experiencing an isotropic to nematic transition at a much lower temperature than its even dimer counterpart, certain odd cyanobiphenyl dimers exhibit a second, lower temperature nematic phase that is a new chiral nematic phase with a “twist-bend” distribution of directors (Figure 3.4b taken from ref 58) predicted in 1973 by Meyer⁵⁹ and Dozov⁶⁰ in 2001. Dozov also predicted that the twist-bend nematic should separate into chiral domains.

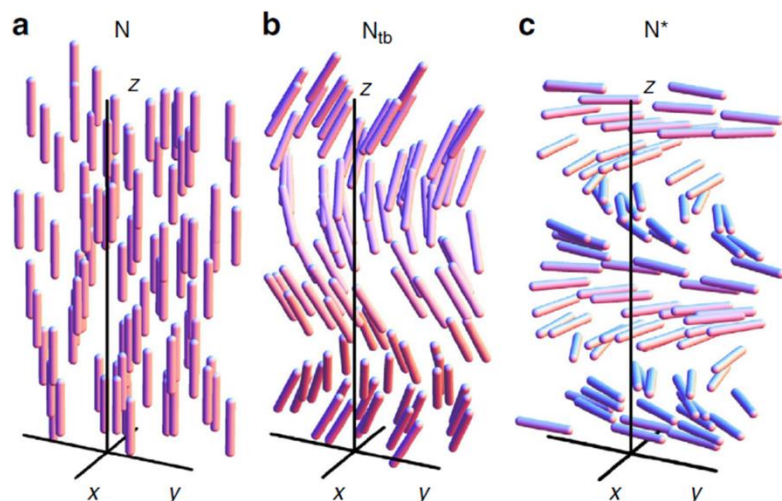


Figure 3.4a. Uniaxial nematic phase, N, **b.** twist-bend nematic phase, N_{TB} , and **c.** chiral nematic phase, N^* (from ref 58).

3.1.4 Experimental determination of the twist-bend nematic phase

Many attempts (experimental and computational) to describe the nature of the proposed twist-bend nematic phase have taken place.^{57,58,61–66} Findings include the observation of textural features in depolarized transmission light microscopy (DTLM) similar to those found in smectic phases, but X-ray diffraction does not show periodic variations of electron density suggesting that the center of masses are randomly distributed, and atypical elastic behavior is found. The chirality of the phase has also been demonstrated. Some of these efforts are summarized in the following sections.

3.1.4.1 Microscopy (FFTEM, Optical Microscopy)

Optical properties of liquid crystals are important in understanding the structure of oriented phases and are manifested due to birefringence (refractive index anisotropy). Liquid crystal phases are typically viewed under optical polarizing microscopes between two glass plates (a cell) that may or may not have surface treatments for aligning the director. If the

surface is treated such that the molecular director is aligned parallel to the glass surface, it is called a planar cell (homogeneous alignment) and if the surface is treated such that the molecular director is aligned perpendicular to the glass surface, it is called a homeotropic cell (heterogeneous alignment).

The so called “schlieren” texture is characteristic of the uniaxial nematic phase in a planar cell (Figure 3.5a). Focal conic textures appear in liquid crystals with one degree of positional order and are consistent with smectic and chiral nematic phases. An example of a focal conic texture for the chiral nematic (N^*) phase is given in Figure 3.5b for a cell with no preferred alignment direction.

The proposed N_{TB} phase draws some comparisons to the N^* phase and it has been proposed that focal conic textures should be expected in a twist-bend nematic phase, but features are on the order of nanometers and the pitch cannot be detected optically.⁵⁸ Textures observed by Borshch et al.⁵⁸ from planar cells are were on the order of microns, but they concluded that the textures were not thermodynamically stable indicating the possibility of submicron features. Other groups have observed focal conic defects in the N_X phase of odd cyanobiphenyl dimers and is the most characteristic texture although other textures are possible depending on sample preparation and thermal hysteresis.⁵⁷ Focal conic textures give unequivocal evidence of structure periodicity or “layering”- not necessarily smectic layering although smectic phases often possess focal conic textures as well. Layering can also be due to helices (as in chiral nematics) or any other periodic structure.⁶⁷

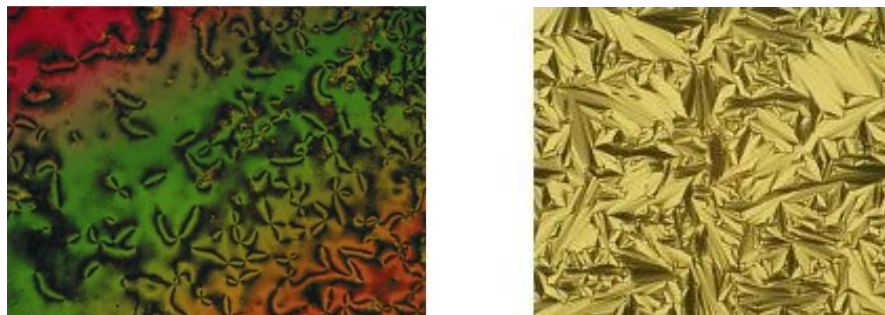


Figure 3.5a. Schlieren texture of the uniaxial nematic phase of a liquid crystal (N) **b.** Focal conic texture of the chiral nematic phase of a liquid crystal (N*) when viewed under a polarizing optical microscope. From ref 68.

One way to view submicron features in the N_x phase is with freeze-fracture transmission electron microscopy (FFTEM) and such studies were used to demonstrate the proposed twist-bend nematic phase's helical pitch on the order of a few molecular lengths ($\sim 8\text{nm}$) for CB-C7-CB.^{58,66} The material is cooled from the isotropic phase into the N_x phase and quenched in liquid nitrogen for TEM studies. Chen et al.⁶⁶ report striped fracture planes which they attribute to periodic modulation of the fluid layers with spacing of $\sim 8.3\text{nm}$. Similarly, Borshch et al.⁵⁸ find a pitch length of 8.05nm for CB-C7-CB with FFTEM. Both studies conclude that the N_x phase is characterized by a periodic modulation of the tilted director with a pitch length of $8\text{-}9\text{ nm}$.

3.1.4.2 Elastic constants in nematic phases

Nematics display elastic behavior when deformed by external forces; the resistance to such forces is described by elastic constants named by the type of deformation performed ($K_1=\text{splay}$, $K_2=\text{twist}$, and $K_3=\text{bend}$). Deformations (strain) of the nematic result in a restoring force (stress)² and elastic constants are the constants of proportionality between strain and stress and are important measures of the variation of the director with respect to applied external forces (important to liquid crystal displays, LCDs) or in this case, elastic

constants are a probe of microscopic structure⁶⁹ and describe the torques necessary to obtain related splay, twist, and bend deformations.

In Borshch et al.,⁵⁸ K_1 and K_3 were measured for a mixture of dimer and monomer added for ease of experimentation (higher degree of alignment, lower viscosity, and observation temperature). The researchers call this mixture “M2” and the structures are shown in Figure 3.6. K_1 followed typical behavior for uniaxial nematics while K_3 reached values lower than typical uniaxial nematics as the temperature was decreased toward the $N-N_X$ transition.

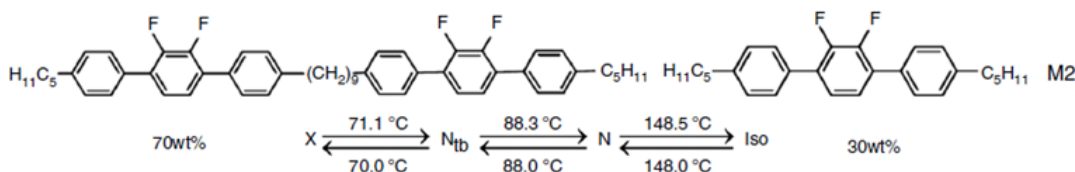


Figure 3.6. Structure and phase transition map for M2. From ref 58.

Studies on M2 were performed in homeotropic and planar cells with nematic directors aligned perpendicular and parallel to the substrate, respectively. When a field is applied parallel to the director in homeotropic nematic cells, the director begins to tilt above some threshold voltage (U_{th}) which is proportional to the square of K_3 . In the nematic phase of M2 once the applied field exceeds U_{th} , the optic axis realigns everywhere in the nematic phase, but in the N_X phase the reorientation occurs at isolated sites and show that the tilt is at a maximum at the venter of the domain reminiscent of S_A and N^* phases. This strange behavior of the dielectric response gives evidence for the periodic nature of the N_X phase at scales smaller than the wavelength of visible light.⁵⁸

3.1.4.3 Experimental determination of chirality

Although the dimeric mesogens in cyanobiphenyl dimers are achiral, the lower temperature nematic phase formed by the dimers is chiral. The chirality of the low temperature nematic phase described previously was demonstrated by Beguin et al.⁶⁴ with NMR.

The analysis of chirality in LC phases with ^2H NMR relies on the concept of prochirality and was first demonstrated by Czarniecka and Samulski.⁷⁰ Chirality in liquid crystalline phases can be detected with a solute containing a prochiral group. It is important that the solute is prochiral (as opposed to a chiral solute) because adding a chiral solute to an achiral liquid crystal can induce chirality.

Prochiral molecules are molecules that can become chiral in one substitution step. For example Figure 3.7 displays a generic tetrahedral molecules with a carbon atom and four substituents, two of them being the same atom. If one of the “H” atoms is replaced with a third substituent (different from “X” and “Y”), the molecule would become chiral. Because the quadrupolar splitting, $\Delta\nu$, is related to the C–D bond order parameter, S_{CD} , the quadrupolar splitting of deuterons attached to a prochiral center can detect chirality if dissolved in a chiral nematic phase.

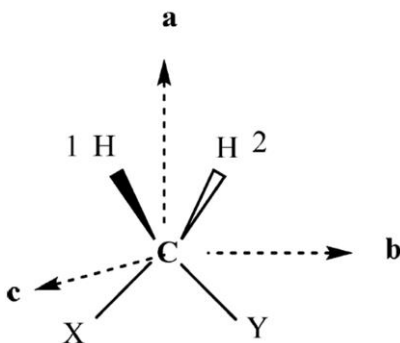


Figure 3.7. Prochiral molecule where X and Y substituents are different.

For a single enantiomer (either + or -), a maximum difference in $\Delta\nu$, $\Delta(\Delta\nu)$, will be observed. The ^2H spectrum of a prochiral molecule dissolved in a (+) enantiomer will be identical to that of the (-) enantiomer because the sign of $\Delta(\Delta\nu)$ will change, but the magnitude will not. For a racemic mixture of (+) and (-), the prochiral splitting disappears and for any enantiomeric mixture other than 50% (+) and 50% (-), a nonzero $\Delta(\Delta\nu)$ is observed. If diffusion of prochiral molecules is slow (compared to $\Delta(\Delta\nu)$) prochiral splitting is unaffected and NMR spectra are identical in either domain. Therefore, if a maximum quadrupolar splitting is observed for a prochiral molecule it can be caused by either the presence of a uniformly handed chiral phase or a mixture of levo or dextro-rotatory domains with slow diffusion between domains.⁷¹

3.1.5 An alternative structure for the N_X phase of odd cyanobiphenyl dimers

Recently, the twist-bend picture of the N_X phase has been called into questions by two key experimental studies; the first using atomic force microscopy (AFM)⁶⁷ and the second using NMR.⁷²

Gorecka et al.⁶⁷ show with AFM measurements that the 8nm periodicity found with FFTEM (attributed to the extremely short helical pitch director modulation proposed for the N_{TB} phase) is very close to that of the crystalline phase of odd cyanobiphenyl dimers which may indicate the presence of surface freezing. The Mehl group used AFM to re-investigate the FFTEM measurements described here in Section 3.1.4.1. CB-C7-CB was placed between two substrates, cooled to the N_X phase from the isotropic phase and quenched in liquid nitrogen followed by removal of one of the substrates and AFM analysis at room temperature. Optical observation showed that CB-C7-CB, in the N_X phase after quenching in liquid nitrogen and warming to room temperature, had smooth textures with mostly focal

conic defects and that the phase was stable at room temperature for less than one hour, but significantly longer than for dimers with longer alkyl spacers, which allowed for AFM observation during this time window.

In the N_X phase, focal conic “parabolas” were covered with layering lines separated by $\sim 8\text{nm}$ (Figure 3.8, left). In the crystal phase region (Figure 3.8, right) the focal conic defects are absent, but the nanoscale periodicity remains. Not only is the periodicity almost the same in the crystalline regions and N_X regions, this is also very close to the periodicity observed with TEM.^{58,66} Therefore, it is possible that the $\sim 8\text{nm}$ periodicity observed with AFM and TEM is evidence for the formation of a solid or smectic phase on the surface.

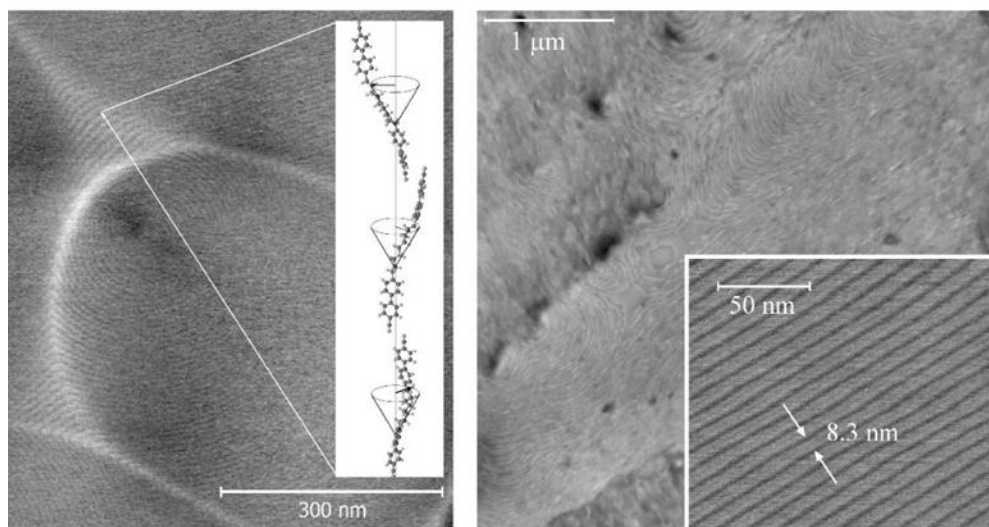


Figure 3.8. AFM images of (left) the N_X phase showing a focal conic domain covered with layers spaced $\sim 8\text{nm}$ apart with the crystallographic structure (right) the crystalline phase showing clear evidence of 8.3 nm periodicity of the crystallographic planes. From ref 67.

In the NMR investigation by Hoffman et al.,⁷² the presence of chiral domains in the N_X phase of CB-C9-CB is demonstrated, but the picture of molecules having a twist-bend variation of the director is called into question by a key NMR experiment. The authors also point out that key assumptions made in developing the model for the twist-bend phase are of

questionable validity. Specifically, the twist-bend spatial distribution of the direction in the proposed NTB phase is given in Equation 3.1, where the pitch, $P = 2\pi/k$ and θ_0 is the tilt angle between \mathbf{n} and Z , and is in line with the theoretical proposal laid out by Dozov which is partially based on the continuum theory of elasticity for the nematic phase.

$$\mathbf{n}(Z) = (\sin\theta_0 \cos kZ, \sin\theta_0 \sin kZ, \cos\theta_0) \quad (3.1)$$

However, if the director in the N_{TB} phase is said to reorient by $2\theta_0$ over $P/2$ ($P/2 \sim 4\text{nm}$ or one to two molecular lengths), then this proposal is no longer valid because the continuum theory assumes very small variation in the director with distance.⁷³ In a different report by the Photinos group, they demonstrate with computer simulations that bent-core molecules similar to odd cyanobiphenyl dimers form chiral domains that spontaneously aggregated into larger helical structures.⁷⁴

The key NMR experiment performed by Hoffman et al.⁷² involves viewing the N_X phase of CB-C9-CB (deuterated at the first methylene, α positions) after rotation of the alignment direction by 90° and before reorientation occurs in the magnetic field; this is possible due to the high viscosity of the N_X phase of CB-C9-CB. Figure 3.9a shows a ^2H NMR spectrum of deuterated CB-C9-CB in the N_X phase before (red) and after (blue) rotation of the sample by 90° . Figure 3.9b shows the effect of the rotation if the hypothetical twist-bend configuration is assumed. It is clear that the spectra in Figure 3.9a cannot be attributed to the hypothetical configuration in Figure 3.9b. If we assume the hypothetical twist-bend figure then the director makes an angle θ_0 with the magnetic field, B_0 .

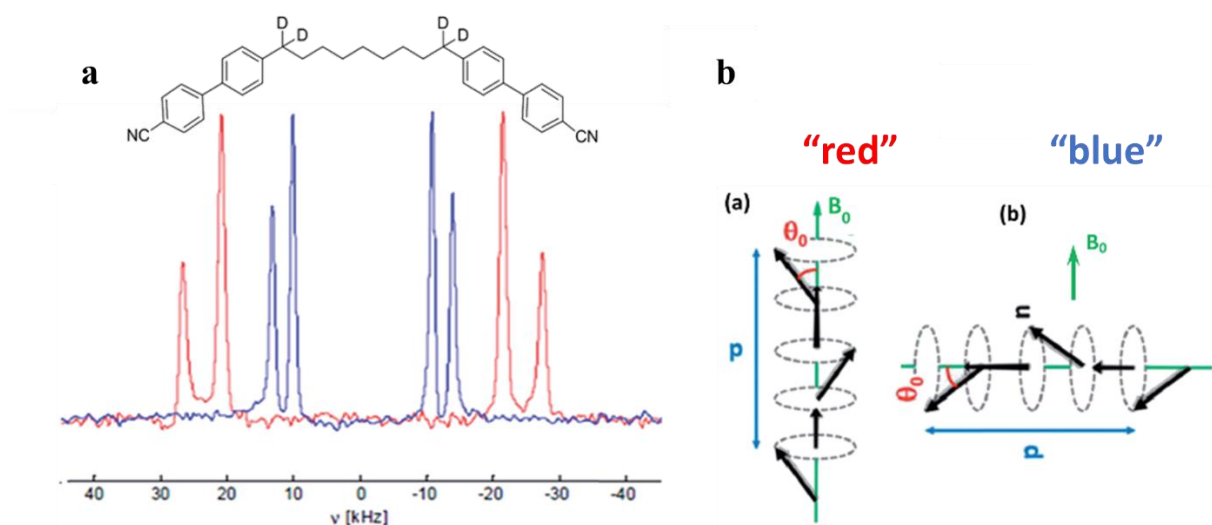


Figure 3.9a. ^2H NMR of the N_X phase of deuterated CB-C9-CB (pictured) before (red) and immediately after (blue) rotation of the sample by 90° . **b.** A hypothetical picture of the proposed twist-bend confirmation undergoing a rotation by 90° . From ref 72.

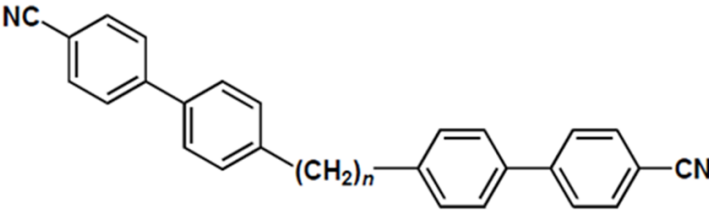
Once the sample is rotated by 90° then the spectrum should show a superposition of peaks corresponding to the distribution of angles the director makes with the magnetic field, $\theta_{n,H}$ of which the values $\pi/2 - \theta_0 < \theta_{n,H} < \pi/2 + \theta_0$ are possible. This is not the case as the spectrum does not exhibit any broadening. In fact, the spectrum indicates a cylindrical distribution of the director that remains after rotation by 90° .

Clearly, the structure of the N_X phase of odd cyanobiphenyl dimers is still under considerable debate. Additional NMR studies are helpful in further elucidating the N_X structure and those efforts are described in the remaining sections. The order parameter of the cyano group, i.e., the orientation of the $-\text{CN}$ bond (para axis) of the cyano-biphenyl terminated alkyl “spacer” with n methylene carbons, $\text{CB-C}_n\text{-CB}$, and the ordering of the solute decane- d_{22} was determined using carbon and deuterium NMR respectively for varying values of n .

3.2 Experimental Methods

3.2.1 Materials

The materials used in this study are cyanobiphenyl dimers with alkyl spacers (CB-Cn-CB) with $n = 7, 9, 10, 11$ and were synthesized by the Mehl group at the University of Hull according to the synthetic details outlined in ref 75 and described in other studies of CB dimers.^{58,61,67,72} Transition temperatures were taken from DSC heating and cooling data also from the Hull group and are given in Figure 3.10.⁷⁶ Samples of 2 wt % decane-d₂₂ in CB-Cn-CB (i.e. 4.5 mg decane-d₂₂ in 216.4 mg for CB-C11-CB) were placed in normal wall (0.8 mm) 5mm O.D. NMR tubes. The samples were degassed using a freeze-pump-thaw method three times. The CB-C11-CB, CB-C9-CB, CB-C7-CB, CB-C10-CB, and 5-CB samples were prepared this way.



Compound	n	Phase transitions
CB-C7-CB	7	Heating: Cr 102 N _X 104 N 116 Iso (°C) Cooling: Iso 116 N 103 N _X <30 Cr (°C)
CB-C9-CB	9	Heating: Cr 85 N _X 108 N 124 Iso (°C) Cooling: Iso 123 N 107 N _X 52 Cr (°C)
CB-C10-CB	10	Heating: Cr 140 N 172 Iso (°C) Cooling: Iso 169 N 118 Cr (°C)
CB-C11-CB	11	Heating: Cr 105 N _X (84) N 125 Iso (°C) Cooling: Iso 124 N 106 N _X 84 Cr (°C)

Figure 3.10. Chemical structure and respective transition temperatures of CB-Cn-CB for $n=7,8,9,10,11,12$, taken from the first DSC heating scans and cooling scans (10 Kmin⁻¹).⁷⁶

3.2.2 NMR Methods

^2H NMR spectra of decane- d_{22} dissolved in CB-Cn-CB (2 wt %) were recorded at 55.3 MHz (Bruker DMX360 FT NMR spectrometer). The sample was mixed in isotropic phase, introduced into the spectrometer, and after equilibration to the desired temperature 5000 scans (free induction decays) were averaged with a spectral width of 100 kHz. A quad echo pulse sequence (Figure 3.11) was used with a 90° pulse width of $2\text{ }\mu\text{s}$ and 100 ms recycle time.

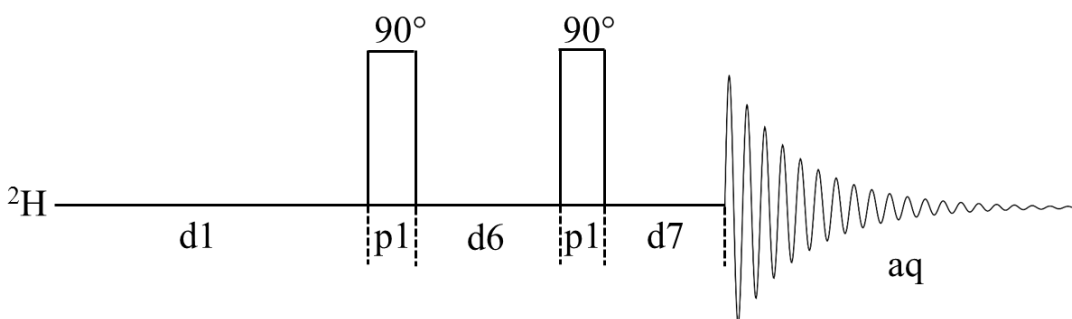


Figure 3.11. ^2H NMR Quad echo pulse sequence where 90° pulses ($p1$ at power level 5 dB) were calibrated to $2\text{ }\mu\text{s}$, $d1$ (recycle time) is 100 ms, $d6$ is $18\text{ }\mu\text{s}$ and $d7$ is $10\text{ }\mu\text{s}$.

Using the same sample (CB-Cn-CB with 2 wt% decane- d_{22}), ^{13}C NMR spectra were recorded at 90.6 MHz (Bruker DMX360 FT NMR spectrometer). The sample was introduced into the spectrometer, and after equilibration to the desired temperature 1000 scans (free induction decays) were averaged with a spectral width of 36 kHz. An inverse gated pulse sequence (^1H decoupled during acquisition time, Figure 3.12) was used with a 90° pulse width of $11\text{ }\mu\text{s}$ and 2 s recycle time. The same procedure was implemented for all CB-Cn-CB dimers and 5-CB.

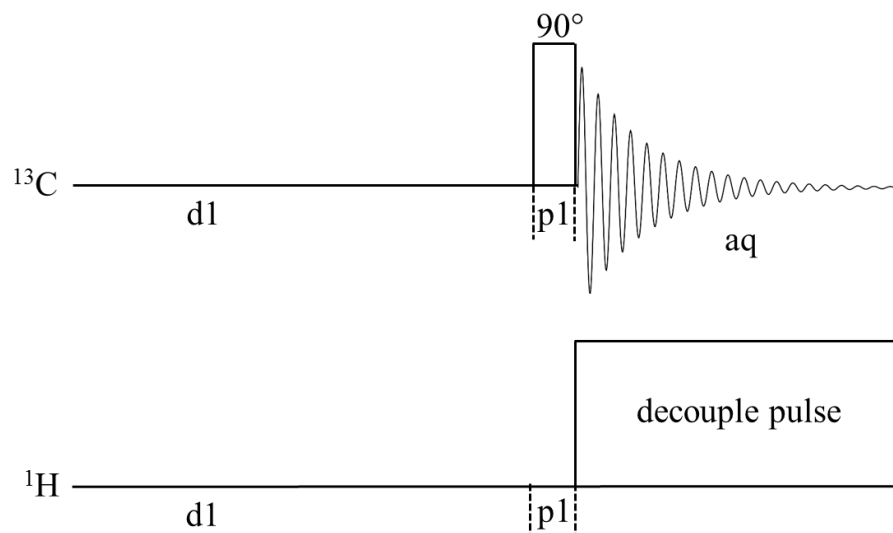


Figure 3.12. Inverse gated ^1H decoupled ^{13}C NMR pulse sequence. The recycle time (d1) is 2 s and the ^{13}C 90° pulse width is equal to 11 μs . The ^1H pulse (0 dB) is on during the acquisition time (56.6 ms)

3.3 Results and Discussion

3.3.1 ^2H NMR of Liquid Crystals

The nuclear quadrupole coupling manifests itself in ^2H NMR and described in Section 1.4.1; the quadrupolar splitting is given in terms of the orientation of the molecular symmetry axis by Equation 3.2 where ν_Q is the quadrupolar coupling constant, θ is the angle that the C—D bond makes with the molecular symmetry axis, and S is the order parameter describing the degree of order of the molecular symmetry with respect to the magnetic field \mathbf{B}_0 .

$$\Delta\nu = \frac{3}{2}\nu_Q P_2(\cos\theta)S. \quad (3.2)$$

3.3.2 Deuterated probes dissolved in liquid crystals

If a deuterated alkane is dissolved in a liquid crystal phase, the molecular organization of the mesogens can be inferred from the ^2H NMR of the alkane. In the present

study, decane-d₂₂ was used because its boiling point (192°C) is much higher than the transition temperatures for any of the cyanobiphenyl dimers studied here. Additionally, the methylene deuterons of decane-d₂₂ are prochiral, so the chirality of the phase can be assessed similarly to the methods described in **Section 3.1.4.3**.

Figure 3.13 shows the ²H NMR spectra of decane-d₂₂ in CB-C11-CB for selected temperatures given in reduced temperature, T/T_{NI} , where T_{NI} is the temperature at which the transition from isotropic to nematic occurs. In Figure 3.14, the quadrupole splitting of the methyl and α -methylene (adjacent to methyl) of decane-d₂₂ are plotted against reduced temperature. Because the quadrupole splitting is related to the order of the molecule (Equation 3.2), it is indicative of the ordering in a particular phase. As the temperature is decreased into N_x phase, the slope of the temperature dependence of the splitting increases, but there is no doubling of the quadrupolar splitting to indicate chirality.

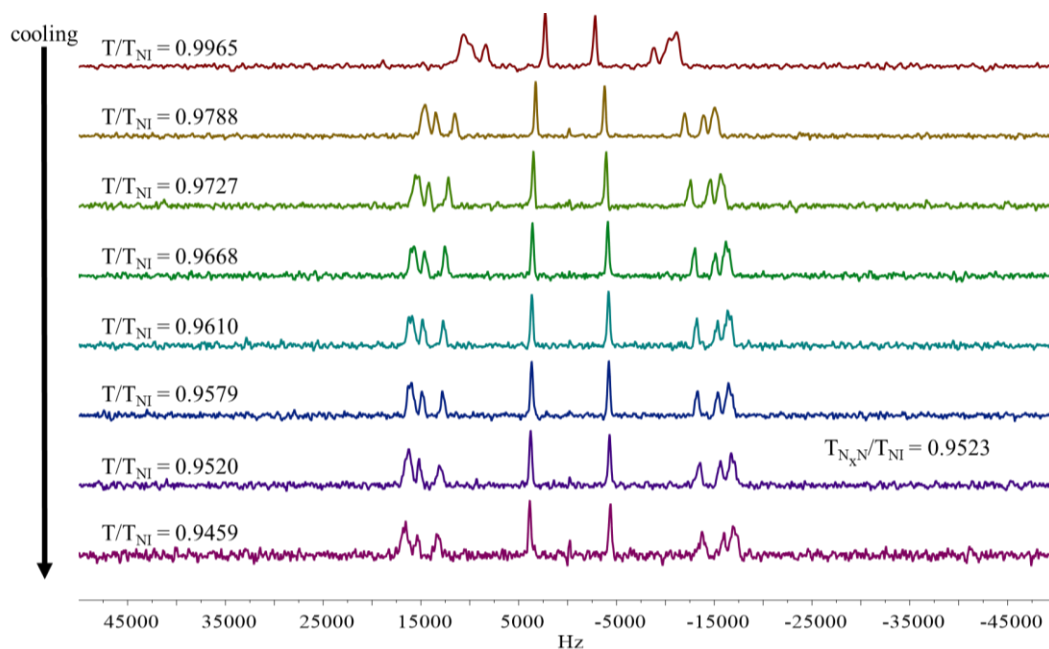


Figure 3.13. ²H NMR spectra of decane-d₂₂ in CB-C11-CB at decreasing temperatures (from top to bottom) The N_x-N transition is noted and occurs at a reduced temperature of 0.9523.

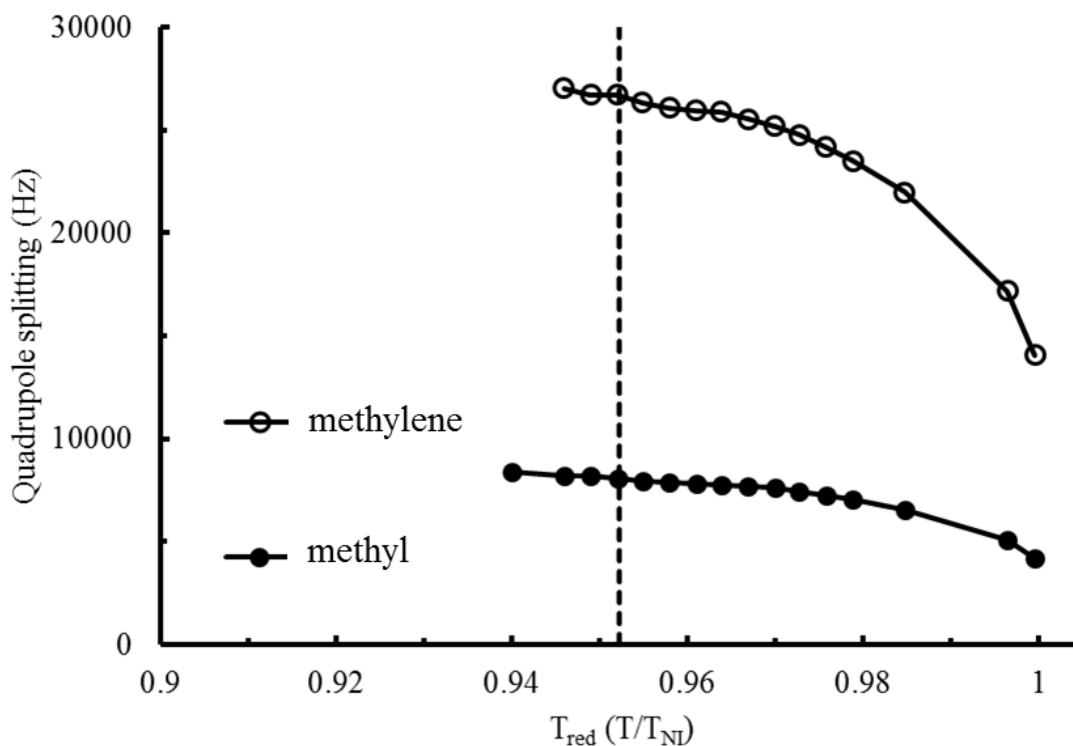


Figure 3.14. The temperature dependence (in reduced temperature) of the quadrupole splitting of the methyl and methylene group of decane- d_{22} in CB-C11-CB with the N to N_x phase transition shown as dotted line.

Once the spacer length is reduced from 11 to 9, the α -CD₂ peaks become doubled upon cooling into the N_x phase. It is presumable that the CB-C11-CB α -CD₂ would also be doubled, but the doubling is smaller than the resolution of the peaks. ²H spectra for selected temperatures and a plot of the quadrupole splitting of the methyl and α -methylene of decane- d_{22} against reduced temperature for CB-C9-CB are shown in Figures 3.15 and 3.16, respectively.

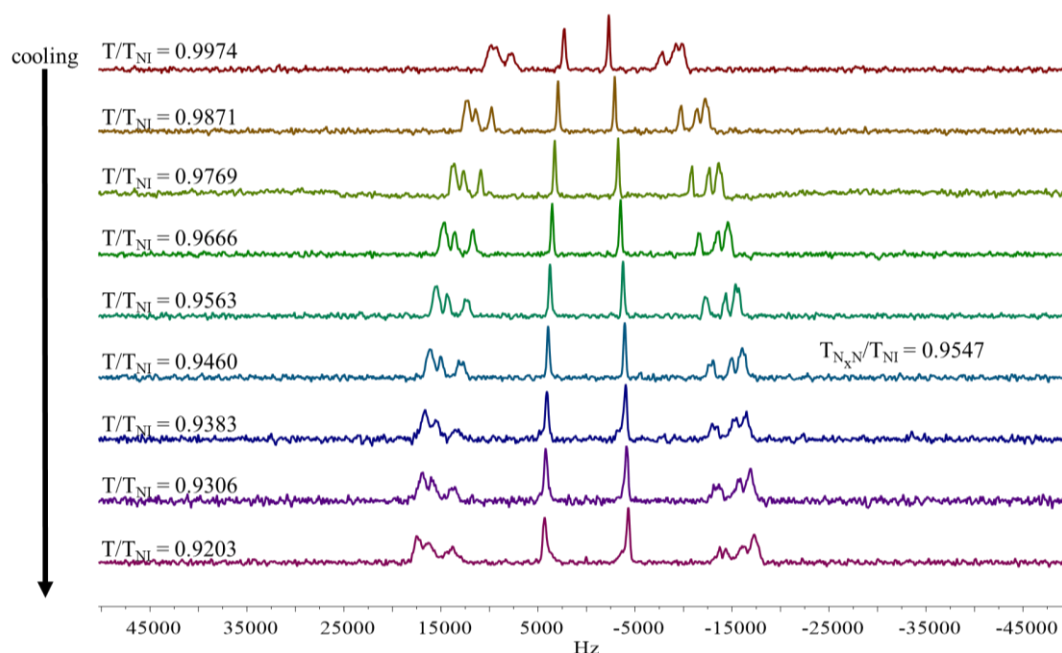


Figure 3.15. ^2H NMR spectra of decane- d_{22} in CB-C9-CB at decreasing temperatures (from top to bottom) The N_x -N transition is noted and occurs at a reduced temperature of 0.9547.

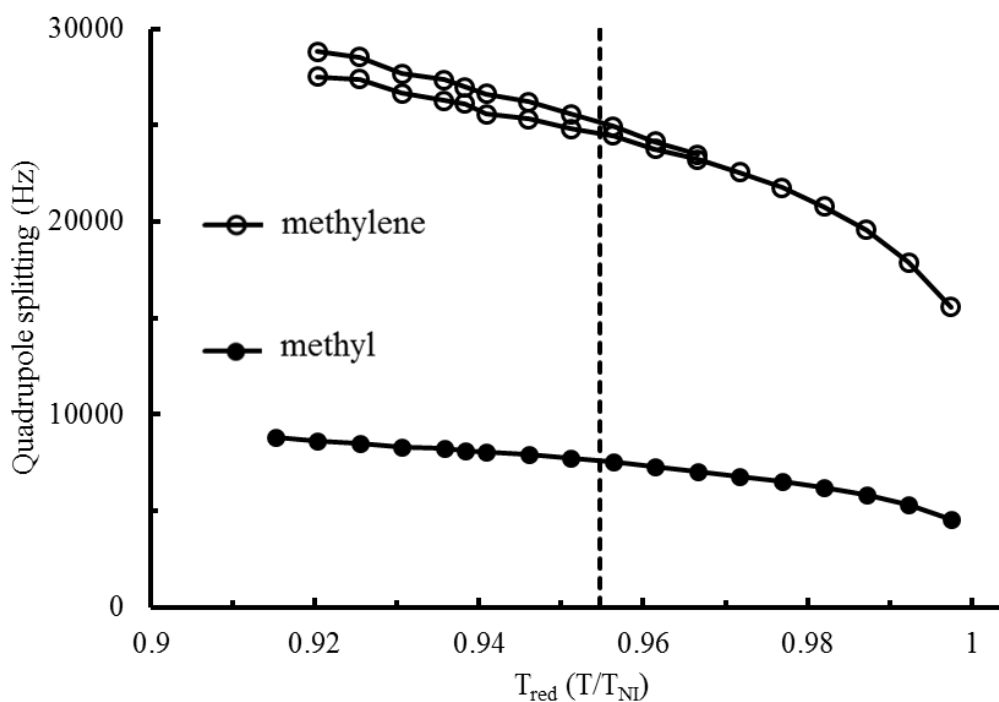


Figure 3.16. The temperature dependence (in reduced temperature) of the quadrupole splitting of the methyl and methylene group of decane- d_{22} in CB-C9-CB with the N to N_x phase transition shown as dotted line.

When the spacer length of the CB-C_n-CB dimer is 7, the doubling of the α -CD₂ peaks upon entrance into the N_x phase is even more pronounced. ²H spectra for selected temperatures and a plot of the quadrupole splitting of the methyl and α -methylene of decane-d₂₂ against reduced temperature for CB-C7-CB are shown in Figures 3.17 and 3.18, respectively.

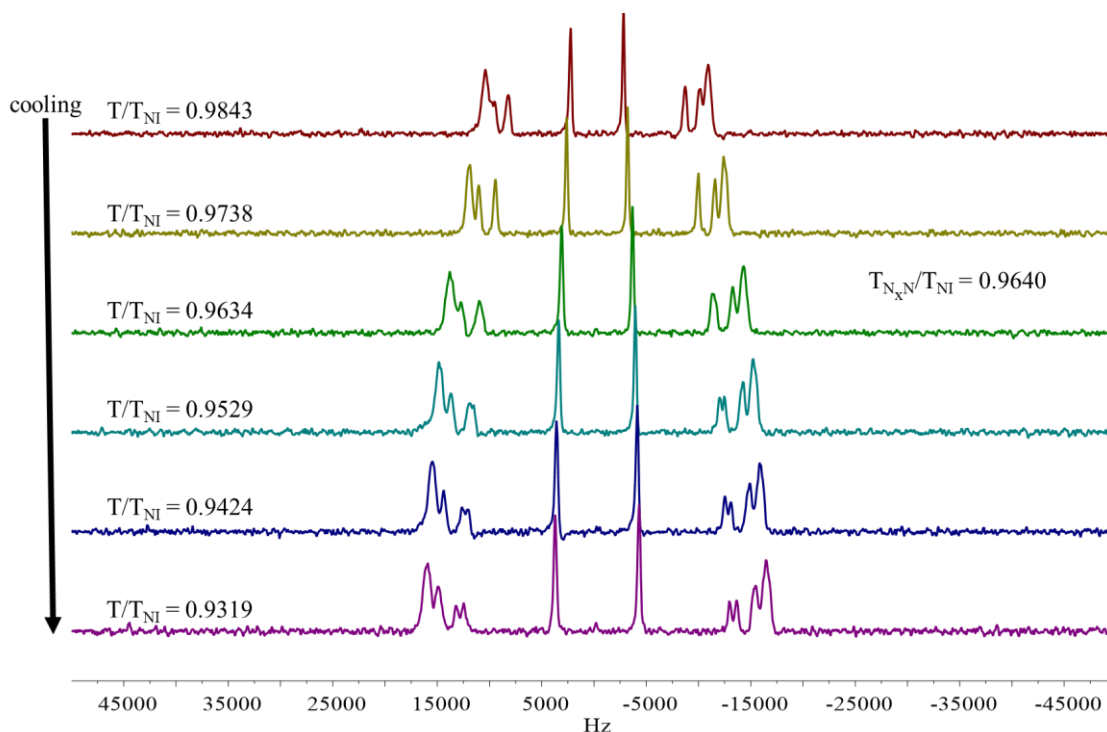


Figure 3.17. ²H NMR spectra of decane-d₂₂ in CB-C7-CB at decreasing temperatures (from top to bottom) The N_x-N transition is noted and occurs at a reduced temperature of 0.9640.

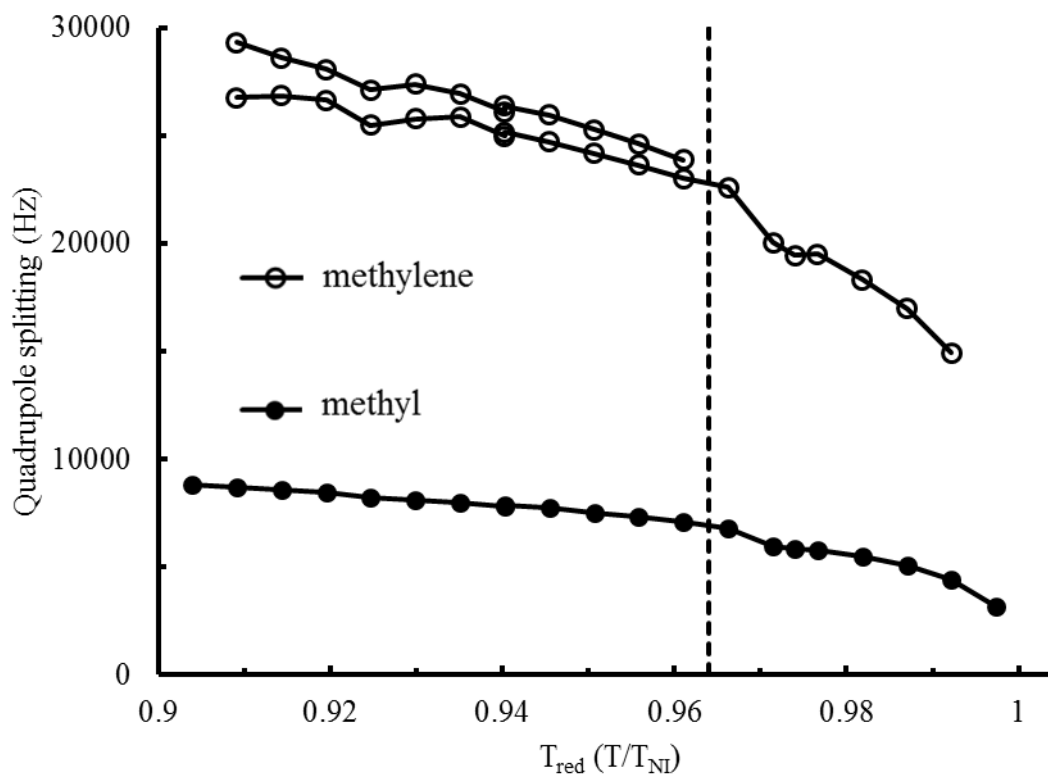


Figure 3.18. The temperature dependence (in reduced temperature) of the quadrupole splitting of the methyl and methylene group of decane- d_{22} in CB-C7-CB with the N to N_x phase transition shown as dotted line.

The peak doubling of the α -CD₂ upon transition into the N_x phase suggests the presence of chiral asymmetry. However, the presence of chirality does not confirm nor refute the twist-bend deformation of the director. Hoffman et al. suggest an alternate structure based on “orientational frustration” of the molecules due to their nonlinear conformations. The mesogenic units are unable to simultaneously align parallel to each other as demonstrated in Figure 3.19.



Figure 3.19. A possible arrangement of mesogenic units within each chiral domain for odd cyanobiphenyl dimers. From ref 72.

3.3.3 Comparison with chiral nematics

In order to explore the notion of orientational frustration further, we compare the ^2H spectra of decane- d_{22} dissolved in CB-C7-CB with that of decane- d_{22} dissolved in a well-known chiral nematic (cholesteric) liquid crystal, cholesteryl nonanoate (CN). For the cholesteric phase of CN, the $\alpha\text{-CD}_2$ doubling does not occur (Figure 3.20). This result is in line with a similar experiment that shows no doubling for nonanoic acid- αd_2 (a prochiral molecule) dissolved in CN.⁷⁷ The cholesteric phase is identified by an abrupt change in the quadrupole splitting upon heating from the smectic phase.

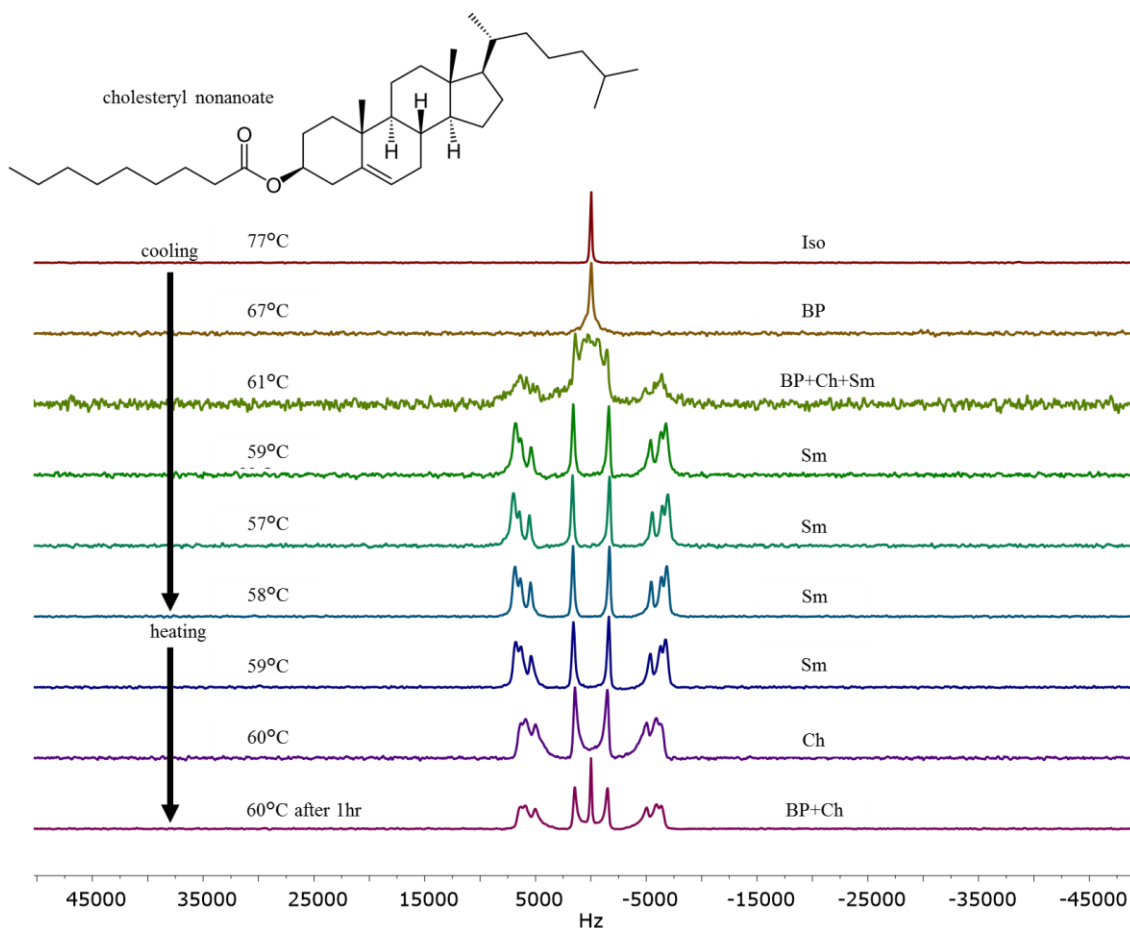


Figure 3.20. ^2H spectra of 2 wt% decane- d_{22} dissolved in cholesteryl nonanoate (CN) cooled into the smectic phase and heated to access the cholesteric phase (spectrum labeled “Ch”) as in ref 77.

The difference in the spectra of decane- d_{22} dissolved in the chiral nematic phase of CN and the N_X phase of CB-C7-CB indicates that the nature of these two phases are different. Luz et al.⁷⁷ report that the cholesteric phase consists of two domains: uniformly oriented with the helix axis parallel to the magnetic field (leading to a smaller observed quadrupolar splitting) and randomly oriented domains. The chirality of the cholesteric phase of CN arises because CN is a chiral molecule; the chirality in CB-C7-CB, an achiral molecule, arises due to orientational frustration (Figure 3.19).

3.3.4 Demonstration of the odd-even effect of cyanobiphenyl dimers

The odd-even effect of cyanobiphenyl dimers is evident in the spectra of probe decane molecules dissolved in odd and even dimers. In Figure 3.21 the α -CD₂ splitting of decane-d₂₂ dissolved in the odd dimers is significantly lower than that of an even dimer, CB-C10-CB. Even dimers do not experience orientational frustration and thus obtain significantly higher order parameters as inferred by the large methylene splitting of CB-C10-CB and do not experience the lower temperature chiral N_X phase. Additionally, CB-C10-CB experiences higher orientational order than the monomer 5-CB meaning that the alkyl spacer is short enough that the cyanobiphenyl dimers remained coupled to one another and acts like a single rigid molecule. For cyanobiphenyl dimers with odd alkyl spacer lengths, the orientational order increases as the alkyl chain gets longer because orientation frustration decreases as the alkyl spacer gets longer. At very long alkyl spacer lengths these effects should disappear, but this “extreme” alkyl spacer length cannot be determined by the current measurements.

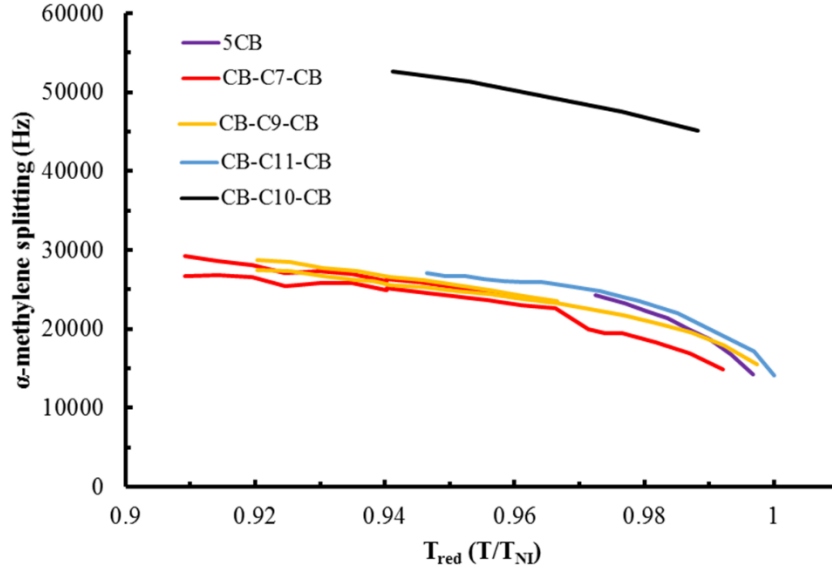


Figure 3.21. The temperature dependence (in reduced temperature) of the quadrupole splitting of the α -methylene group of decane- d_{22} in all samples including the monomer, 5-CB and the even dimer, CB-C10-CB.

3.3.5 Core order parameters

The core order parameter of a liquid crystalline phase is an important parameter in determining the structure and molecular ordering. The order parameter describes the degree of order of the phase and is related to the ^2H quadrupolar splitting (Equation 3.2). The order parameter of a nematic phase can be determined by measuring the quadrupolar splitting of a selectively deuterated molecule. In the report by Hoffman et al.⁷² CB-C9-CB is selectively deuterated in the $\alpha\text{-CD}_2$ position. The order parameter $S_{\alpha\text{-CD}}$ is determined from the quadrupolar splitting of the deuterons (Equation 3.3).

$$\Delta\nu = \frac{3}{2} |q_{\text{CD}} S_{\alpha\text{-CD}}| \quad (3.3)$$

where $S_{\alpha\text{-CD}} = \langle P_2(\hat{\mathbf{e}}_{\alpha\text{-CD}} \cdot \hat{\mathbf{H}}) \rangle$, $\hat{\mathbf{e}}_{\alpha\text{-CD}}$ denotes the orientation of the C—D bond, $\hat{\mathbf{H}}$ denotes the orientation of the magnetic field, P_2 is the second Legendre polynomial and the brackets denote an ensemble time average. For the N phase of CB-C9-CB- αd_2 , $S_{\alpha\text{-CD}} = -0.19$ at

temperature $T = 106^\circ\text{C}$, $\Delta\nu = 48\text{kHz}$, and $q_{CD} = 168\text{kHz}$. The core order parameter is

$S_{core} = \langle P_2(\hat{\mathbf{e}}_p \cdot \hat{\mathbf{H}}) \rangle$ where $\hat{\mathbf{e}}_p$ is the orientation of the biphenyl para axis. S_{core} is related to $S_{\alpha-CD}$ and is found using Equation 3.4 to be 0.57 assuming a tetrahedral angle between the para axis and C—D bond.

$$S_{\alpha-CD} = S_{core} P_2(\hat{\mathbf{e}}_p \cdot \hat{\mathbf{e}}_{\alpha-CD})$$

$$S_{core} = \frac{2S_{\alpha-CD}}{(3\cos^2(109.5^\circ) - 1)(\hat{\mathbf{e}}_p \cdot \hat{\mathbf{e}}_{\alpha-CD})} = 0.57 \quad (3.4)$$

Values of S_{core} shows only a slight increase upon cooling in the N_X phase and saturates at a value of 0.6.

3.3.6 Direct determination of S_{core} using the chemical shift anisotropy of ^{13}C

Although it is possible to obtain the core order parameter using the $\alpha\text{-CD}_2$ quadrupolar splitting as described in the previous section, it is not a direct measure of the core order parameter. The assumption of a constant tetrahedral angle between the C—D bonds and the biphenyl para axis has to be made. To the best of our knowledge, there has not been a direct measure of the core order parameter for this class of odd-cyanobiphenyl dimers. One way to directly measure S_{core} is using ^{13}C NMR to measure the chemical shift of the cyano carbon as a function of temperature.

The chemical shift (δ) is described by a tensor; a 3 x 3 matrix of real numbers as described in Section 1.4.3 and the isotropic chemical shift is the average of the three principal chemical shift values (Equation 3.5).

$$\delta_j^{iso} = \delta_{xx}^j + \delta_{yy}^j + \delta_{zz}^j \quad (3.5)$$

Chemical shift anisotropy (CSA) quantifies deviation from isotropy. This occurs when some orientations are preferred like in anisotropic liquids and solids. Therefore, if

molecular motion changes from isotropic to anisotropic, the NMR peak frequencies will change. The chemical shift is no longer an average over all orientations, but biased orientations are sampled along \mathbf{B}_0 .³

The observed chemical shift is the sum of the isotropic chemical shift and the anisotropic chemical shift. In order to obtain the core order parameter, the temperature dependence of the chemical shift of CN was measured. The observed chemical shift ($\delta_{\text{CN}}^{\text{obs}}$) at each temperature and the isotropic chemical shift ($\delta_{\text{CN}}^{\text{iso}}$) were used to calculate the anisotropic chemical shift ($\delta_{\text{CN}}^{\text{aniso}}$) via Equation 3.7.

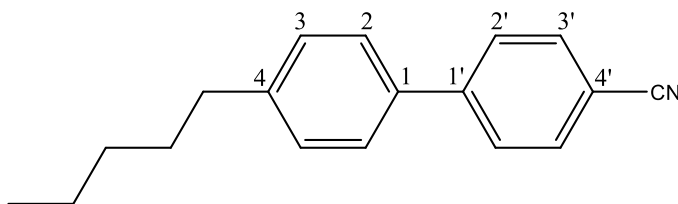
$$\delta_{\text{CN}}^{\text{aniso}} = \delta_{\text{CN}}^{\text{obs}} - \delta_{\text{CN}}^{\text{iso}} \quad (3.7)$$

Guo and Fung used two-dimension ^{13}C NMR for several series of liquid crystals to derive an equation to calculate order parameters directly from $\delta_{\text{CN}}^{\text{aniso}}$.⁷⁸ Equation 3.8 is used to calculate the order parameter of CN (S_{CN}). Values for a and b are taken from values determined by Guo and Fung for monomers nCB with $n = 5, 6, 7$ and 8 and are shown in Table 3.1.

$$S_{\text{CN}} \approx \frac{\delta_{\text{CN}}^{\text{aniso}} - b}{a} \quad (3.8)$$

where $a = \frac{2\Delta\sigma}{3}$, $\Delta\sigma = [\sigma_{zz} - \frac{1}{2}(\sigma_{xx} + \sigma_{yy})]$, and b is an empirical constant.

Table 3.1. Calculated values of a and b in ppm for each ^{13}C nucleus in the phenyl rings and CN group of 5-CB. ⁷⁸



^{13}C nucleus	1	2	3	4	1'	2'	3'	4'	CN
a	83.3	31.7	30.5	82.0	97.7	40.8	46.9	92.7	-188.7
b	9.2	4.5	3.2	7.3	5.3	5.1	5.0	3.9	-12.7

3.3.7 ^{13}C NMR of cyanobiphenyl dimers

^{13}C spectra of CB-C11-CB at decreasing temperature with ^1H decoupling is shown in Figure 3.22. In the oriented phase, the chemical shift anisotropy (CSA) of the cyano (CN) group causes it to overlap with the chemical shift of the aliphatic carbons. In order to identify the CN group, a ^1H coupled experiment was performed (Figure 3.23). The CN peak does not have any observable dipolar coupling in the ^1H coupled experiment, so its chemical shift can be distinguished from the aliphatic peaks.

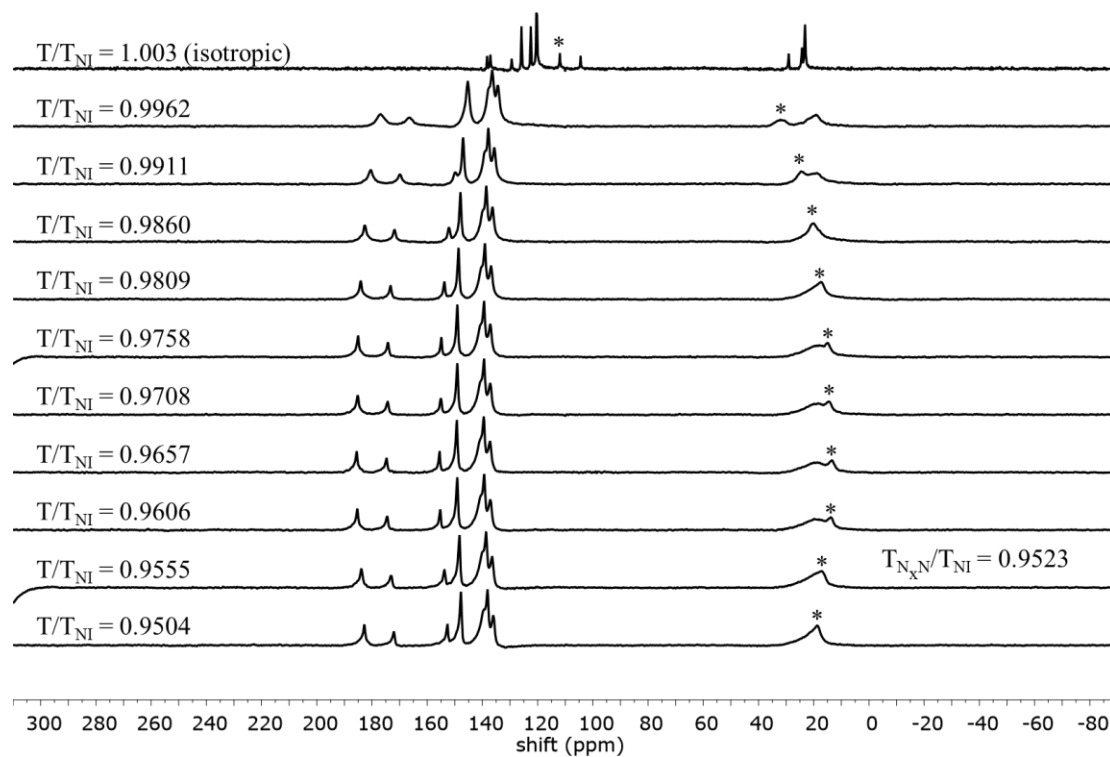


Figure 3.22. ^{13}C spectra of CB-C11-CB at decreasing temperature with ^1H decoupling. The first spectrum is in the isotropic phase. The cyano group (*) is identified.

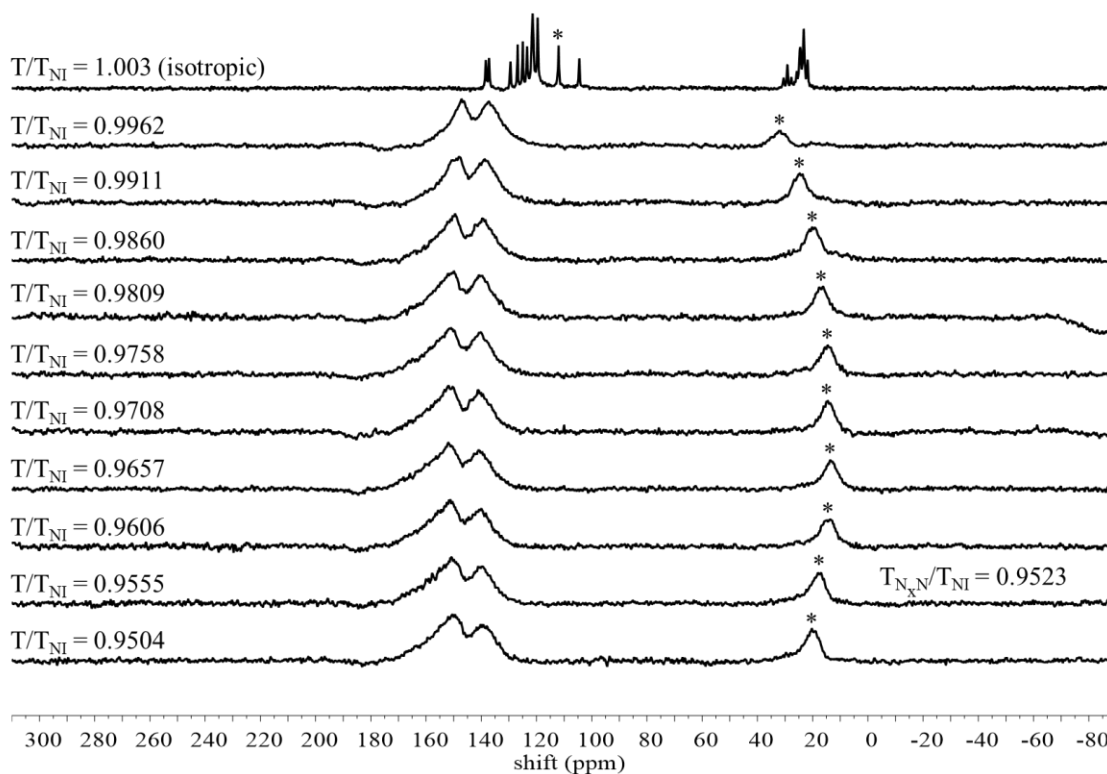


Figure 3.23. ^{13}C spectra of CB-C11-CB at decreasing temperature without ^1H decoupling. The first spectrum is in the isotropic phase. The cyano group (*) is identified.

Values of S_{CN} were calculated with Equation 3.8 and plotted against reduced temperature (Figure 3.24). The order parameter increases steadily in the nematic, but begins to decrease slightly as it approaches the N_x phase (except for CB-C7-CB where the order parameter increases slightly) and plateaus at it supercools.

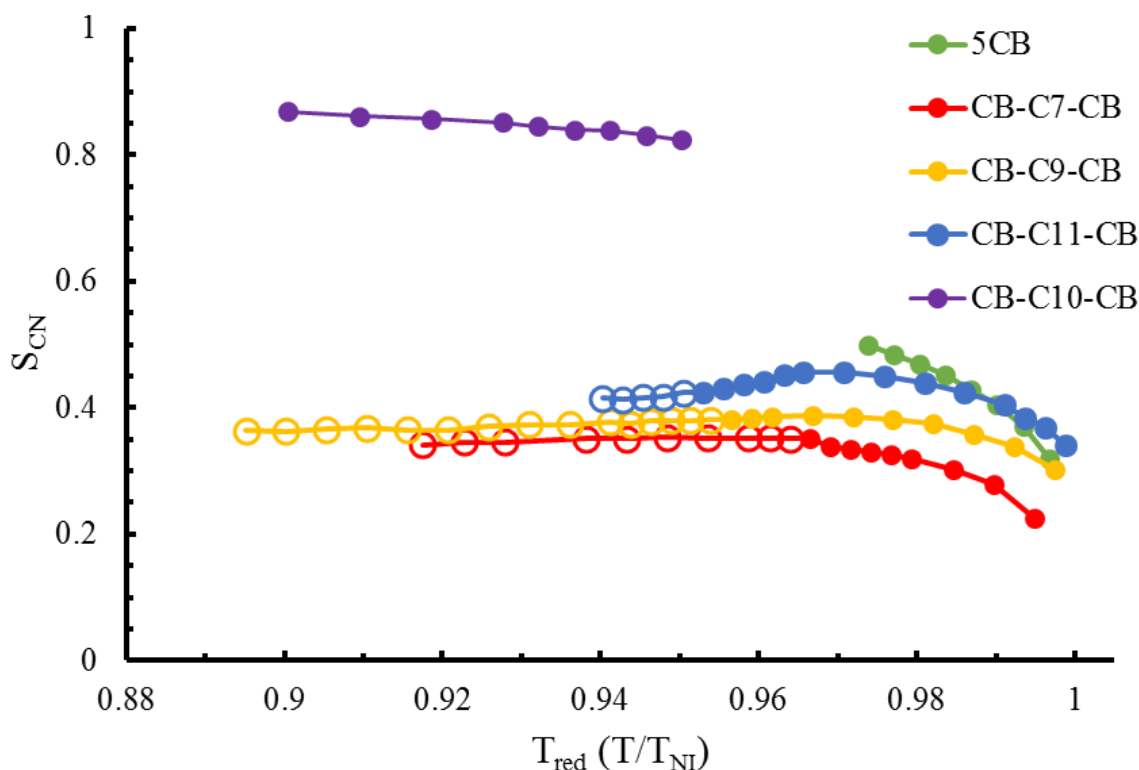


Figure 3.24. The temperature dependence (in reduced temperature) of the order parameter of CN in CB-C11-CB, CB-C9-CB, CB-C7-CB, and the monomer 5-CB. Open circles indicate transition into the N_x phase determined by DSC experiment.⁷⁶

The cyano order parameter, S_{CN} , plotted in Figure 3.24 is equal to the core order parameter, S_{core} . Hoffman et al.⁷² calculated S_{core} to be ~ 0.57 for the N phase of CB-C9-CB and ~ 0.6 for the N_x phase, however, in our measurements S_{core} is much lower and plateaus at ~ 0.37 in the supercooled N_x phase. The trend, however, is similar where the ordering remains low into the N_x phase which confirms the proposed structure of chiral domains with orientational frustration (Figure 3.19). Within the series of odd dimers, the dimers with larger alkyl spacer have larger core order parameters approached the order parameter of the monomer, 5-CB. The even dimer, CB-C10-CB shows extremely high ordering ($S_{core} \sim 0.85$). Due to this high degree of ordering, the direct dipolar coupling between molecules begins to overwhelm the quadrupolar coupling and the CN resonance is very broad (Figure 3.25)

compared to any of the odd cyanobiphenyl dimers. To obtain a better measurement of S_{core} , we used the 4' resonance (phenyl ring carbon adjacent to CN) and the corresponding a and b values in Table 3.1. This is a valid comparison and in the Guo and Fung report they show that order parameters for all phenyl carbons and the cyano group collapse onto one line using their calculated values for a and b .

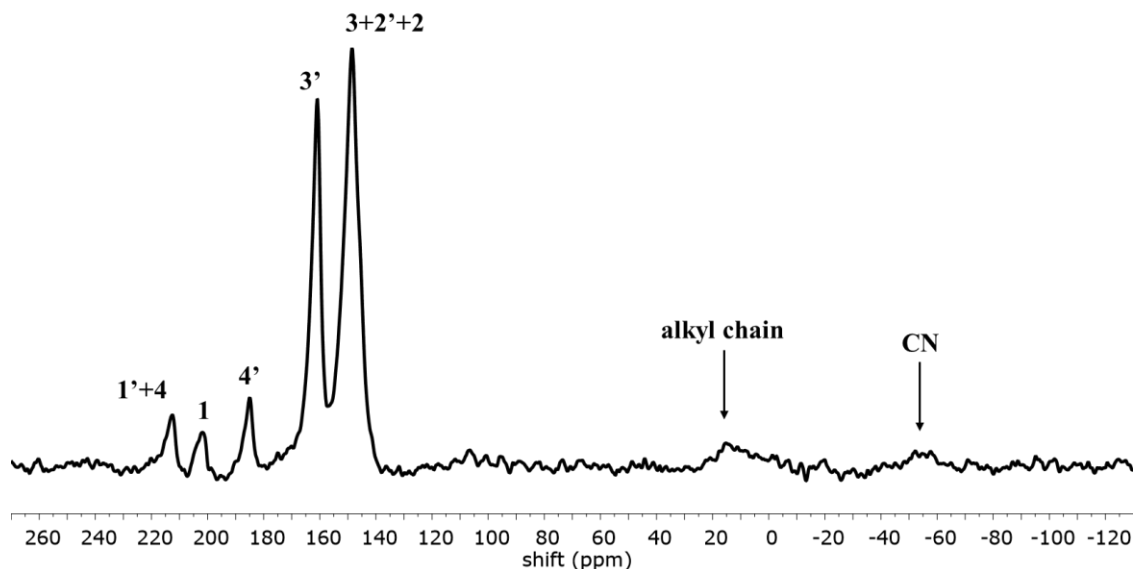


Figure 3.25. ^{13}C NMR of CB-C10-CB in the nematic phase. Peaks identified using ref 79.

3.4 Conclusions

In this chapter, we have demonstrated the first direct measurement of the core order parameter of odd cyanobiphenyl dimers exhibited an additional low temperature nematic phase (N_X) by exploiting the CSA using ^{13}C NMR. Recently, a simplified model was used to explain the experimental results on odd-cyanobiphenyl dimers and propose an alternate structure of the N_X phase.⁸⁰ The model consists of two uniaxial mesogenic cores separated by fixed-length spacers and allows for two conformations only, which are nonplanar and of opposite handedness. They find three distinct phases using a mean-field approximation: one isotropic, one uniaxially apolar nematic, and one transversely polar and twisted nematic.

Efforts are underway by Vanakaras and Photinos to fit the ^2H NMR alkane data in cyanobiphenyl dimers (tables of data included as Appendix A) and initial results suggest excellent fits of their model to the data.

CHAPTER 4: LOCAL DYNAMICS OF BOTTLEBRUSH MACROMOLECULES VIA ^2H NMR

4.1 Introduction

Bottlebrush macromolecules (BBMs) constitute a group of graft macromolecules having long and densely grafted side chains and exhibiting gel-like properties in the neat material.⁸¹ These shape-persistent macromolecules have been targeted as materials for applications ranging from mechanosensors^{82–84} and photonics^{85–87} to bio-inspired lubricants⁸⁸ and super-soft elastomers.^{89,90} The side chains in BBMs act as a pseudo-solvent that, unlike in hydrogels, are covalently attached to the polymer backbone. The resulting intra-macromolecular steric repulsion between the crowded graft side chains impacts the persistence length of the BBM backbone by restricting its ability to explore random-coil configurations on spatial scales characteristic of linear, non-grafted polymers.⁸¹ In turn, the density of intermolecular entanglements in condensed neat phases of BBMs is reduced and as a result, networks comprised of covalently linked BBMs are anticipated to have very low moduli (~kPa) and are referred to as super-soft elastomers⁹¹ or very soft networks.⁹⁰

The grafting density and side chain length can be tuned in BBMs in order to target applications requiring specific physical properties. In an effort to quantify the effect of certain tunable features on the internal mobility of BBMs, poly((2-(2-bromopropionyloxy)ethyl methacrylate-*stat*-methyl methacrylate-g-butyl acrylate) (poly((BPEM-*stat*-MMA)-g-PBA)) was previously studied using proton NMR (^1H NMR) relaxation dynamics.⁹² Pietrasik and coworkers measured the ^1H spin-spin relaxation time

(T_2) and found that the proton T_2 of the BBM backbone decreased with increasing side chain length and grafting density. Their observations indicated that molecular congestion on the interior of BBMs resulted in a significant decrease in molecular motion along the backbone. The T_2 relaxation times of protons on the PBA side chains showed a more complicated response.⁹²

Herein, we reexamine molecular bottlebrushes dynamics using deuterium NMR (^2H NMR) to monitor the local dynamics within the backbone and side chains of BBMs. Unlike ^1H relaxation, which is dominated by the dipole-dipole relaxation mechanisms among multiple protons at variable dynamical distances and chemical shift anisotropy relaxation mechanisms at high magnetic fields, ^2H relaxation is dominated by the well-defined quadrupolar interaction, i.e. intra-carbon-deuterium bond interaction that is directly related to C—D bond reorientations.³ For the purpose of this study, we designed BBMs with a deuterium label covalently embedded in the center of the backbone chain (Figure 4.1).

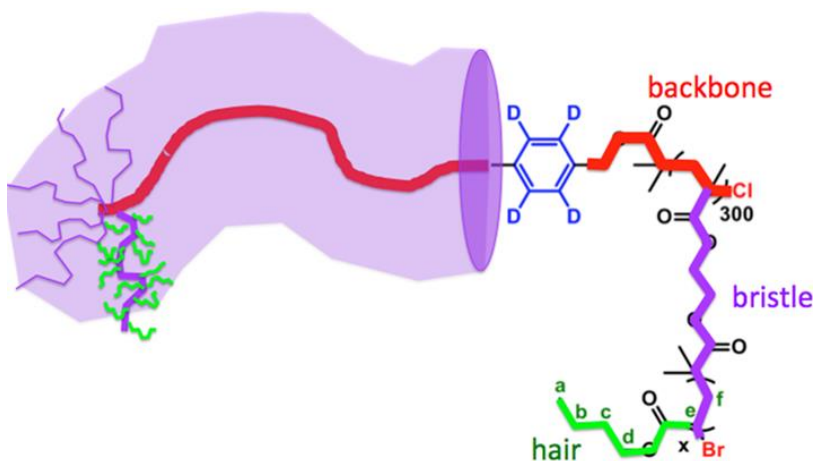


Figure 4.1. Schematic diagram of bottlebrush macromolecule (BBM) showing label in backbone, grafted “bristles” and “hair” on each of the bristles.

BBMs can be synthesized via three methods: (i) ‘grafting through’,⁹³ (ii) ‘grafting onto’,⁹⁴ and (iii) ‘grafting from’^{81,95–97} strategies. The latter method is mainly performed via

controlled radical polymerization (CRP) methods, in particular atom transfer radical polymerization (ATRP).^{98–100} The ‘grafting from’ via ATRP allows for a good control over the grafting density and degree of polymerization (DP) of the side chains and backbone. In addition, initiators utilized by ATRP can be easily obtained by simple organic reactions including esterification/amidation of hydroxyl/amine functionalities.

The structural simplicity of ATRP initiating groups enables access to more complex functional ATRP initiators, which can be utilized to tune the topology and/or properties of molecular bottlebrushes.⁸⁴ In studies by Matyjaszewski, Sheiko, and coworkers, an ATRP diinitiator consisting of a disulfide (S-S) bond was used to incorporate a weak bond in a bottlebrush, thus obtaining a molecular tensile machine.⁸² The mechanical tension intrinsically generated by the brush enabled detailed kinetic studies of a selective cleavage, of S-S bond which could be controlled by tuning the length of the side chains or/and the properties of the used substrate.^{82,83} A similar approach was applied by Burdyńska and Matyjaszewski to design an ATRP di-initiator with a labeled quinone-d₄ ring and employ it in formation of ²H labeled BBM for the bottlebrush dynamics studies.

4.2 Experimental Methods

A deuterated ATRP diinitiator (Br-d₄-Br, Figure 4.2b) was employed to generate labeled molecular bottlebrushes (BBM-d₄) for NMR dynamical studies. The synthetic approach for the preparation of BBM-d₄ involved two steps: the formation of ATRP diinitiator with a deuterium label (Br-d₄-Br) and the incorporation of Br-d₄-Br into the structure of BBM (Figure 4.2b).

In order to embed a deuterium label into Br-d₄-Br, several chemical modifications were performed on the commercially available deuterated terephthalic acid (TPA-d₄, Figure

4.2a). The general methodology involved: an esterification of TPA- d_4 to form its dimethyl ester (DMTP- d_4), a reduction of DMTP- d_4 to the corresponding diol (PDM- d_4), and an esterification of PDM- d_4 to form the ATRP diinitiator (Br- d_4 -Br) (Figure 4.2a).

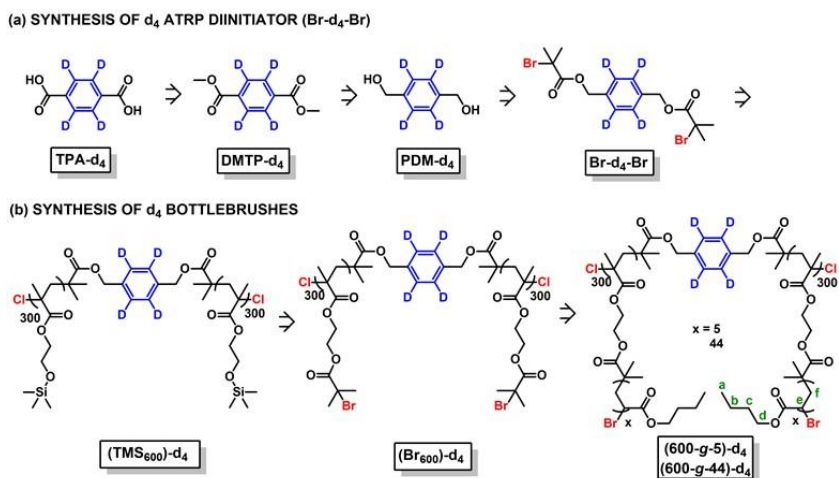


Figure 4.2 The synthetic pathway for the preparation of **a.** ATRP diinitiator- d_4 (Br- d_4 -Br) and **b.** labeled BBMs and PnBA side chains ((600-g-5/44)- d_4). Figure prepared by Joanna Burdyńska.

Figure 4.2b shows the synthetic methodology applied in the preparation of deuterated bottlebrushes. BBMs were prepared via the “grafting-from” approach under normal ATRP conditions.

4.2.2 NMR Methods

The first set of data includes relaxation data from dilute brush solutions. All of the 1D spectra of brush solutions were taken on a Bruker B600 spectrometer operating at 92.12 MHz (^2H frequency) using a liquid state cryoQNP probe with Z-gradients. The samples were made by dissolving in dichloromethane (DCM) and acquired in nonspinning sealed 5mm tubes at 298K.

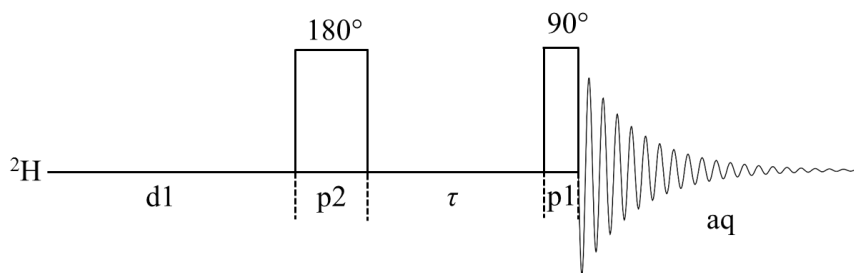


Figure 4.3. Inversion recovery pulse sequence. Values of τ are varied for measuring the spin-lattice relaxation time, T_1 .

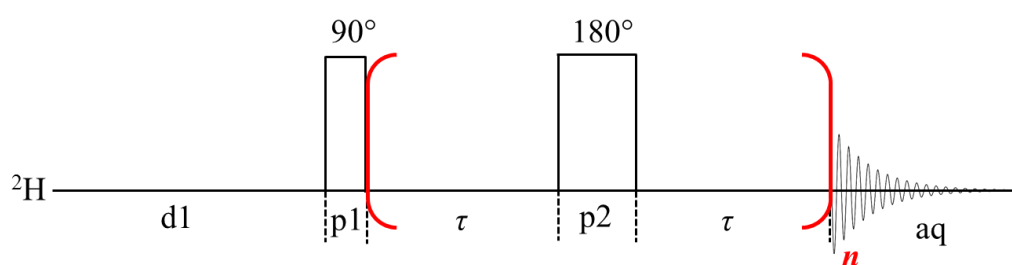


Figure 4.4. Car-Purcel-Meiboom-Gill (CPMG) pulse sequence. Values of n are varied for measuring the spin-spin relaxation time, T_2 .

Before the ^2H acquisition, each sample was shimmed using the ^1H NMR free induction decay (FID). For 1D experiments, a 90° pulse width of $139\ \mu\text{s}$ was used with a recycle delay of 1 s. T_1 values were measured using an inversion recovery pulse sequence (Figure 4.3) and T_2 values were measured using a Car-Purcel-Meiboom-Gill (CPMG) pulse sequence (Figure 4.4), both included in the Bruker software. Peak intensities were recorded at different delay times. The peak intensities were fit to exponential functions (Equations 4.1 and 4.2, where M is the measured peak intensity at time t and M_0 is the maximum peak intensity at $t = 0$) in order to extract the relaxation times.³

$$\frac{M}{M_0} = 1 - 2e^{-t/T_1} \quad (4.1)$$

$$\frac{M}{M_0} = e^{-t/T_2} \quad (4.2)$$

The second set of data includes spectra of neat brush samples taken using a high-powered probe tuned to the ^2H Larmor frequency, 55.3 MHz, with a quadecho pulse sequence; experimental details given in Figure 4.5.

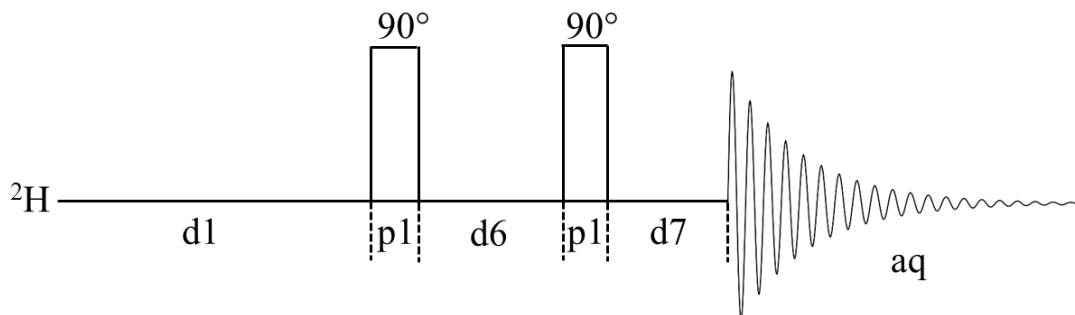


Figure 4.5. ^2H NMR Quad echo pulse sequence where 90° pulses ($p1$ at power level 6 dB) were calibrated to $5.3 \mu\text{s}$, $d1$ (recycle time) is 500 ms, $d6$ is $20 \mu\text{s}$ and $d7$ is $9 \mu\text{s}$.

4.3 Results and Discussion

4.3.1 Solution Dynamics in Bottlebrush Backbone

Our aim was to understand the local bottlebrush backbone dynamics by measuring NMR relaxation times (correlation times) as a function of BBM architecture. To that end, we have inserted a well-defined ^2H label into (Br600)- d_4 macroinitiator and measured the relaxation behavior with, and without grafted n-butyl acrylate side chains ((600-g-5)- d_4 and (600-g-44)- d_4) (Figure 4.2b). Specifically labeling BBMs with deuterium enables one to probe the dynamics of local motion at the site of the C—D bond. NMR relaxation times T_1 and T_2 can be related to physically-relevant correlation times, τ_c , the time it takes the C—D bond to lose its correlation with its original orientation. The relation between T_i and τ_c is given by Equations 4.3 and 4.4,^{4,101}

$$\frac{1}{T_1} = \frac{3\pi^2}{10} \left(\frac{e^2 q Q}{h} \right)^2 \left[\frac{\tau_c}{1 + \omega^2 \tau_c^2} + \frac{4\tau_c}{1 + 4\omega^2 \tau_c^2} \right] \quad (4.3)$$

$$\frac{1}{T_2} = \frac{3\pi^2}{20} \left(\frac{e^2 q Q}{h} \right)^2 \left[3\tau_c + \frac{5\tau_c}{1 + \omega^2 \tau_c^2} + \frac{2\tau_c}{1 + 4\omega^2 \tau_c^2} \right], \quad (4.4)$$

which in the fast motion limit ($\omega^2 \tau_c^2 \ll 1$), becomes

$$\frac{1}{T_1} = \frac{1}{T_2} = \frac{3\pi^2}{2} \left(\frac{e^2 q Q}{h} \right)^2 \tau_c \quad (4.5)$$

The particular labeled moiety, a quinone ring in the BBM backbone, was chosen so that all ^2H nuclei were magnetically equivalent and chemically shifted from the aliphatic hydrogens in the brush. The latter could interfere if natural abundance deuterium (0.015%) resonances from the side chains begin to dominate the spectrum. The ^2H NMR spectrum of the bottlebrush backbone (BBB) in Figure 4.6 shows that the aromatic ^2H label has a chemical shift of 7.41 ppm, outside of the aliphatic region (1-4 ppm), and is sufficiently removed from the dichloromethane (DCM) solvent resonance (5.33 ppm). Initially our goal was to compare the backbone dynamics with and without grafted side chains. To this end we measured the relaxation times T_1 and T_2 for different concentrations of the labeled BBB in DCM. We roughly estimate the overlap concentration as $\frac{1}{\sqrt{N}}$ of the BBB to be 0.04 g/mL and acquired relaxation measurements on three samples: 0.01 g/mL ($c < c^*$), 0.04 g/mL ($c \sim c^*$), and 0.09 g/mL ($c > c^*$). For each concentration, T_1 and T_2 were determined (Table 4.1) by exponential fits to Equations 4.1 and 4.2 (Figure 4.7). Within the experimental error, $T_1 = T_2$ in each sample implying that the fast motional limit applies, independent of BBB concentration. For the range of concentrations measured, the relaxation times are not particularly dependent on concentration suggesting that the relaxation is primarily caused by

intra-backbone motions (rotations about and librations of the *para* axis of the labeled aromatic ring in BBB and not global reorientational motion of the whole polymer chain.¹

Table 4.1. Relaxation data for decreasing concentrations of BBBs (Br₆₀₀)-d₄.

	c (g/mL)	T₁ (ms)	T₂ (ms)
c > c*	0.089	43.7	40.0
c ~ c*	0.040	35.6	30.6
c < c*	0.014	41.0	23.5

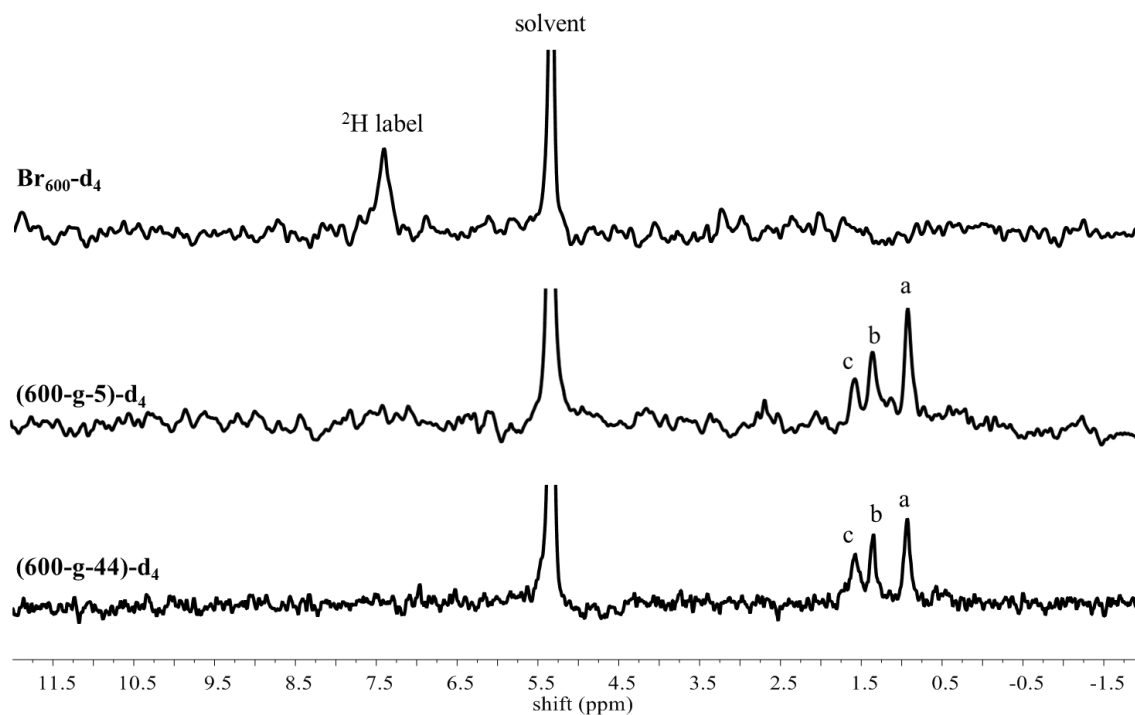


Figure 4.6. ²H 1D NMR spectra of (Br₆₀₀)-d₄ (0.09g/mL in DCM), (600-g-5)-d₄ (10 wt% in DCM), and (600-g-44)-d₄ (12 wt% in DCM).

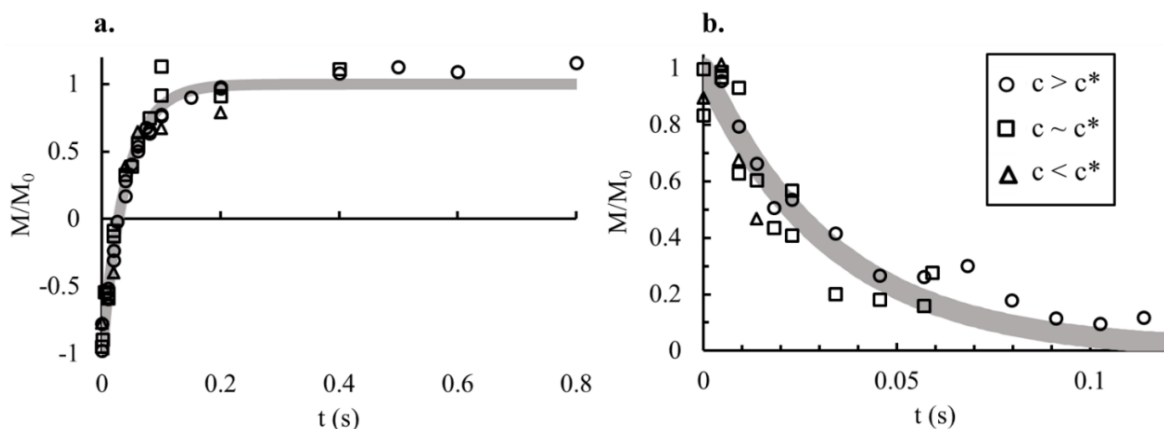


Figure 4.7. Experimental data for determination of T_1 (a) and T_2 (b) for three concentrations of BBB. Shaded line represents the estimated error in the exponential fit.

4.3.2 Solution Dynamics in Bottlebrush Macromolecules

The NMR spectra and relaxation results of the simple bottle brush polymer backbone (BBB) (Br_{600})- d_4 change dramatically when the polymer backbone is grafted to make the BBM (600-*g*-5)- d_4 (10 wt% in DCM), and in the BBM (600-*g*-44)- d_4 (12 wt% in DCM). For starters, the label resonance at 7.4 ppm in the BBB is not observable in the BBM spectra (Figure 4.6). This is not due to insufficient label: the 0.015% natural abundance methyl signal in BBM (600-*g*-5)- d_4 is calculated to be one third of the intensity anticipated for the specifically labeled deuterons in the backbone. The aromatic label's covalent linkage into the backbone insures that it reflects local reorientation of the backbone contour. But if the backbone correlation time becomes too long, i.e., if T_2 decreases and falls below the fast motion limit and loses its equivalence to T_1 (T_1 goes through a minimum and begins to increase), the backbone resonance linewidth increases. For very slow dynamics (long correlation times), the linewidth of the resonance from the backbone label becomes very broad and cannot be detected with conventional high resolution NMR. Over the entire range of graft densities and graft side chain lengths we could access with the ATRP chemistry—a

degree of polymerization of the PBA unit (DP_{sc}) ranging from $DP_{sc} \sim 44$ to $DP_{sc} \sim 5$ —the label resonance was too broad to measure. Note that for short graft lengths (e.g., $DP_{sc} \sim 5$), the DP_{sc} is computed by the monomer conversion (x_{nBA}) (described in the synthetic section), which gives *on average* $DP_{sc} \sim 5$.

In order to facilitate the discussion, we describe the bottlebrush structure as a backbone chain (stem) with grafted side chains (“bristles”). As shown in Figure 4.1, each bristle is comprised of a defined number of R (= PBA) units, and each PBA unit has a $CH_3CH_2CH_2CH_2-O-CO-$ appendage, i.e., a butyl-ester “hair” emanates from each segment of the bristle. In the BBM samples, the mobility within the bristle is sufficient to detect the natural abundance 2H NMR resonances of the butyl-ester sheath on the bristle exterior. The PBA units in the graft sidechains exhibit resolved, natural abundance resonances in the bottlebrush (600-g-5)- d_4 and (600-g-44)- d_4 samples (Figure 4.6). The differentiated natural abundance 2H resonances of the butyl-ester hairs on each bristle graft are labeled a-f in Figure 4.2b. The aliphatic units of the hair that are furthest from the grafted bristle’s contour are the only peaks detected in the 2H NMR spectra of the BBM. This suggests that the side chain dynamics within the dense grafted bristle environment surrounding the backbone stem are too slow (T_2 is too short) to detect natural abundance resonances for all of the protonated sites; only the positions a, b, and c at the extremity of the hair on each bristle have sufficient mobility to give nicely resolved resonances. For these positions, the relaxation measurements fall within the fast motion limit ($T_1 = T_2$) within experimental error.

The relaxation data in Table 4.2 reveals that as we move along the butyl ester hairs from the exterior methyl groups to the ester linkage to the bristle’s contour, the dynamics slow down significantly. The resonance for the “d” methylene is already too broad to show

up in the spectrum. These findings support a picture of bottlebrush intra-macromolecular organization wherein significant steric repulsion among the crowded grafts result in dynamics too slow for the bristles and certainly for the constrained backbone to enable high resolution spectra.

Table 4.2. T_1 and T_2 data and calculated correlation times for (600-g-44)-d₄.

	T_1 (ms)	$\tau_{c,1}$ (ps)	T_2 (ms)	$\tau_{c,2}$ (ps)
a	257	7.68	100	19.7
b	130	15.2	83.8	23.6
c	53.7	36.8	42.2	46.8

4.3.3 Bottlebrush Dynamics Inferred from NMR Linewidths

In an attempt to identify the label peak, we used a high-powered NMR probe to study various brush samples. High-powered probes are typically used to observe solids, which benefit from the use of very short pulses and high powered decoupling. Here, we take advantage of the ability to observe NMR signal decay after short high-powered pulses. The quadecho pulse sequence is used (also known as solid echo). The second delay in the quadecho pulse sequence, d7 in Figure 4.5, is purposely set to be shorter than what is required to get to the highest point in the FID. During processing of the data, the FID can be “left shifted” till the maximum of the FID is reached. If T_2 values are very short (restricted dynamics), more of the signal can be observed after a short pulse (here 5 μ s) vs. \sim 100 μ s pulses used when collected ^2H spectra using a lock channel on a low powered probe in the previous sections.

Even using short pulses the signal of the backbone label was not observed. In Figure 4.9a, a ^2H spectrum of (600-g-5)-d₄ was observed using the quadecho pulse sequence with d6 = 20 μ s and d7 = 9 μ s with a 90° pulse of 5.3 μ s at 6 dB with a 500 ms recycle time and sweep width of 50 kHz. The brush with $\text{DP}_{\text{sc}} \sim 5$ was used to increase the concentration of

the label. However, the only intensity comes from the natural abundance signal of the side chains overlapping to form one large peak (~400 Hz linewidth). We can use this linewidth information, however, to simulate spectra and try to infer dynamics information from linewidths.

Simulated spectra can be created by knowing the relative intensities of the natural abundance deuterium of the side chains to the backbone label. The ^1H spectrum in Figure 4.8a was used to identify the side chain peaks a-f (identified in Figure 4.2b). Based on spectra of the labeled backbone (BBB) (without grafted side chains) the label peak should show up at ~ 7ppm. Using this, and approximate linewidths and intensities for side chain peaks a-f, the simulated spectra in Figure 4.8 c-e were created. The linewidths for peaks a-f were estimated from the experimental spectrum in Figure 4.8b. The linewidth of the label peak was varied to be 20 Hz, 100 Hz, and 200 Hz in spectra c, d, and e, respectively.

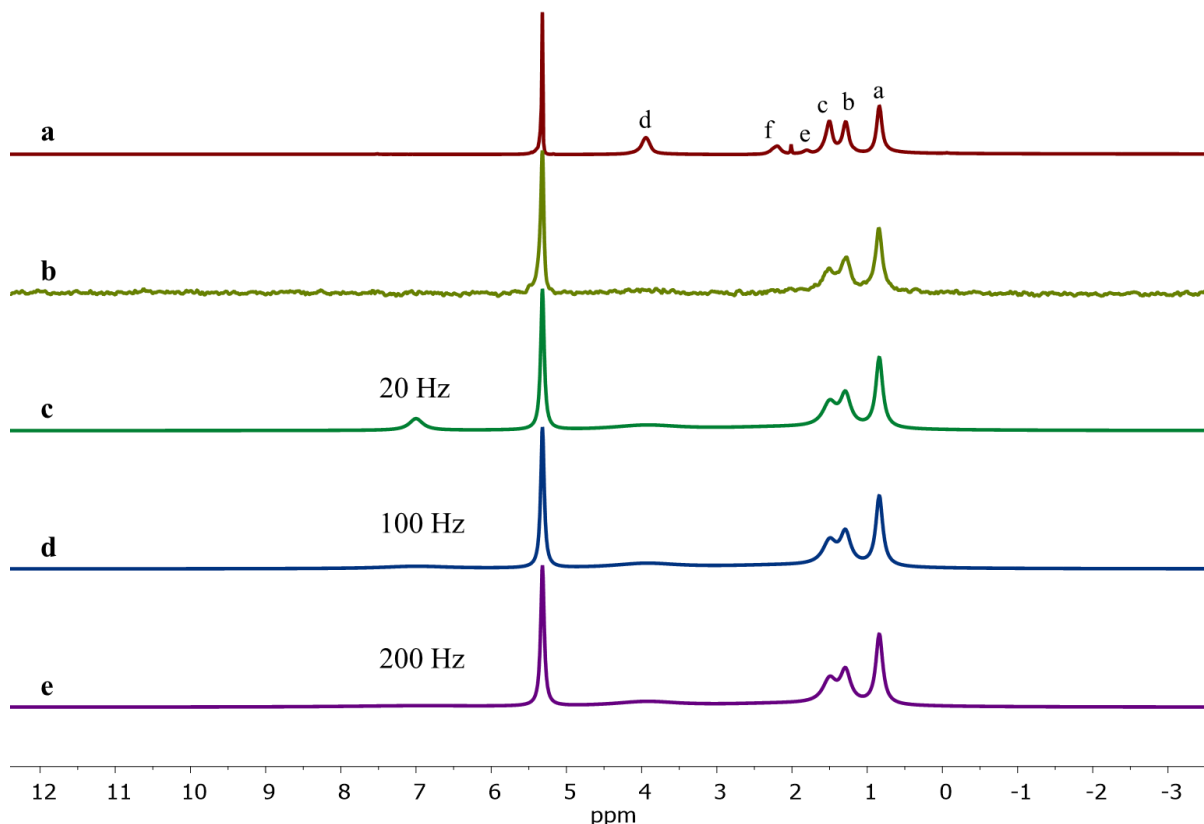


Figure 4.8. Experimental and simulated spectra of the bottle-brush (600-g-44)-d₄ in DCM. **a.** Experimental ¹H NMR spectrum of 40 wt% brush in DCM with side chain protons a-f identified, **b.** Experimental ²H NMR spectrum of 40 wt% brush in DCM, **c-e.** Simulated ²H spectra with linewidths for peaks a-f optimized to qualitatively match the experimental spectrum (**b**). The linewidths ($\nu_{1/2}$) used are: 10 Hz (a), 15 Hz (b), 20 Hz (c), 100 Hz (d), 200 Hz (e), and 200 Hz (f). The linewidth for the label peak is varied in the simulated spectra c-e to be 20 Hz, 100 Hz, and 200 Hz, respectively.

It is clear that a linewidth of more than 100 Hz would not be visible. From these linewidths, a correlation time can be inferred using the estimate for T_2 from the linewidth in Hz ($\nu_{1/2}$) in Equation 4.6.

$$\nu_{1/2} = \frac{1}{\pi T_2} \quad (4.6)$$

An approximate correlation time can be calculated from T_2 using Equation 4.5. For a linewidth of 20 Hz a correlation time $\tau_C = 0.12$ ns is found, for 100 Hz, $\tau_C = 0.62$ ns, and for

200 Hz, $\tau_C = 1.2$ ns. This means that the lower bound for correlation times that can be detected is ~ 1 ns as the corresponding peak is too broad to be observed.

In Figure 4.9a, a ^2H spectrum of the neat brush with $\text{DP}_{\text{sc}} \sim 5$ ((600-*g*-44)- d_4) is shown. For the neat brush, the natural abundance signals from the side chains are not resolved because of significant line broadening. Using a linewidth for the natural abundance side chains of 200 Hz provides a qualitative fit to the experimental spectrum in Figure 4.9a. In Figure 4.9b-d, the linewidth of the label is varied using the correct ratio of the ^2H label to the natural abundance of the methyl group on the side chain; the ratio is 2:1. The brush with shorter side chains was used to try to detect a broad peak coming from the label. The linewidths of the label are estimated to be 200 Hz, 400 Hz, and 1000 Hz. These linewidths correspond to approximate correlation times of 1.2 ns, 2.5 ns, and 6.2 ns, respectively. Therefore, we can conclude that the ^2H experiment is not sensitive to nanosecond or slower dynamics.

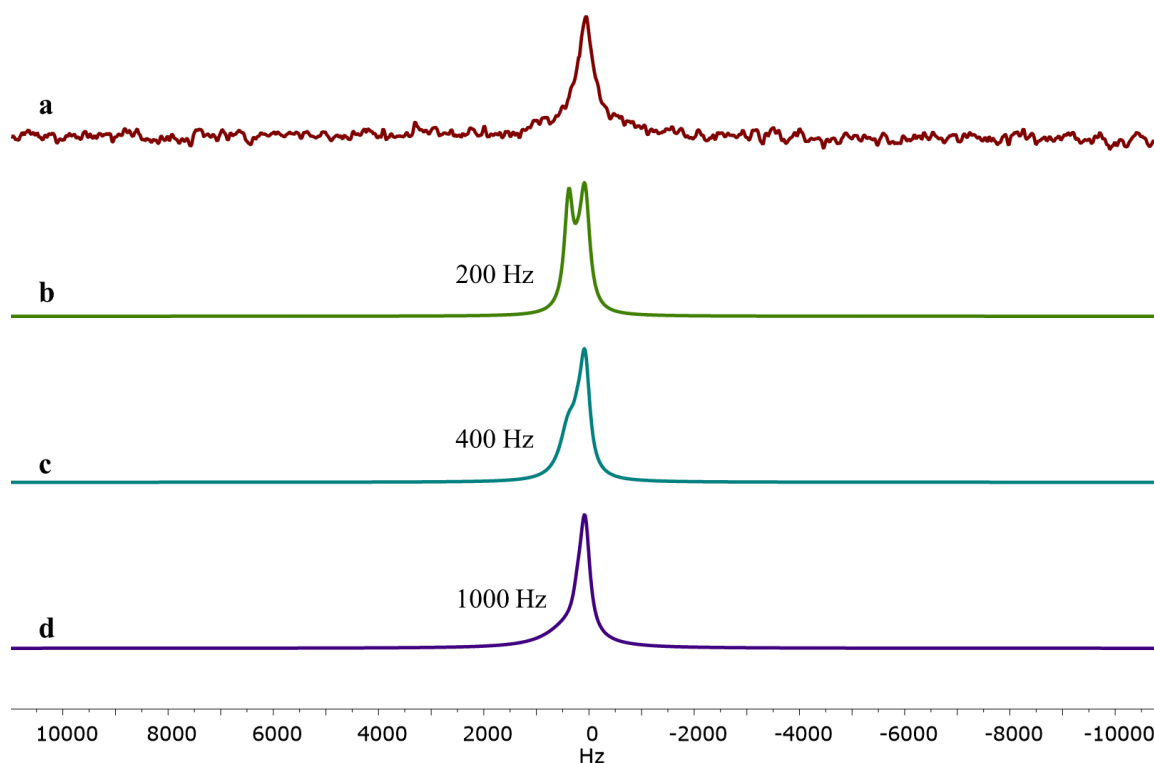


Figure 4.9. Experimental and simulated spectra of the neat bottle-brush (600-g-5)-d₄
a. Experimental ²H NMR spectrum **b-d.** Simulated ²H spectra with linewidths for peaks a-f optimized to qualitatively match the experimental spectrum (**a**). The linewidth ($\nu_{1/2}$) used for the natural abundance side chains is 200 Hz. The linewidth for the label peak is varied in the simulated spectra b-d to be 200 Hz, 400 Hz, and 1000 Hz, respectively.

4.4 Conclusion

Labeled linear and bottlebrush macromolecules were synthesized via ATRP from a tagged ATRP diinitiator. The design of the diinitiator allowed for embedding of quinone-d₄ ring in the polymer center, thus enabling the dynamics study via ²H NMR. The dynamics of the backbone “stem” of bottlebrush macromolecules are severely limited by the densely crowded array of grafted side chain “bristles.” Slow dynamics dominate even when the average bristle length is very short (e.g., DP_{sc} ~ 5) preventing the observation of a high resolution ²H NMR spectrum of deuterium labeled backbone. Efforts to detect the latter by

signal-averaging resulted in appearance of the NMR resonances from natural abundance deuterium in the mobile butyl ester sheath on the exterior of the bristle grafts. But even in that relatively mobile sheath, a gradient of molecular dynamics was evident: motion slows as one approaches the bristle graft contour. Moreover, we anticipate that this gradient is convolved with a second gradient of mobility, stiffening of the grafted bristle as one moves along the bristle to the BBM backbone. In summary, there is a hierarchy of dynamics in BBMs: i) an essentially static arrangement of the backbone within the core of the bottlebrush with its segmental mobility essentially governed by rotational diffusion of the entire macromolecule; ii) constrained bristle contour dynamics, especially within the densely grafted array of side chains near the backbone; iii) rapid dynamics in the aliphatic sheath surrounding each bristle near its free end.

CHAPTER 5: LIQUID CRYSTAL THERMOSETS: HIGH PERFORMANCE THERMOSET RESINS

5.1 Introduction

In the 1970s, liquid crystal polymers (LCPs) were touted as the next generation of high performance, high temperature (HT) polymers, but processing challenges attenuated the widespread adoption of LCPs. In a series of reports pioneered by researchers at NASA, (refs) liquid crystal end-functionalized “macro-monomer” precursors were shown to lead to a new class of HT liquid crystal thermosets (LCTs).

5.1.1 High Performance Polymers

High performance polymers (sometimes referred to as high temperature polymers) are defined by their exceptional mechanical properties especially at high temperatures. Beginning in the 1950s, the development of high performance polymers grew mostly out of a need from the aerospace industry that would benefit from strong and lightweight materials able to withstand harsh conditions for extended periods of time. High performance polymers are used in various applications, e.g. adhesives, films, and most notably in fiber reinforced polymer matrix composites (PMCs) where high performance polymers are used as the polymer matrix and are typically reinforced with carbon fibers to make extremely strong, lightweight materials.¹⁰²

Some of the earliest efforts in high performance polymers included chemical architectures with all-aromatic chains which result in very rigid materials with excellent thermomechanical properties. One such polymer is Kapton™, a polyimide shown in Figure

5.1a. Liquid crystalline architectures are popular for use in high performance polymers because of their high rigidity and orientational order, e.g. KevlarTM, a para-aramid liquid crystal synthetic fiber. To use these materials as a polymer matrix, however, is impossible because of their inability to be melted and therefore melt-processed. All-aromatic liquid crystalline polymers are very difficult to process as they must be processed from solution, typically requiring very harsh chemicals like concentrated sulfuric acid.

In the 1970s, in an effort to develop melt-processable high performance polymers, several new materials started being produced. Some of these are shown in Figure 5.1b: polyphenylene sulfide (PPS, i.e. FortronTM), polyetherimide (PEI, i.e. UltemTM), and polyetheretherketone (PEKK, i.e. VictrexTM). Although these polymers can be melt processed, their thermomechanical properties are far below what can be achieved by all-aromatic and liquid crystalline polymers.

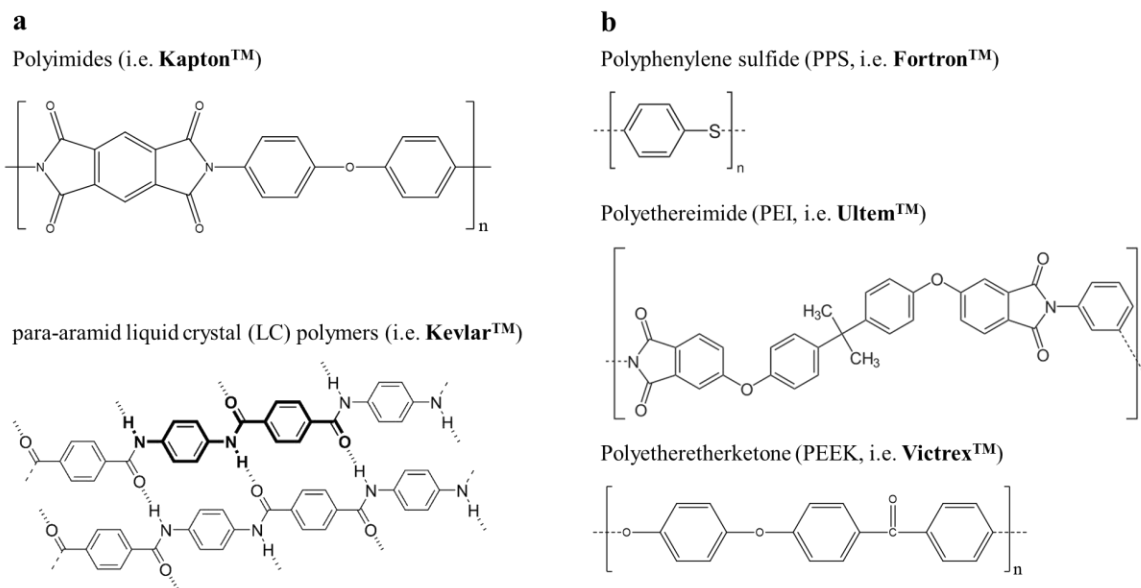


Figure 5.1a. All-aromatic high performance polymers and **b.** melt processable high performance polymers.

5.1.2 Current Polymer Matrix Composites

The high performance polymer field has continued to grow with the increasing demand for high performance polymers for adhesives, composite matrices, and films. The aim of most high performance materials is to have materials with very high modulus that can be melt processed. Typical ways to increase the moduli of polymers include increasing the covalent cross-link density and/or reinforcing them with glass, carbon fibers, or nanoparticles—e.g. carbon nanotubes and graphene (e.g. for PMCs). Many fiber-reinforced polymer matrix composites are limited by the inherent properties of the matrix resin, e.g. its heat-deflection temperature, its coefficient of thermal expansion relative to the reinforcement, and its chemical stability in harsh environments. Additionally, the fiber-matrix interface will impact the properties of polymer matrix composites (PMCs). If this interface is weak, fiber pullout occurs, which affects PMC toughness. The two major classes of polymers used in current PMCs are epoxides (thermosetting) and all-aromatic (thermoplastic) resins. Epoxide resins are easy to process, but have inferior mechanical properties, high moisture uptake, and poor solvent resistivity. All-aromatic resins are more difficult to process, have a high melting temperature (T_m) close to the decomposition temperature (T_d), and have high melt viscosities about the glass transition temperature (T_g).¹⁰²

5.1.3 High Performance Thermosets

Polymer networks used in PMCs will often employ the use of chemical cross-links are processing. When the reaction to form cross-links occurs via heat the resulting network is called a thermoset. One approach is called the “reactive oligomer” approach in which all-aromatic oligomers have reactive end-groups that cross-link at high temperatures in excess of the melting temperature of the oligomers. The use of oligomers (polymers with fewer than

20 repeat units) instead of polymers ensures accessible melting temperatures. Reactive monomers can be used as well, however, a high reactive group density means that the final thermoset is often very stiff and brittle.

5.1.3.1 Liquid Crystal Thermosets

The “reactive oligomer” approach was implemented by researchers at NASA to invent a new class of liquid crystal thermosets (LCTs) that circumvented the aforementioned limitations in **Section 5.1.2**.¹⁰³ Well-known all-aromatic main-chain liquid crystal chemistries are used as the oligomer. One such example of a well-known liquid crystalline polymer (LCP) is VectraTM with $T_g = 110^\circ\text{C}$ and $T_m = 280^\circ\text{C}$ shown in Figure 5.2. The use of Vectra as a polymer matrix material is implausible as it is difficult to process because the melting temperature is very close to the decomposition temperature, ($T_d \approx 330\text{-}360^\circ\text{C}$).

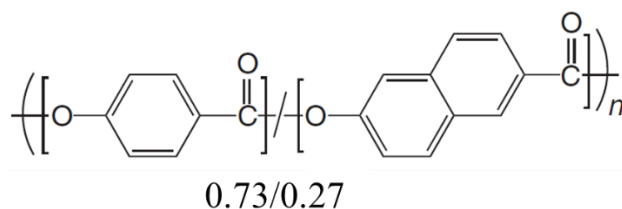


Figure 5.2 The LCP VectraTM.

Using the same chemistry as Vectra, this LCT is prepared from macro-monomer with reactive end-groups (Figure 5.3) and is a precursor to a new class of high performance polymer matrix materials. LCTs based on this concept can have very high glass transition temperatures (T_g up to 450°C) and decomposition temperatures ($T_d > 500^\circ\text{C}$), and exhibit extremely strong bonding to glass, metal, and carbon fibers, a prerequisite for a strong fiber-matrix interface in composites. In the melt phase of the reactive macro-monomer precursor ($T_m \sim 300^\circ\text{C}$) before curing, the fluid is a low viscosity nematic liquid crystal that can be

readily processed. In the melt, the uniaxial nematic phase generates spectacular properties along the nematic director \mathbf{n} , properties that can be distributed throughout the bulk via processing strategies. Figure 5.4a provides a depiction of the nematic liquid crystalline phase of LCT showing a preferred direction of aligned macromonomers (ellipsoids) along the direction, \mathbf{n} .¹⁰⁴

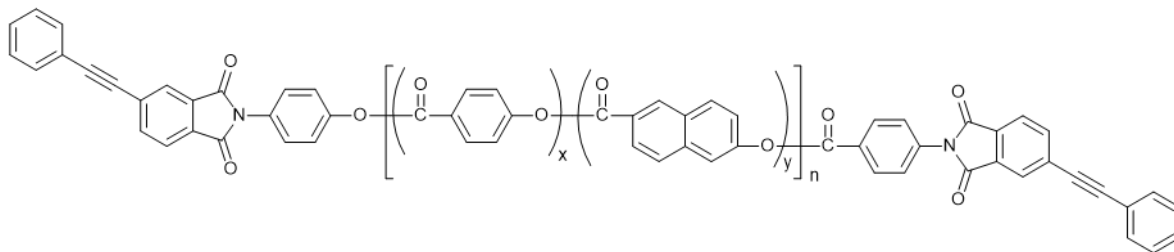


Figure 5.3 LCT reactive oligomer

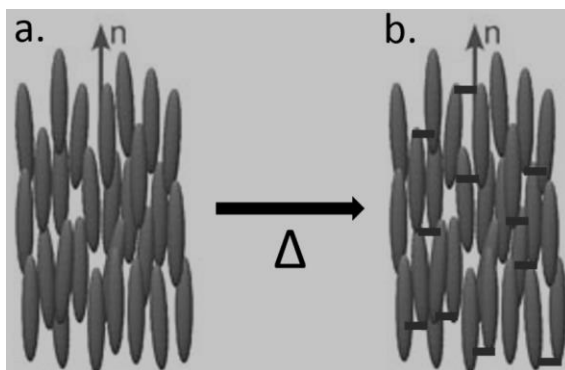


Figure 5.4. Liquid crystal thermoset **a.** before and **b.** after curing with preferred direction along \mathbf{n} . Cross-links are represented by the black bars.

This new family of reactive all-aromatic liquid crystal macro-monomers can be processed just like a traditional thermoplastic. After molding, chain extension and/or cross-linking via the phenylethynyl end-groups is initiated. The cured product retains its orientation described locally by the nematic direction, \mathbf{n} (Figure 5.4b). The advantages of using a reactive liquid crystal macro-monomer over traditional composite resins have to do with processing. LCTs have an infinite shelf-life, accessible melting temperatures, and the

nematic liquid crystal melt has a low viscosity, which makes processing composites easy. After cross-linking, the nematic thermoset has no residual crystallinity and exhibits very high, after-cure glass transition temperatures (T_g s of 200-400°C and possible).¹⁰²

5.1.4. Curing of phenylethynyl based systems

The choice of reactive end-group in designing a high-temperature thermoset is important. Phenylethynyl-based systems lead to desirable processing characteristics. The reactive end-group effectively slows down radical formation, which delays cross-linking until temperatures greater than 300°C are reached. This allows the high-melting reactive oligomer to be processed in the melt-state before cross-linking. Another interesting feature of phenylethynyl-based systems relates to the after-cure properties. As the molecular weight of the precursor increases, the tensile strength, modulus, and elongation at break increase.¹⁰² This indicates that the curing mechanism may involve chain extension in addition to cross-linking. In order to design new high-temperature polymers, it is important to understand this mechanism both in terms of the kinetics and the final products formed.

5.2 NMR Methods

As stated, it is important to understand the curing chemistry associated with the LCT reactive oligomer in Figure 5.3. The ultimate goal was to monitor and characterize the curing chemistry associated with LCTs and its impact on the molecular organization it is liquid crystalline phase. However, the LCT reactive oligomer is intractable and very few techniques exist to interrogate the curing chemistry in real time. In the remaining sections, a combination of solid-state NMR techniques and high-temperature liquid-state NMR is used to characterize the curing chemistry associated with the LCT reactive oligomer. All solid-state spectra were analyzed as powders with a Bruker360 spectrometer using a magic-angle

spinning double resonance probe. Solid-state ^{13}C NMR spectra were collected using a cross-polarization pulse sequence (Figure 5.5) with ^1H decoupling. The contact time was set to 3 ms (where the ^{13}C mixing pulse power level was 7.7 dB and the ^1H spin locking power level was 7.6 dB) with 4k time domain points, 27.172 kHz sweep width (18.4 μs dwell time), pre-scan delay of 6 μs (required by the instrument), recycle time (d1) of 5 s, ^1H 90° pulse width of 5 μs at 5 dB, magic angle spinning was run at 10 kHz, and the carbon and proton frequencies were 90.5656 and 360.1307 MHz, respectively. Solid samples were packed into 4-mm ZnO_2 rotors. The theory behind the CP/MAS experiment is in the next section.

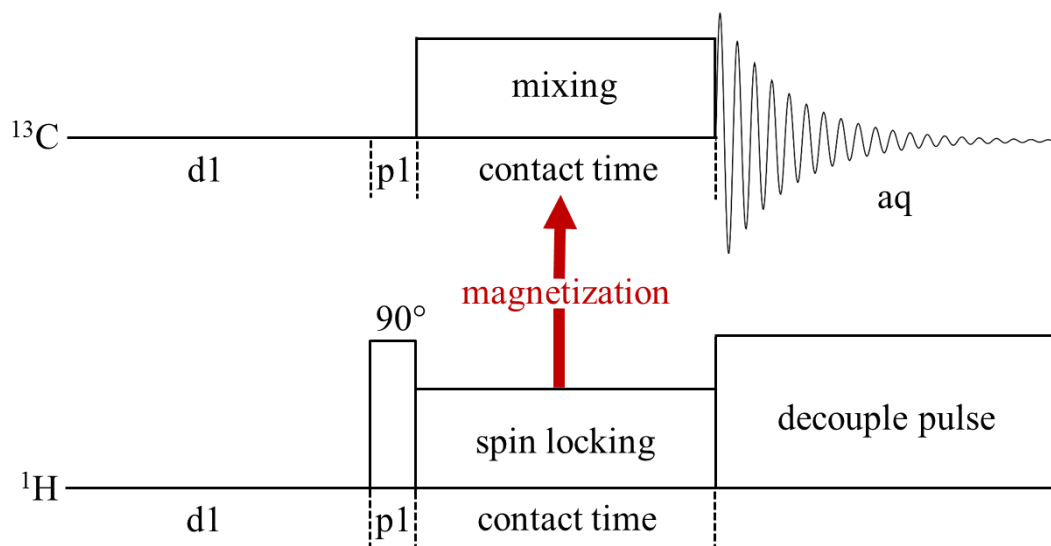


Figure 5.5. ^1H broadband decoupling ^{13}C NMR pulse sequence using cross polarization wherein the ^1H nuclei are excited with a 90° pulse and transferred to ^{13}C nuclei during the contact time.

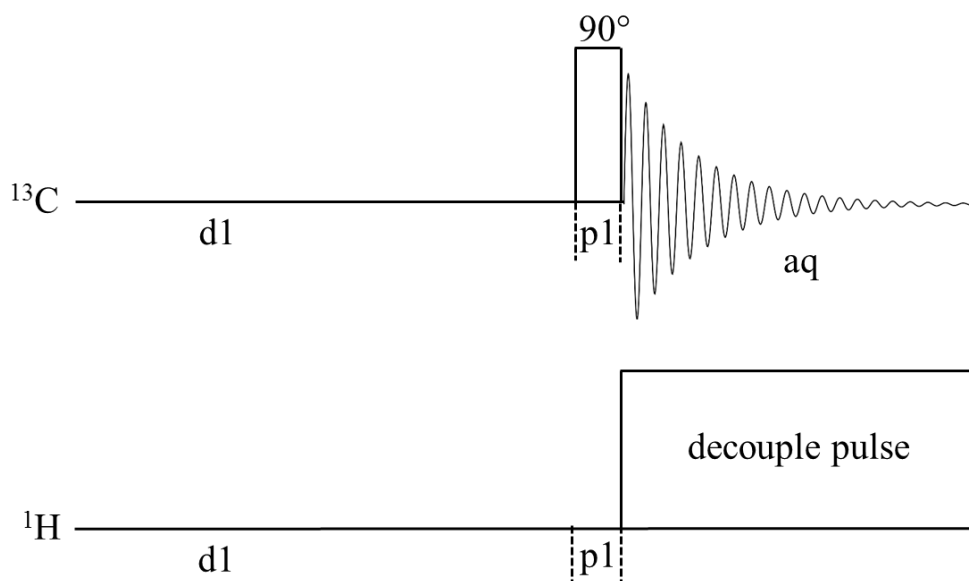


Figure 5.6. ^1H broadband decoupled ^{13}C pulse sequence.

For high-temperature (liquid state) studies of LCT materials, a simple single pulse ^{13}C NMR experiment is used with a ^{13}C pulse width of $2.15\ \mu\text{s}$ (3 dB) and ^1H broadband decoupling using an inverse gated ^{13}C NMR experiment (Figure 5.6) where decoupling occurs during the acquisition time (41 ms at -3 dB) with 4k time domain points, 50 kHz sweep width (10 μs dwell time), 6 μs pre-scan delay, recycle time (d1) of 2 s, and the carbon and proton frequencies were 90.5638 and 360.1335 MHz, respectively. Conventional liquid-state NMR probes cannot go above $\sim 100^\circ\text{C}$. Therefore, an existing probe had to be modified to access the melting and curing temperatures of LCT. The modified probe (Figure 5.7) was able to reach temperatures in excess of 400°C . The probe was modified by removing the coil responsible for irradiating the sample with a radiofrequency pulse. By changing the number of turns...

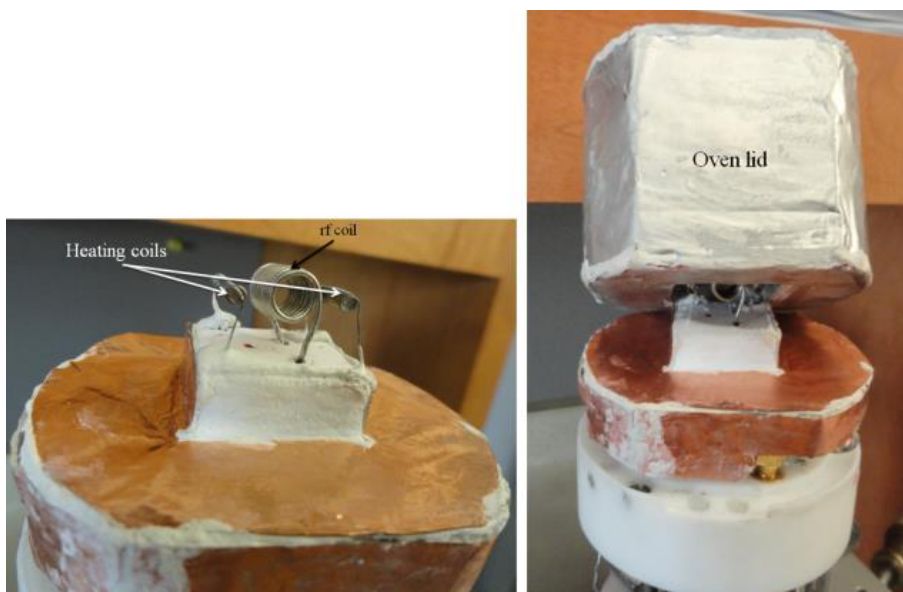


Figure 5.7. Home-built oven for ^{13}C NMR probe capable of reaching over 400°C .

5.2.1 Solid State ^{13}C NMR

NMR spectra in the solid state have much lower resolution than in liquids and solutions due to the angular-dependence of anisotropic interactions. Various strategies exist, however, to improve the resolution in the solid state and extract meaningful information. Here we focus the discussion on three methods typically used in solid state NMR; high-power ^1H decoupling, cross polarization (techniques that manipulate nuclear spins with radiofrequency pulses and delays), and magic angle spinning (a technique that uses mechanical rotation of the sample).

A ^{13}C spectrum of a solid without any of these resolution enhancement techniques results is called a “powder pattern.” A static ^{13}C NMR experiment of the LCT oligomer is shown in Figure 5.8. Because carbon chemical shifts and direct dipolar couplings are influenced by the orientation of the molecule with respect to the magnetic field, a featureless powder pattern results. This orientation dependence of the chemical shift is termed the

chemical shift anisotropy or CSA. In isotropic liquids, thermal motions lead to fast reorientations of each molecule, which averages the CSA. In powders, we see a featureless powder pattern because all orientations of the molecules are equally likely.

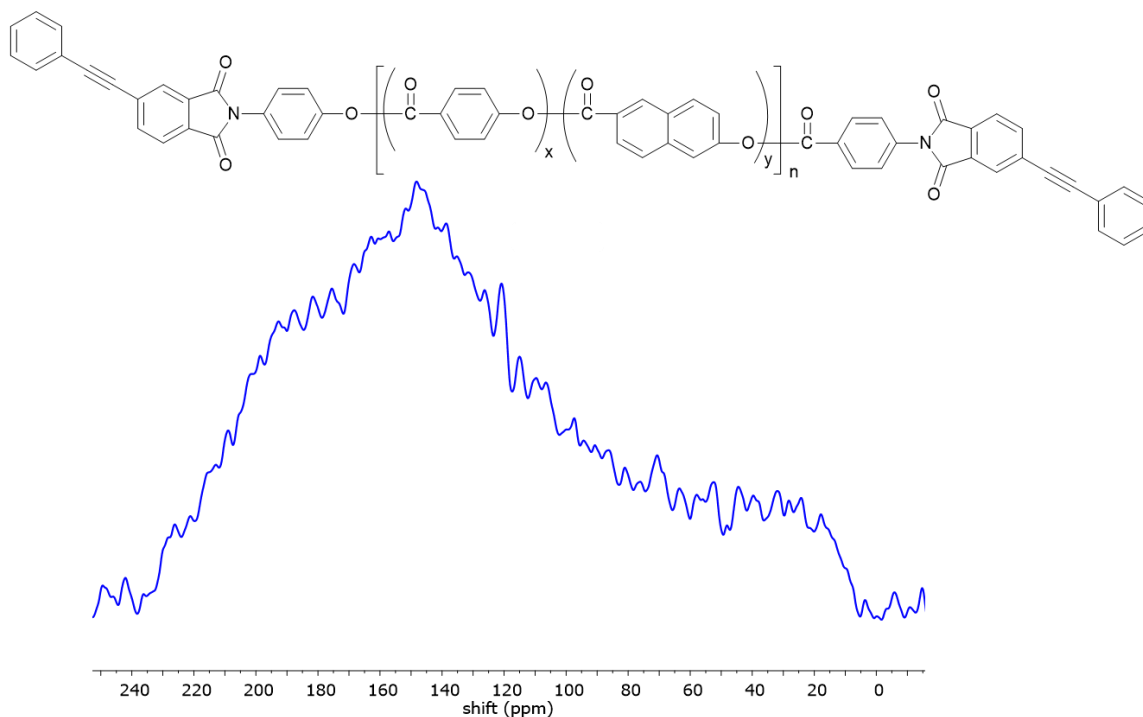


Figure 5.8. ^{13}C powder pattern of the LCT precursor oligomer

In a single crystal (one orientation), however, a single line for each distinct carbon chemical shift results. In Figure 5.9, from ref 3, a depiction of a single crystal spectrum is shown where different orientations of the crystal with respect to the magnetic field result in different chemical shifts. An ideal powder pattern (for one type of carbon) is shown which results from the superposition of many sharp peaks with difference frequencies, with each one coming from a different crystallite with a particular orientation with respect to the magnetic field. The powder pattern in Figure 5.8 is more complicated because of the number of magnetically inequivalent carbons.

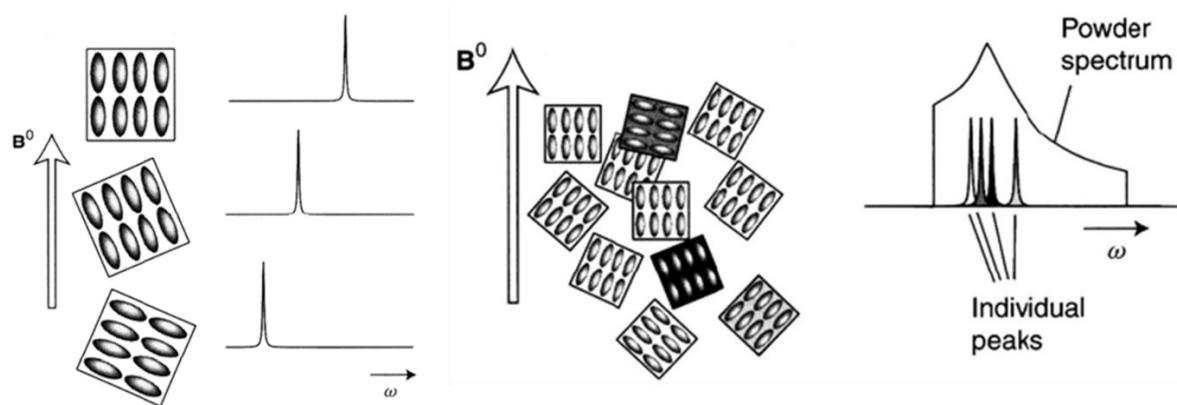


Figure 5.9. Representative, idealized spectra from single crystals with one orientation (left) and powders with random orientations (right). From ref 3.

As stated above, many techniques exist to simplify these broad spectra and increase resolution. One involves mechanical manipulation of the sample, called “magic angle spinning,” where the sample is placed in a rotor and spun at the magic angle: 54.7° . The mechanical rotation at the magic angle mimics the effect of isotropic molecular motion. The anisotropic interactions are removed, leading to a solid state spectrum that resembles that of an isotropic liquid. The magic angle comes from the angular dependence of the chemical shift interaction (and dipolar interaction) which is multiplied by $3\cos^2\theta - 1$ where θ is the angle between the tensor principal axes system direction and the external magnetic field; setting this equal to zero and solving for θ results in $\theta = 54.7^\circ$.

In addition to mechanical manipulation of the powder, we employ two additional techniques for simplifying the solid state spectrum, although it is noted that several other pulse sequences exist to increase the resolution of solid state spectra. The first is broadband proton decoupling, which involves irradiation the sample with a continuous radiofrequency (*rf*) pulse at the ^1H Larmor frequency. The efficiency of the decoupling depends on the power of the *rf* pulse and whether or not the ^1H frequency is “on resonance.” This

decoupling *rf* pulse effectively cancels out *J*-coupling interactions between ^{13}C and ^1H nuclei; each ^{13}C shows up as a single resonance with no splitting caused by the *J*-interaction. The second technique used is cross polarization (CP) which effectively causes ^{13}C and ^1H nuclei to precess at the same frequency. This requires the energy levels of the two different nuclei to be matched; often called the “Hartmann-Hahn condition”¹⁰⁵ and the result is that magnetization can be transferred from the abundant ^1H to ^{13}C nuclei. The Hartmann-Hahn condition is given in Equation 5.1 where B_1 is the magnetic field strength, γ is the gyromagnetic ratio for each nuclei, and $\gamma^{^1\text{H}} / \gamma^{^{13}\text{C}} \cong 4$ meaning a 4X sensitivity enhancement is possible. Also, protons typically have shorter values of T_1 , therefore a shorter recycle delay is possible which reduces the time of the experiment.

$$\gamma^{^{13}\text{C}} B_1^{^{13}\text{C}} = \gamma^{^1\text{H}} B_1^{^1\text{H}} \quad (5.1)$$

A ^{13}C NMR broadband ^1H decoupled CP/MAS spectrum of the LCT oligomer is shown in red in Figure 5.10. The spinning rate was 10 kHz. It is clear that the spectrum is significantly simplified by the resolution-enhancing techniques.

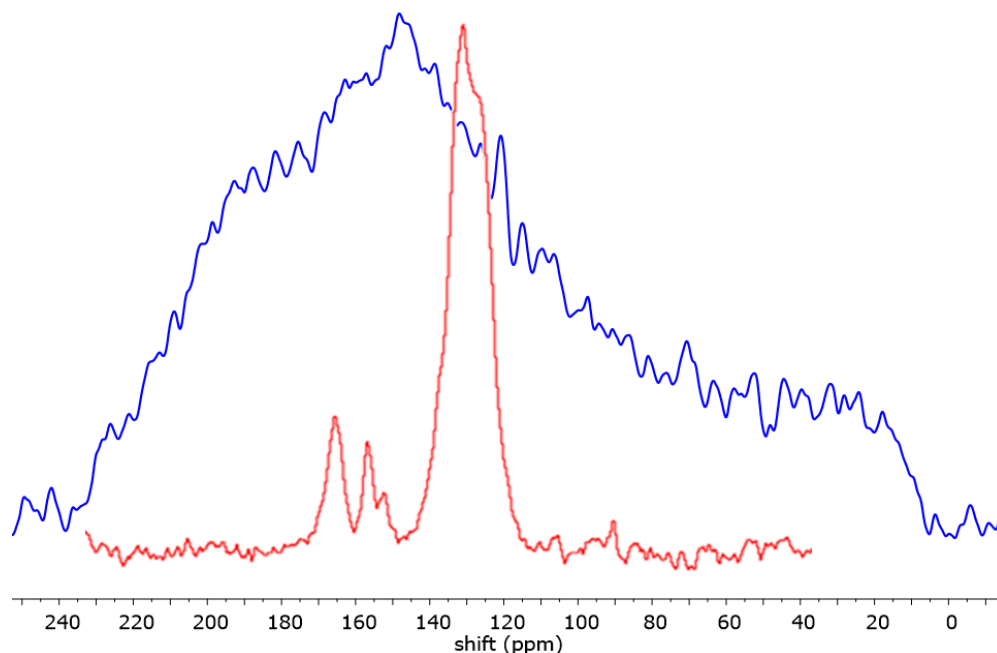
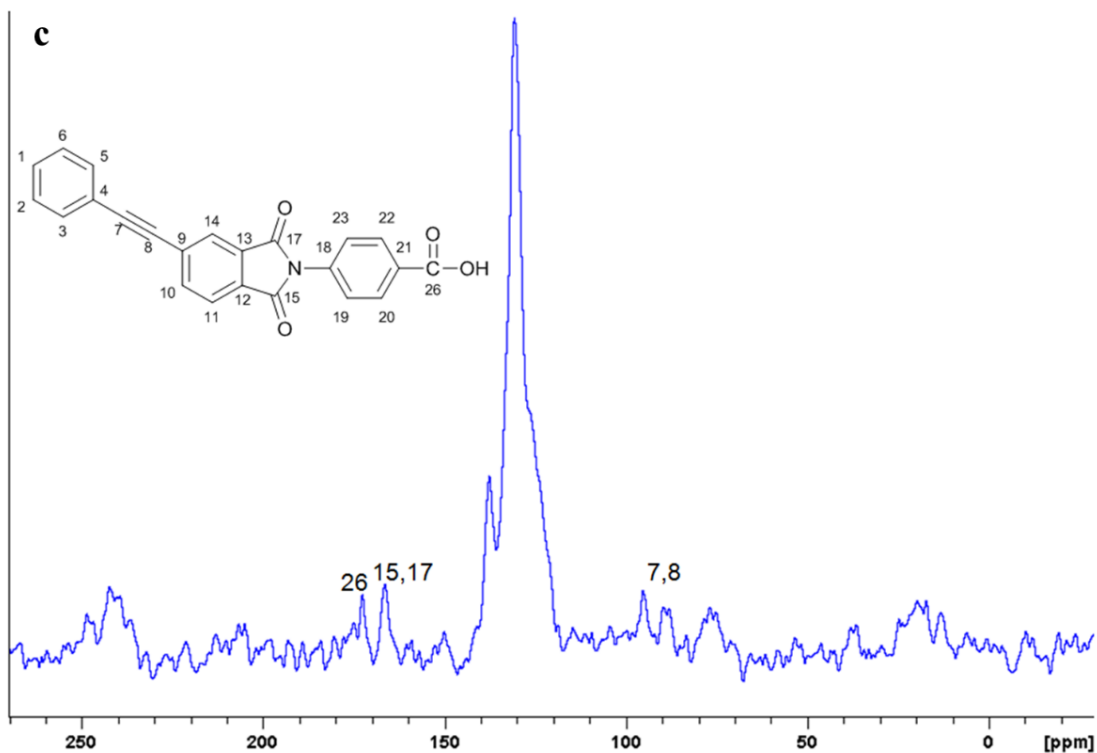
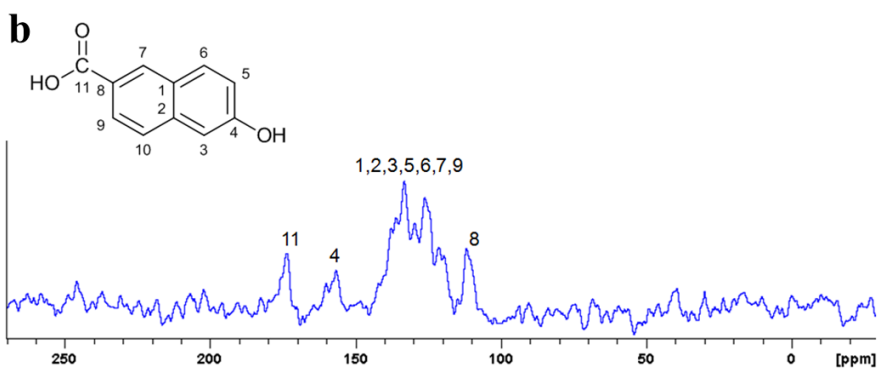
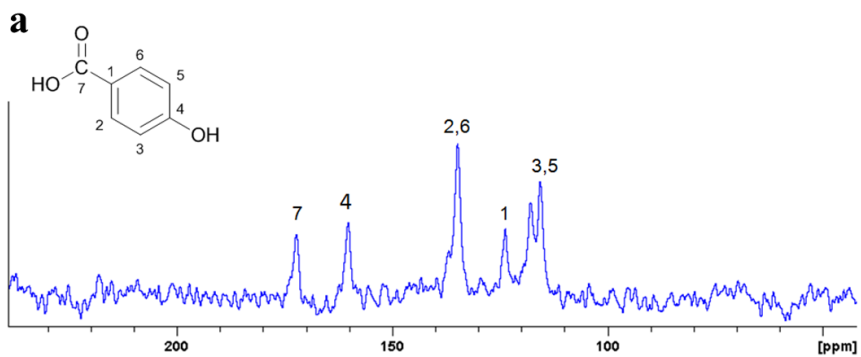


Figure 5.10. ^{13}C NMR spectra of the LCT oligomer. The blue spectrum is taken with a single ^{13}C NMR pulse, and the red spectrum is taken with ^1H broadband decoupling and CP/MAS with 10 kHz spinning rate.

5.3 Results and Discussion

5.3.1 Solid-State Spectra of LCT oligomer precursor

The LCT oligomer precursor (Figure 5.3) with molecular weight 1000 g/mol and its starting monomers and end-groups are readily available and were used to assign the ^{13}C CP/MAS spectrum (Figure 5.10, red). Synthesis of phenylethynyl terminated LCT oligomer was built around the two monomers, 4-hydroxybenzoic acid (HBA) and 6-hydroxy-2-naphthoic acid (HNA), the chemical building blocks of VectraTM (Figure 5.2), with the reactive end-groups N-(4-carboxyphenyl)-4-phenylethynylphthalimide (PE-COOH) and N-(4-acetoxyphenyl)-4-phenylethynylphthalimide (PE-OAc).¹⁰³ ^{13}C CP/MAS spectra of these four starting materials (Figure 5.11) were collected, digitally combined (Figure 5.12), and compared to the LCT precursor oligomer (Figure 5.13).



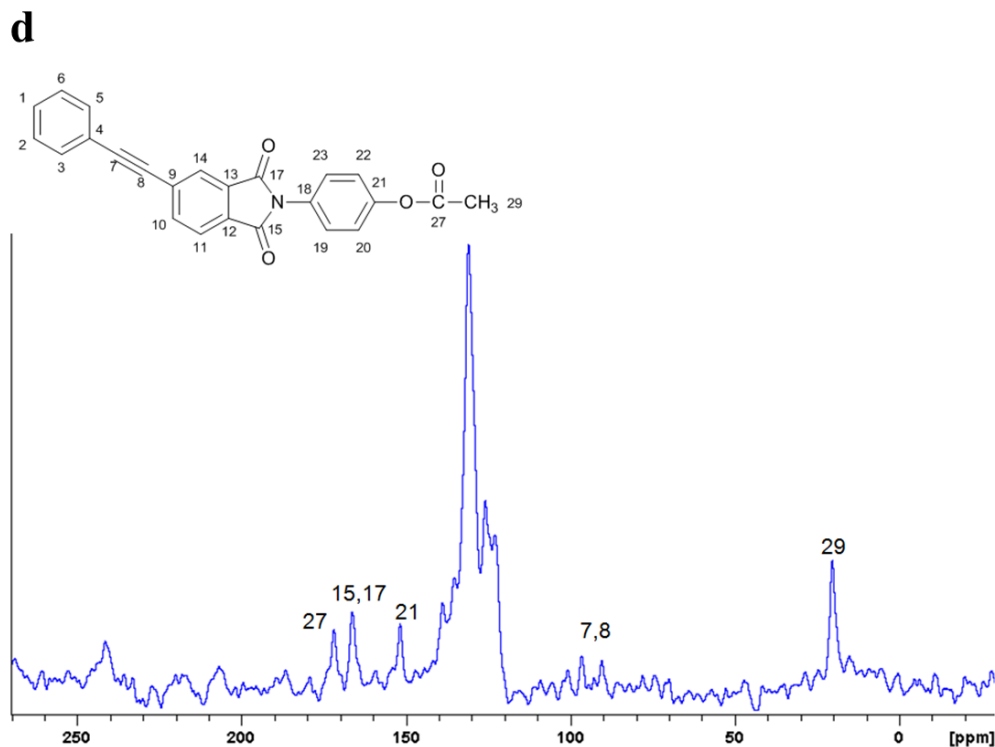


Figure 5.11. ¹H broadband decoupled ¹³C CP/MAS spectrum of **a.** HBA, **b.** HNA, **c.** PE-COOH, and **d.** PE-OAc

Using the spectra from Figure 5.11, the peaks in the spectrum of the LCT oligomer precursor can be assigned; numbered peaks correspond to carbons on the structure of each monomer/end-group and the remaining carbons are assigned to the aromatic region between 120 and 140 ppm.

Figure 5.12 represents the sum of the monomer/end-group spectra. The structure of the LCT oligomer in Figure 5.3 has an approximate molecular weight of 1000 g/mol. This means it will have a relatively high concentration of reactive end-group functionalities resulting in high after-cure cross-link density.¹⁰² The number of repeating units in the final structure of the LCT precursor is about six and the respective amounts of HBA and HNA are 73% and 27% ($x = 0.73$ and $y = 0.27$ in the structure in Figure 5.3).¹⁰³ The digitally combined summation spectrum in Figure 5.12 represents this ratio of monomers and end-

groups. We expect the spectrum of the 1000 g/mol LCT to be similar to the red spectrum in Figure 5.10 bearing in mind that some peaks are lost after the reaction and some peaks are shifted due to changes in the chemical environment. Based on the individual spectra, we can globally assign regions in the spectra to certain chemical groups. These labels are included in Figure 5.12.

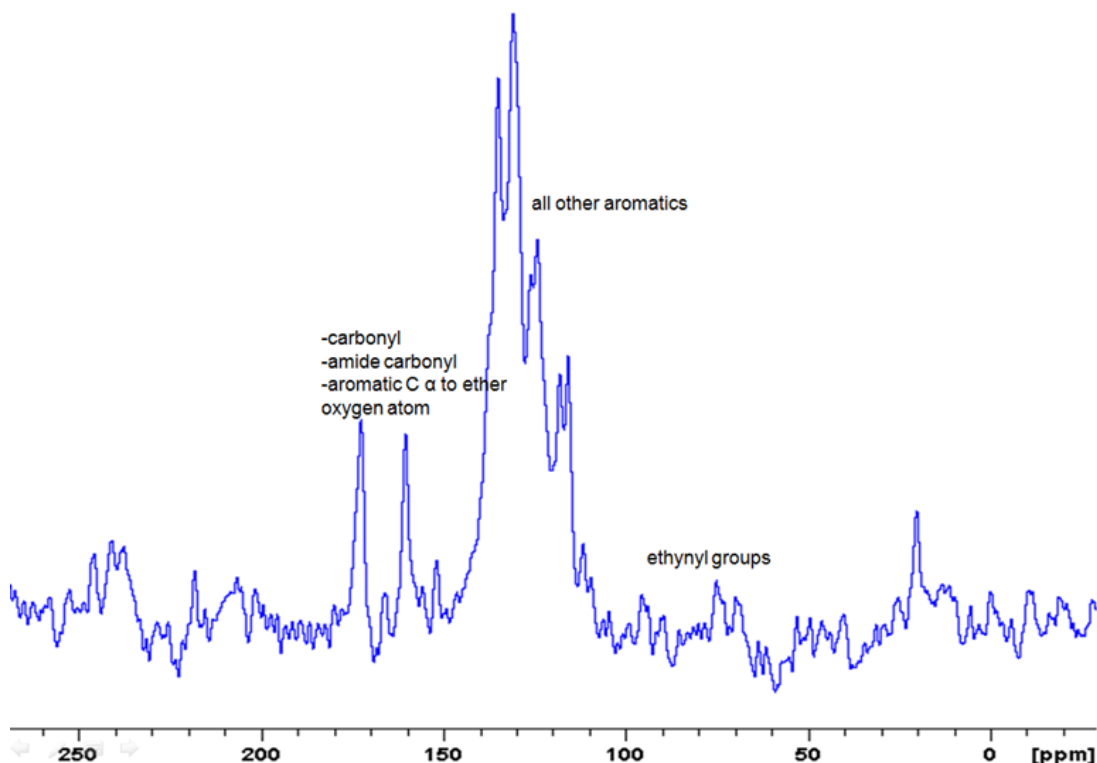


Figure 5.12. Sum of ^{13}C CP/MAS spectra of HBA, HNA, PE-COOH, and PE-OAc (scaled to ratios of monomers and end-groups).

Figure 5.13 is an overlay of the spectrum in Figure 5.12 and the LCT precursor oligomer spectrum. Using this information along with similar peak assignments by Roberts et al.,¹⁰⁶ we can assign chemical shifts to aid in tracking the curing chemistry. The peak at 165 ppm represents the three carbonyl carbons. The peak is shifted upfield after reaction of the monomers and end-groups because the carboxylic acid groups reacted to form ester groups. The peaks at 156 ppm and 151 ppm are due to the aromatic carbon atoms α to the

ether oxygen atom and the amide carbonyl groups, respectively. This is explained by the fact that the chemical environment around the amide carbonyl groups does not change much as a result of the reaction, while the aromatic carbon atoms α to the ether oxygen atom do see a change in chemical environment. The large peak between 120 and 140 ppm can be broadly attributed to all remaining aromatic carbons. Lastly, a very small peak is present at 90 ppm. Based on the findings of Roberts et al.,¹⁰⁶ this falls in the region of ethynyl carbons.

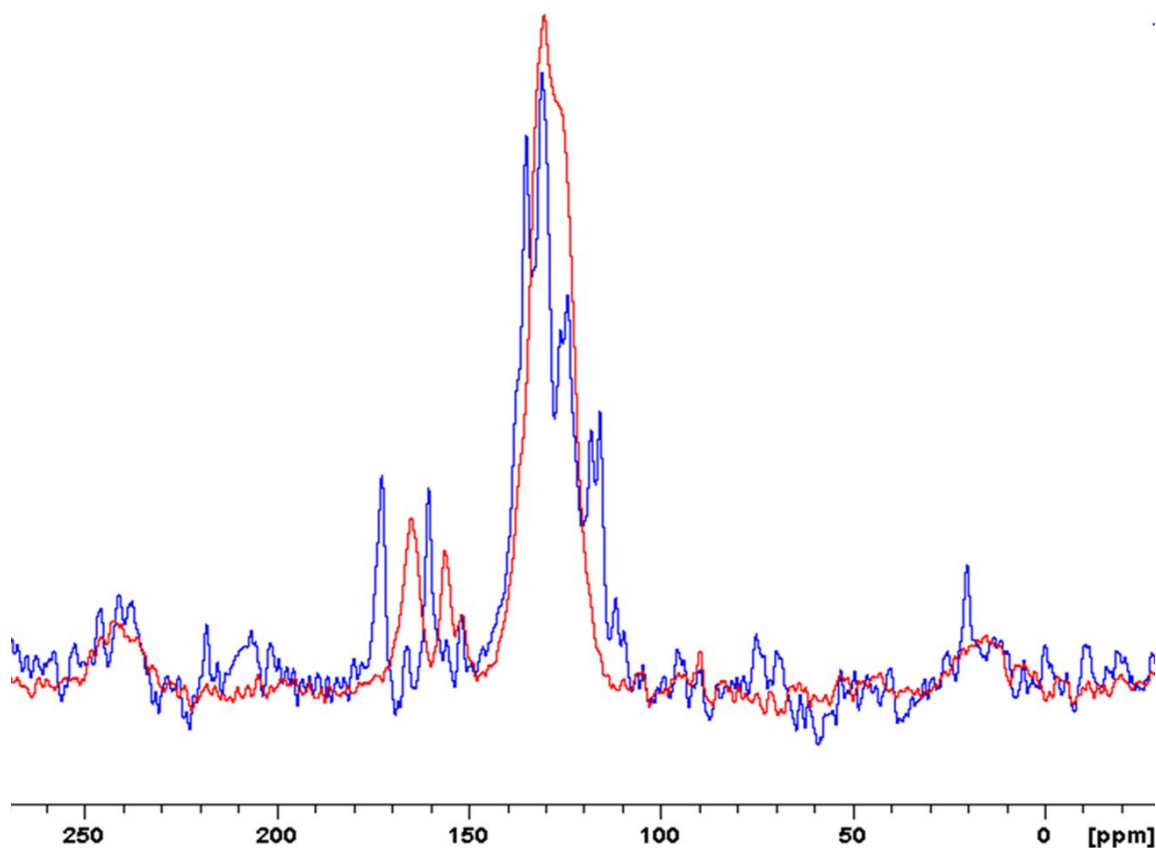


Figure 5.13. Overlay of Figures 5.12 (sum, blue) and 5.10 (red).

5.3.2 NMR of Liquid Crystal Thermosets

Since the overall properties of a thermoset resin is dictated by the structure of the crosslinks formed, it is important to understand the resin curing chemistry. However, cured

resins are difficult to characterize because of their insoluble nature. To that end, we studied static, non-spinning magnetically-aligned samples wherein the LCT chains are aligned parallel to the NMR spectrometer magnetic field. This was accomplished by merely melting the LCT into its nematic phase in the presence of the field using the probe modified to include a high temperature oven (Figure 5.7). The anticipated advantage of studying LCTS over other matrix resins in this manner is the possibility of obtaining such uniaxially aligned samples. Figure 5.14 depicts this scenario; the director \mathbf{n} of the LCT precursor oligomer is randomly oriented macroscopically, however when an external (magnetic) field is introduced, the director \mathbf{n} preferentially aligns with the field.

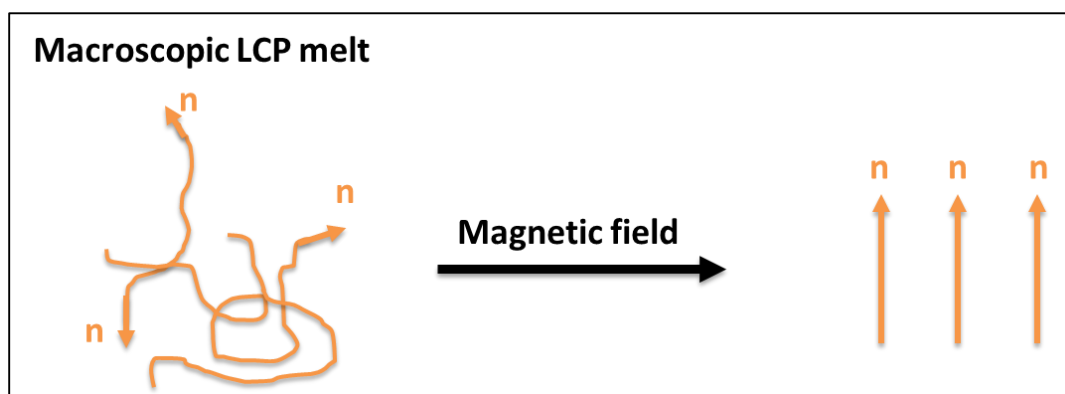


Figure 5.14. Simplified picture of a liquid crystal polymer melt before and after a magnetic field is applied.

Instead of seeing a ^{13}C NMR spectrum dominated by overlapping and broad chemical shift anisotropies indicative of a randomly oriented molecules, in the aligned liquid crystalline sample all of the NMR intensity is collapsed into discrete lines (like the single crystal case in Figure 5.9, left). In conjunction with broadband decoupling schemes to eliminate dipolar couplings between ^{13}C and ^1H spins, a high resolution spectrum is accessible.³

Roberts and coworkers¹⁰⁶ used ^{13}C NMR to investigate the cross-linking chemistry via the thermally induced reactions of the phenylethynyl group in model compounds similar to the one in Figure 5.3. They used cross-polarization enhanced magic angle spinning (CP-MAS) ^{13}C NMR (a typical NMR technique that makes a solid-state spectrum look like an isotropic liquid state spectrum) and found that the ethynyl resonances of phenylethynyl-terminated imide oligomers were readily distinguished from other carbon resonances. They suggested di- and tri-functional chemical structures resulting from the cross-linking reactions and provided chemical shifts of the associated products (Figure 5.15).¹⁰⁶

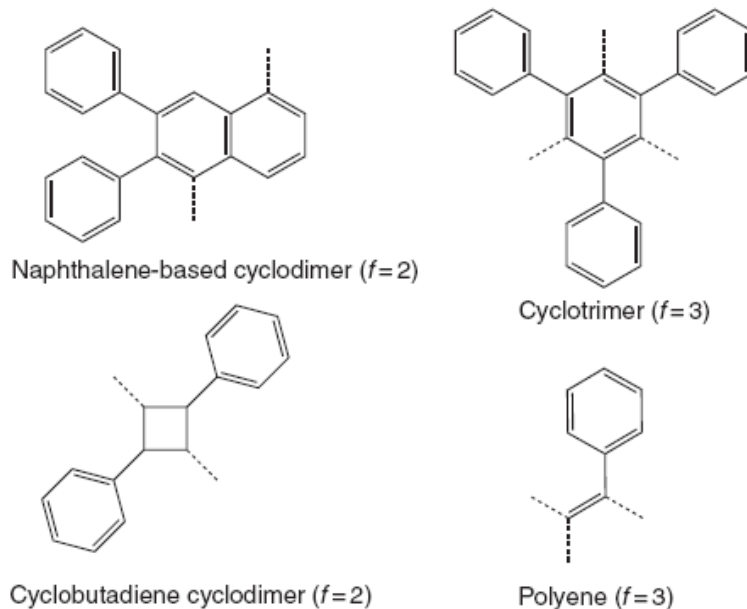


Figure 5.15. Proposed di- ($f=2$) and tri- ($f=3$) functionalized cure products of the phenylethynyl end-group chemistry. From ref 106.

Watching the curing chemistry at high temperature in real-time in the magnetic field offers many advantages over the solid-state technique. In the solid-state it is necessary to label the ethynyl carbons with ^{13}C or signal average over several hours. This is due to the fact that the cross-polarization enhancement technique typically used in solid-state NMR

does not affect the ethynyl carbons because they are not directly bonded to hydrogens.

Additionally, using high temperature NMR does not require preparing separate samples for each curing time point.

The LCT precursor spontaneously aligns along the spectrometer magnetic field merely by heading up the sample to its nematic melt (220-280°C depending on the oligomer molecular weight). It is possible to monitor the reaction products that result by changes in ^{13}C spectra and chemical shift anisotropy (CSA). The anisotropic motionally-averaged CSA is projected along \mathbf{n} parallel to the spectrometer magnetic field; hence the ^{13}C resonances are readily resolved with fewer scans than with solid-state NMR, and without labeling of the ethynyl carbons.

Figure 5.16 shows the isotropic spectrum found with CP/MAS (red) overlaid with the nematic spectrum found at ~250°C, which is well below the curing temperature. It appears that some of the chemical shifts are shifted upfield (lower values of δ), while others are shifted downfield (to higher δ). This is due to the CSA of carbon.¹⁰⁷ The CSA quantifies deviation from isotropy. This occurs when some orientations are preferred, like in anisotropic liquids and solids. Therefore, if molecular motion changes from isotropic to anisotropic, like when a liquid crystal is cooled below its nematic transition temperature, the NMR peak frequencies will change. The chemical shift is no longer an average over all orientations, but biased orientations are sampled along the main spectrometer magnetic field.³

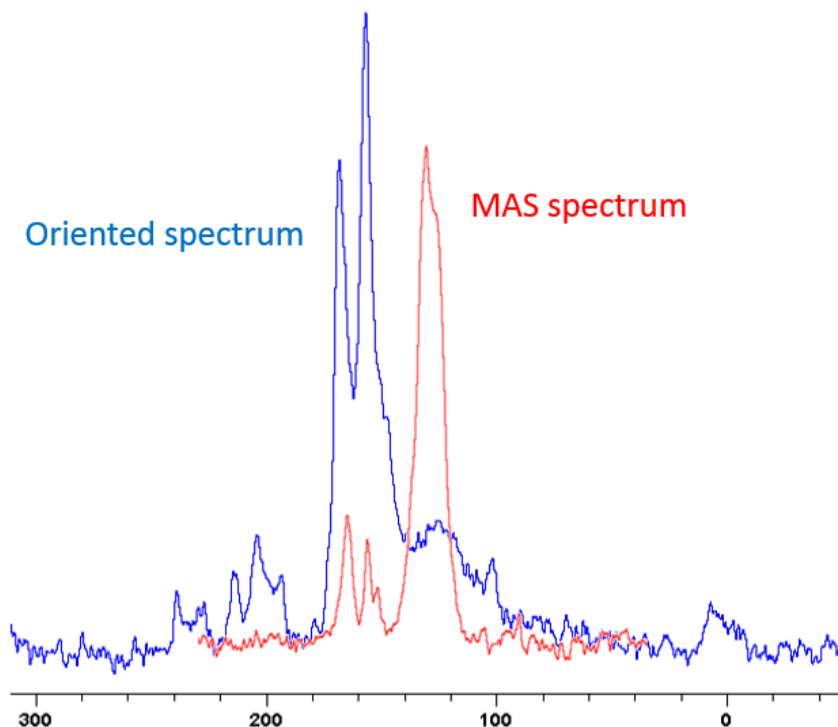


Figure 5.16. ^{13}C NMR spectra of 1000 g/mol LCT precursor. Isotropic CP/MAS (red) Oriented 250°C (blue).

5.3.2.1 Chemical Shift Anisotropy in Liquid Crystals

Here, we show ^{13}C NMR spectra of several small molecule liquid crystals to demonstrate the chemical shift changes between isotropic and nematic phases. The first example, terephthalylidene-bis-(4-n-butylaniline) (TBBA) is a well-studied liquid crystal that forms a nematic phase and several smectic phases. This molecule was used to calibrate the temperature, and optimize the experiment. The CSA is demonstrated as TBBA cools into the nematic and smectic phases in the ^{13}C spectra in Figure 5.17.

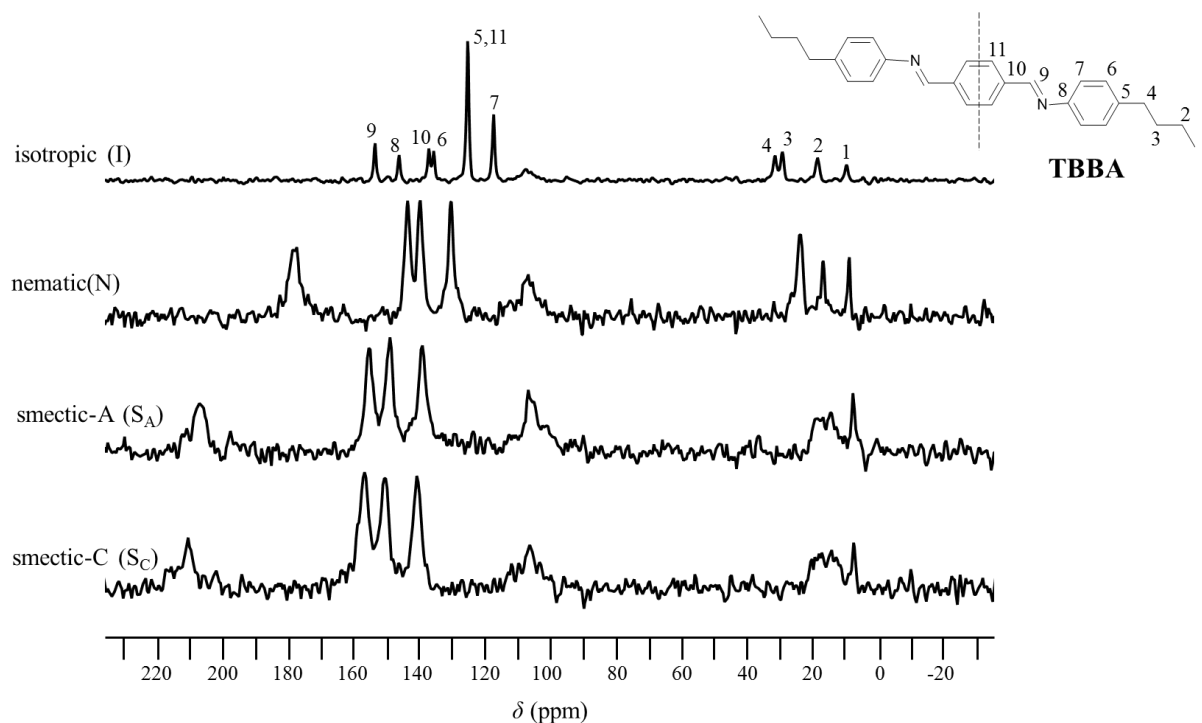


Figure 5.17. ^1H decoupled ^{13}C spectra of TBBA in the isotropic phase and various oriented phases.

Going from the isotropic phase into the oriented phases peaks move around because of the CSA. The isotropic spectrum shows a single peak for each chemically inequivalent carbon because the ^1H - ^{13}C J-coupling is removed by the decoupling pulse sequence (Figure 5.6). The carbon peaks are identified in the isotropic spectrum; the unidentified peak comes from a polytetrafluoroethylene (PTFE) plug that was used to hold the sample in place in the probe. The chemical shift anisotropy quantifies the deviation from the isotropic chemical shift which averages over all orientations. Because the aliphatic part of TBBA have very small CSA, those chemical shifts (carbons 1,2,3, and 4) do not move much upon cooling into the nematic phase. The aromatic peaks shift downfield upon cooling into the nematic phase. The peaks move further away from the isotropic values upon cooling into the two smectic phases.

There are several sophisticated pulse sequences for ^1H decoupling that are used to observe liquid crystal phases. They differ in the way the ^1H pulse occurs during the ^{13}C acquisition time in Figure 5.6. Three of these decoupling sequences are shown in Figure 5.18; continuous wave (CW), SPINAL-64, and WALTZ-16. It is clear from looking at nematic spectra of TBBA that the difference between the decoupling sequences is minimal so the CW pulse sequence is used, which is simply a continuous *rf* pulse at the ^1H Larmor frequency. It should be noted that the other two decoupling sequences require a knowledge of the 90° pulse width or the time required to torque the equilibrium Boltzmann distribution magnetization from the *z*-axis (parallel to the magnetic field; equilibrium position) into the *xy* plane. If the 90° pulse is not precise then the WALTZ-16 and SPINAL-64 schemes may not be as effective.

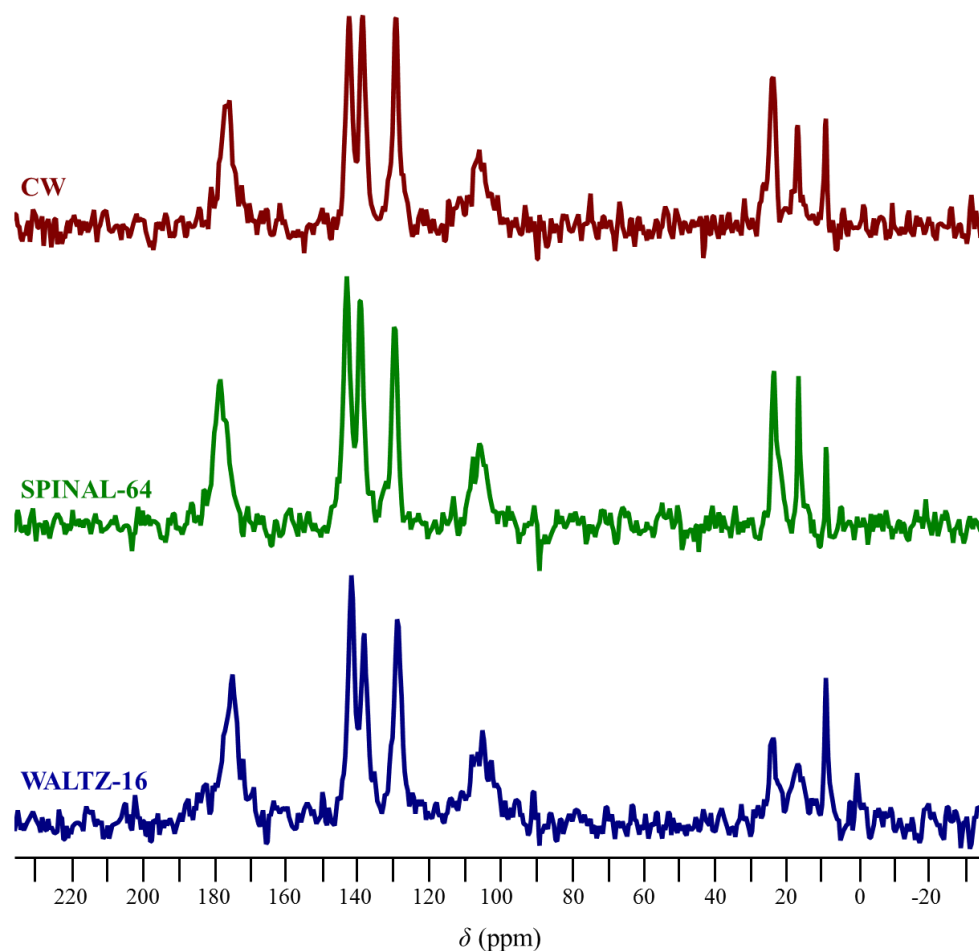


Figure 5.18. ^1H decoupled ^{13}C spectra of TBBA in the nematic phase using different ^1H decoupling schemes.

The popular small molecule liquid crystal, 5-CB, used in many liquid crystal displays has been extensively studied and its CSA is well-documented. The nematic and isotropic spectra of 5-CB are shown in Figure 5.19 from an article in the *Encyclopedia of NMR*.⁷⁹ All peaks are identified and we use this information to look at other liquid crystal molecules and the LCT oligomer.

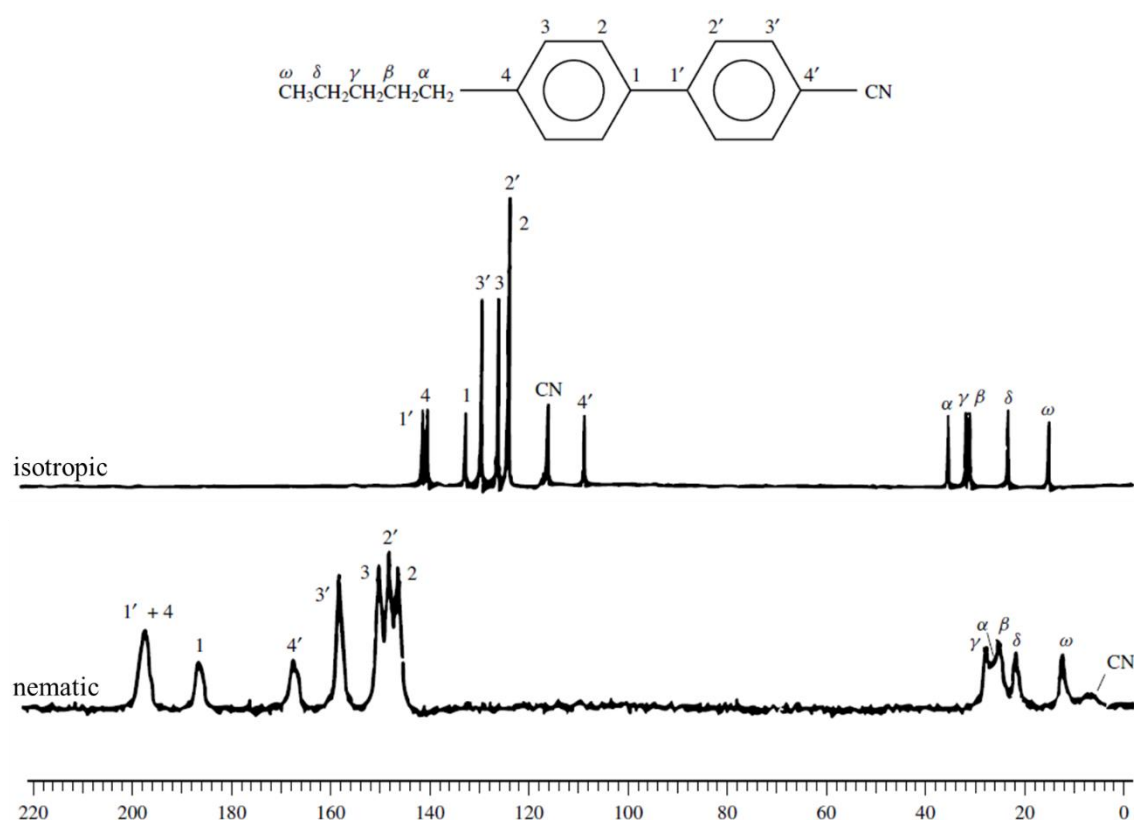


Figure 5.19. Proton-decoupling ^{13}C NMR of 5-CB in the isotropic and nematic phases. From ref 79.

One important item to note from the spectra of 5-CB are that the $-\text{CN}$ group appears to have a very large CSA and is shifted by ~ 100 ppm downfield. This is important because the chemical group of interest in the LCT oligomer is the acetylene carbons, which has similar electronic distribution to $-\text{CN}$, which determines the CSA. Conceptually a large CSA means that the carbon nuclei in $-\text{CN}$ “see” a very different magnetic field depending on how the molecule is oriented with respect to the field, which is related to how the electrons “shield” the nucleus from the external field.

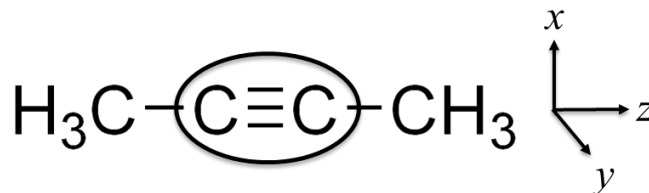


Figure 5.20. Dimethylacetylene structure and axes system with the z -axis along the acetylene bond.

In order to explicitly anticipate the CSA of the acetylene groups, we can look at a simple molecule: dimethylacetylene (structure and axes system in Figure 5.20), which has well-defined chemical shift tensor values where $\sigma_{zz} = -44$; $\sigma_{xx} = \sigma_{yy} = 157$.¹⁰⁸ The observed chemical shift is the sum of the isotropic chemical shift and the anisotropic chemical shift; the isotropic chemical shift and anisotropic chemical shift are defined in Equation 5.2. Equation 5.2 indicates that the observed chemical shift for acetylene carbons will be shifted 100 ppm upfield from the isotropic chemical shift value assuming an order parameter S_{zz} of 0.5, a typical value for liquid crystals.

$$\delta^{obs} = \delta^{iso} + \delta^{aniso}$$

$$\delta_{C\equiv C}^{iso} = \frac{1}{3}(\sigma_{xx} + \sigma_{yy} + \sigma_{zz}) = \frac{1}{3}(157 + 157 - 44) = 90 \text{ ppm} \quad (5.2)$$

$$\delta_{C\equiv C}^{aniso} = S_{zz} \left(\sigma_{zz} - \frac{1}{2}(\sigma_{xx} + \sigma_{yy}) \right) \cong 0.5(-44 - 157) \cong -100 \text{ ppm}$$

Lastly, we look at the molecule pentyloxy-substituted diphenyl diacetylene (DPDA-OC₅)¹⁰⁹ because it contains the key chemical groups present in the LCT precursor (aliphatic carbons, aromatic carbons, and acetylene carbons). The acetylene carbons are shifted upfield significantly, while the aliphatic carbons do not move, and the aromatic carbons are shifted downfield slightly.⁷⁹ Since we are tracking the curing chemistry of the reactive groups (phenylethynyl groups) it was important to realize that these would be shifted to very low

chemical shift values in the nematic phase making them easy to monitor with ^{13}C NMR. By performing the calculation for dimethylacetylene, we concluded that the resonances around $\delta = 0$ ppm (blue spectrum, Figure 5.21) represents the acetylene carbons in DPDA-OC₅ and in the LCT oligomer (blue spectrum, Figure 5.16).

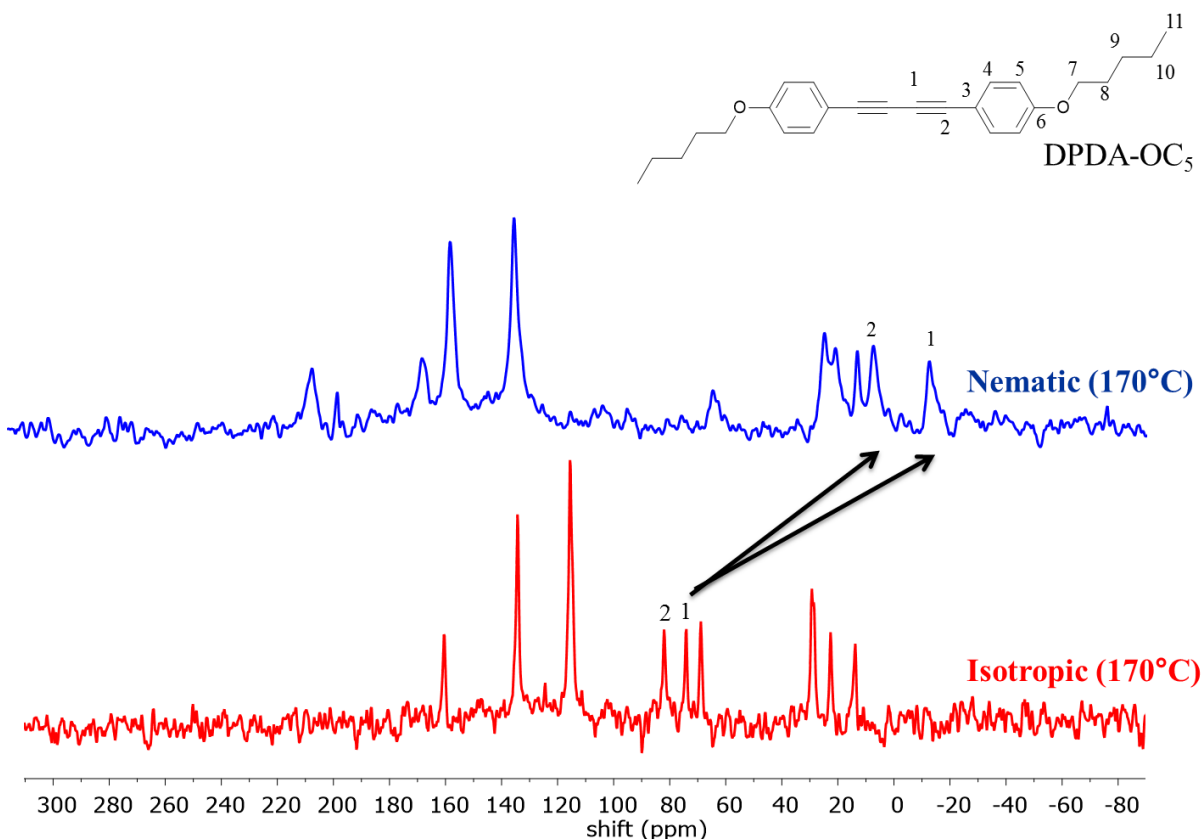


Figure 5.21. ^{13}C spectra of DPDA-OC₅ in the nematic and isotropic phases.

5.3.3. Exploitation of Chemical Shift Anisotropy in LCTs

With our high temperature set-up (Figure 5.7) we can see the qualitative disappearance of the ethynyl carbon peak around 0 ppm when the LCT precursor is cured at 300°C for 1 hour (Figure 5.22). However, the peak is on the edge of the resolution required to draw any quantitative conclusions about the curing reaction. This is a significant drawback of studying the LCT precursor. Because of the presence of variation in molecular

weight between oligomers, the ^{13}C spectrum is effectively broadened because the ordering of each oligomer with respect to the magnetic field is slightly different leading to different CSA values. Additionally, the concentration of reactive end-group is fairly small compared to the rest of the oligomer chain.

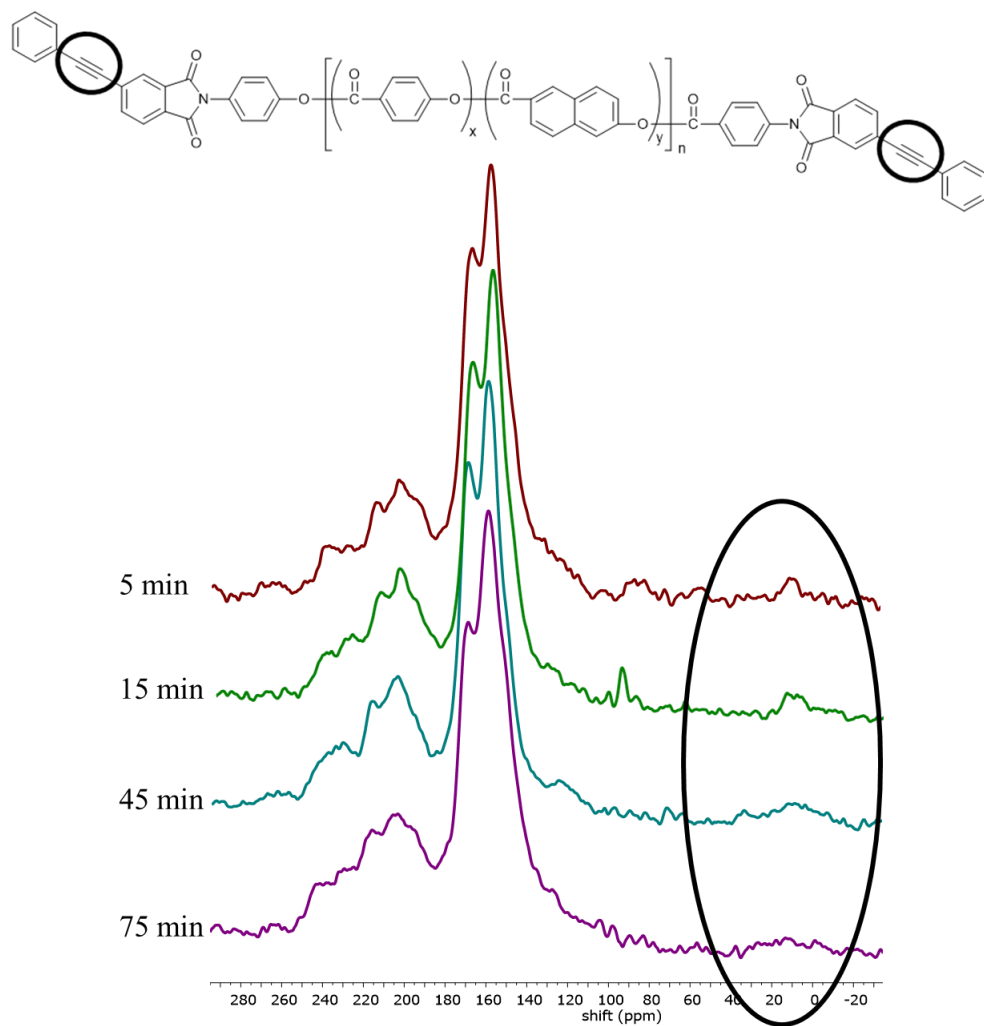


Figure 5.22. ^{13}C NMR of LCT after curing at 300°C for 75 min for various time intervals. A qualitative loss of the ethynyl carbon peak intensity is observed.

5.3.3.1 LCT Model Compounds

To obtain quantitative kinetic measurements we instead turn to a liquid crystalline model compound with the same phenylethynyl reactive end-group. The structure of the

model compound, PE-naphthalenediol-PE (PE=phenylethynyl), is shown in Figure 5.23 with the ethynyl resonance circled. The ^{13}C resonances are better resolved due to the well-defined structure with no variation in molecular weight. Additionally, the signal is more intense because of the higher concentration of ethynyl groups making the kinetic study straightforward.

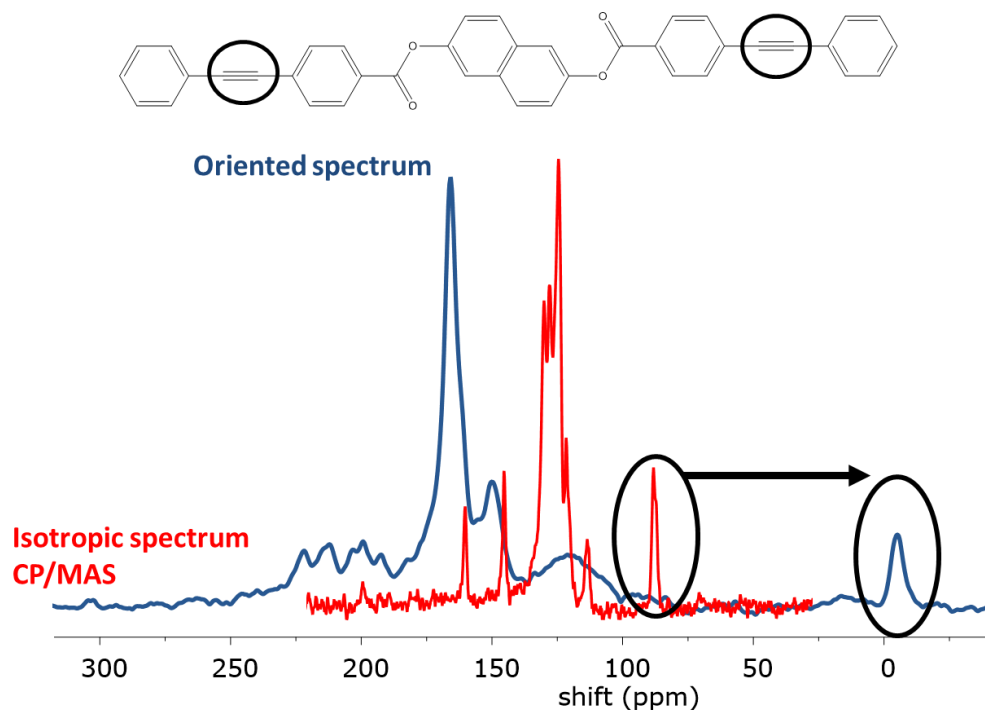


Figure 5.23. CP/MAS (isotropic) spectrum in red and oriented (anisotropic) spectrum in blue of the PE-naphthalenediol-PE model compound. The anisotropic shift is indicated with an arrow and the ethynyl group for kinetic studies is circled in both the structure and spectra.

5.3.2 Curing Kinetics

In the nematic melt, the director spontaneously aligns along the spectrometer magnetic field identifying the reactive acetylene group by its distinct chemical shift anisotropy (CSA). The disappearance of the acetylene resonance indicates the formation of cure products with phenylethynyl end-groups. By integrating NMR peaks at time points during cure, we can plot the concentration of ethynyl groups against time to obtain kinetic

plots. NMR spectra taken at specified curing temperatures show that the curing chemistry follows first-order rate kinetics with rate constants of 0.011 min^{-1} and 0.023 min^{-1} at 300°C and 325°C , respectively. First-order rate constants were obtained from linear fits of plots of the natural log of concentration vs. time. Figure 5.24 shows some spectra taken during cure at 300°C along with the plot of concentration of reactive end-groups against cure time and Figure 5.25 shows the kinetic plots with the rate constants calculated from fits to the data.

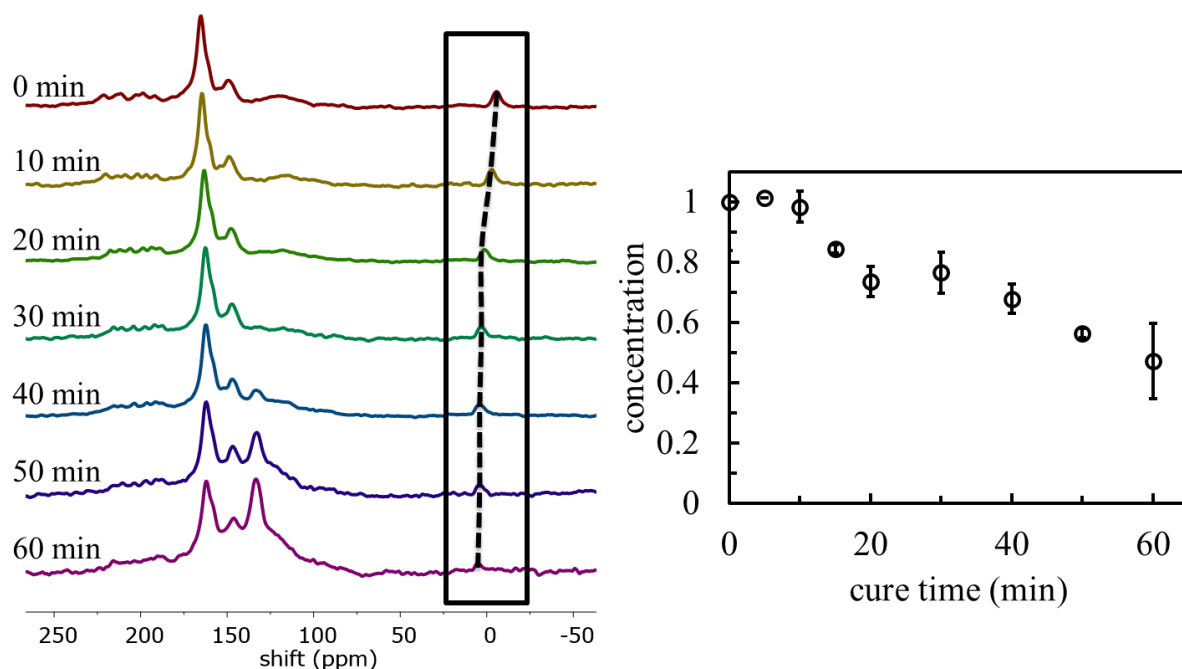


Figure 5.24. ^{13}C NMR of LCT precursor model compound (PE-naphthalenediol-PE). Different durations of curing in minutes at 300°C and plot of concentration of ethynyl peak vs. cure time used to determine kinetic rate constants.

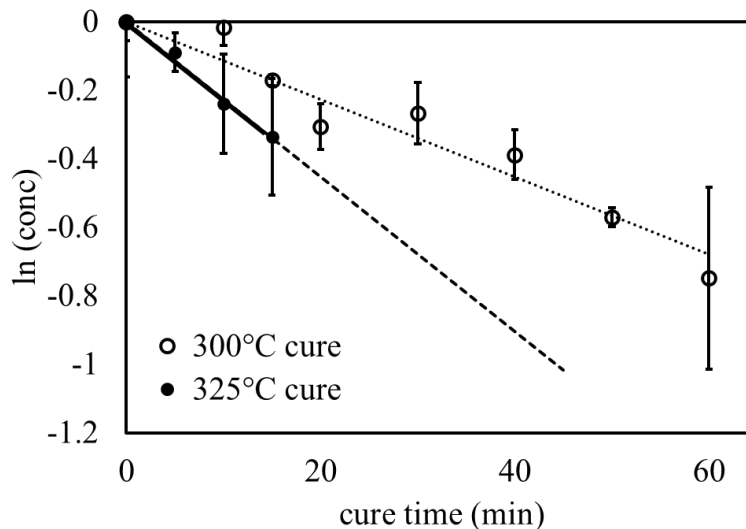


Figure 5.25. Kinetic plot of the natural log of concentration vs. cure time in minutes. First-order rate constants are found from linear fits to the data.

In addition to kinetic information, the NMR technique also gives information about the supramolecular structure of LCT as it cures because the CSA can be related to orientational order. The chemical shift of the ethynyl resonance shifts towards the isotropic value (dashed line in Figure 5.24) during the curing process which indicates a decrease in orientational order as the network is formed. Using Equation 5.2, the order parameter of PE-naphthalenediol-PE before and after curing can be calculated from the observed chemical shifts (-5 ppm before cure and +6 ppm after curing for 60 min at 300°C) and the isotropic chemical shift (88 ppm) in Equation 5.3. The order parameter drops from 0.46 to 0.41 upon curing for 60 min at 300°C. The acetylene peak also broadens upon curing which indicates a gradient of order parameters upon curing, which is consistent with the formation of a three-dimensional network.

$$S_{zz} = \frac{\delta^{aniso}}{\sigma_{zz}^{C\equiv C} - \sigma_{yy}^{C\equiv C}} \quad (5.3)$$

5.4 Conclusions

Since the overall properties of a thermoset resin is dictated by the structure of the crosslinks formed, it is important to understand the resin curing chemistry. However, cured resins are difficult to characterize because of their insoluble nature. We have developed a way to investigate the curing chemistry of LCT with fewer scans than with CP/MAS and without the expensive process of ^{13}C labeling.

Mechanical properties of cured LCTs suggest that chain extension, in addition to cross-linking, most likely plays a major role in the curing of phenylethynyl-based systems. In order to understand this process completely we examined the kinetics of the disappearance of the reactive group (at 0 ppm), which is readily resolved from the rest of the spectrum of a phenylethynyl end-capped model compound.

APPENDIX A: TABLES OF ^2H AND ^{13}C NMR DATA OF CYANOBIPHENYL DIMERS

The ^2H NMR quadrupolar splittings of decane- d_{22} dissolved in cyanobiphenyl dimers summarized in Section 3.3.2 is displayed in the tables below. The splittings of methyl (“C1”) and all methylene deuterons are numbered from 2-5 starting with the methylene adjacent to C1. Because of the symmetry of decane- d_{22} , only the first five groups are shown.

2 wt% decane- d_{22} in CB-C11-CB				T_{NI} (obs)	392
T (K)	T_{red}	C1 (Hz)	C2 (Hz)		
391.8	0.999	4201	14066		
390.6	0.996	5104	17196		
386	0.985	6572	21973		
383.7	0.979	7048	23500		
382.5	0.976	7258	24182		
381.3	0.973	7435	24766		
380.2	0.97	7611	25201		
379	0.967	7706	25543		
377.8	0.964	7788	25883		
376.7	0.961	7851	25948		
375.5	0.958	7894	26092		
374.3	0.955	7979	26333		
373.2	0.952	8072	26707		
372	0.949	8180	26706		
370.8	0.946	8230	27031		
368.5	0.94	8411			

2 wt% decane-d ₂₂ in CB-C9-CB				T_{NI} (obs)	389		
T (K)	T _{red}	C1 (Hz)	C2 (Hz)	C2b (Hz)	C3 (Hz)	C4 (Hz)	C5 (Hz)
388	0.9974	4579.74	15546.93		18484.25	19740.57	
386	0.9923	5328.61	17895.14		20852.82	22670.15	
384	0.9871	5843.07	19550.39		22870.06	24473.4	24976.87
382	0.982	6222.18	20785.15		24210.77	25999.56	26469.93
380	0.9769	6534.46	21746.34		25345.54	27252.08	27791.56
378	0.9717	6794.29	22540.24		26257.45	28139.07	28663.66
376	0.9666	7063.16	23215.23	23479.29	27179.66	29198.83	
374	0.9614	7291.73	23758.17	24150.2	28004.42	29958.76	30514.98
372	0.9563	7530.43	24446.45	24946.89	28776.17	30762.83	31289.67
370	0.9512	7699.14	24804.76	25574.84	29367.26	31511.03	31922.66
368	0.946	7900.5	25301.77	26214.09	30076.41	32058.59	32517.94
366	0.9409	8045.33	25572.82	26604.04	30446.38	32667.24	33000.88
365	0.9383	8128.02	26124.36	26960.19			
364	0.9357	8231.5	26259.47	27352.38	31141.04	33291.6	34040.26
362	0.9306	8324.58	26662.85	27675.04			
360	0.9254	8503.4	27390.67	28531.44			
358	0.9203	8627.68	27501.6	28803.54			
356	0.9152	8823.61					

2 wt% decane-d ₂₂ in CB-C7-CB				T_{NI} (obs)	385		
T (K)	T _{red}	C1 (Hz)	C2 (Hz)	C2b (Hz)	C3 (Hz)	C4 (Hz)	C5 (Hz)
384	0.9974	3180.7					
382	0.9922	4412.12	14920.83		17764.68	18596.14	
380	0.987	5052.44	16984.18		19986.4	21186.82	
378	0.9818	5479.71	18300.36		21320.53	23003.32	
376	0.9766	5805.79	19490.59		23413.77	24193.76	24599.86
375	0.974	5822.76	19426.64		22672.51	24326.82	
374	0.9714	5982.55	20034.43		23312.36	25028.48	
372	0.9662	6794.01	22584.05		26074.21	28118.61	
370	0.961	7085.6	22999.47	23854.03	27416.37	29189.24	
368	0.9558	7311.79	23628.76	24595.34	28175.91	30066.31	
366	0.9506	7528.15	24176.87	25271.84	28879.47	30931.18	
364	0.9455	7725.35	24705.98	25939.61	29073.13	31469.81	
362	0.9403	7871.67	25144.86	26365.09	29791.06	32019.22	
362	0.9403	7784.17	24958.5	26108.48	29767.5	31754.51	
360	0.9351	7962.5	25868.28	26924.4	30479.22	32239.28	
358	0.9299	8125.02	25772.28	27363.5	31077.69	32793.42	
356	0.9247	8241.89	25459.49	27117.84	31243.67	33476.35	
354	0.9195	8445.74	26628.47	28049.46	31621.89	33277.44	34091.95
352	0.9143	8555.4	26831.47	28590.38	32354.64	33979.43	34528.83
350	0.9091	8696.77	26755.16	29298.12	32031.41	34863.05	
348	0.9039	8837.28					

2 wt% decane-d ₂₂ in CB-C10-CB				T_{NI} (obs)	425	
T (K)	T _{red}	C1 (Hz)	C2 (Hz)	C3 (Hz)	C4 (Hz)	C5 (Hz)
420	0.98824	13694.1	45126.3	52243.3	56081.2	57080.9
415	0.97647	14463.2	47542.1	55075.1	58687.4	59508.2
410	0.96471	15147.3	49433.8	57265.5	60844.3	61737.9
405	0.95294	15827.9	51322.1	58759.6	63113.7	63910.9
400	0.94118	16380.5	52620	60411.7	64418.4	64920.9

2 wt% decane-d ₂₂ in 5CB				T_{NI} (obs)	305	
T (K)	T _{red}	C1 (Hz)	C2 (Hz)	C3 (Hz)	C4 (Hz)	C5 (Hz)
296.6	0.97246	7411.49	24318.5	28588.8	30977.1	31737.5
298	0.97705	7087.32	23255.7	27375.3	29560.3	30498
299	0.98033	6785.75	22292.3	26248.4	28372.1	29221.1
300	0.98361	6489.09	21338.8	25116.5	27178.6	27983.6
301	0.98689	6110.42	20017.5	23580.7	25740.9	26082.4
302	0.99016	5689.61	18695.6	22004.7	24016.7	24483.3
303	0.99344	5084.33	16787	19779.1	21423.3	22034.3
304	0.99672	4326.71	14191	16755.1		18518.2

The ¹³C NMR chemical shift data for cyanobiphenyl dimers summarized in Section 3.3.7 is displayed in the tables below. The observed (δ_{CN}^{obs}), isotropic (δ_{CN}^{iso}), and anisotropic (δ_{CN}^{aniso}) chemical shift values are displayed as well as the order parameter calculated from Equation 3.8 in the text. For CB-C10-CB, values for the aromatic carbon (4') resonance is given as opposed to CN for reasons given in the text.

CB-C11-CB		T_{Nl} (obs)	393.5		
T (K)	T _{red}	$\delta_{\text{CN}}^{\text{obs}}$	$\delta_{\text{CN}}^{\text{iso}}$	$\delta_{\text{CN}}^{\text{aniso}}$	S _{CN}
393	0.9987	35.16	111.96	-76.8	0.3397
392	0.9962	29.69	111.96	-82.27	0.3687
391	0.9936	26.7	111.96	-85.26	0.3845
390	0.9911	22.88	111.96	-89.08	0.4048
388	0.986	19.2	111.96	-92.76	0.4243
386	0.9809	16.43	111.96	-95.53	0.439
384	0.9759	14.45	111.96	-97.51	0.4494
382	0.9708	13.3	111.96	-98.66	0.4555
380	0.9657	13.31	111.96	-98.65	0.4555
379	0.9632	14.02	111.96	-97.94	0.4517
378	0.9606	15.91	111.96	-96.05	0.4417
377	0.9581	16.97	111.96	-94.99	0.4361
376	0.9555	18.08	111.96	-93.88	0.4302
375	0.953	19.2	111.96	-92.76	0.4243
374	0.9504	19.27	111.96	-92.69	0.4239
373	0.9479	20.48	111.96	-91.48	0.41749
372	0.94536	20.67	111.96	-91.29	0.41648
371	0.94282	21.38	111.96	-90.58	0.41272
370	0.94028	21.02	111.96	-90.94	0.41463

CB-C9-CB		T_{NI} (obs)	391		
T (K)	T _{red}	$\delta_{\text{CN}}^{\text{obs}}$	$\delta_{\text{CN}}^{\text{iso}}$	$\delta_{\text{CN}}^{\text{aniso}}$	S _{CN}
390	0.9974	42.7	112.25	-69.6	0.3013
388	0.9923	35.74	112.25	-76.5	0.3382
386	0.9872	32.01	112.25	-80.2	0.3579
384	0.9821	28.88	112.25	-83.4	0.3745
382	0.977	27.61	112.25	-84.6	0.3812
380	0.9719	26.72	112.25	-85.5	0.386
378	0.9668	26.43	112.25	-85.8	0.3875
376	0.9616	26.88	112.25	-85.4	0.3851
375	0.9591	27.14	112.25	-85.1	0.3837
374	0.9565	27.4	112.25	-84.9	0.3824
373	0.954	27.78	112.25	-84.5	0.3803
372	0.9514	27.81	112.25	-84.4	0.3802
371	0.9488	27.9	112.25	-84.4	0.3797
370	0.9463	28.12	112.25	-84.1	0.3785
369	0.9437	28.82	112.25	-83.4	0.3748
368	0.9412	28.29	112.25	-84	0.3776
366	0.9361	29.12	112.25	-83.1	0.3732
364	0.9309	29.16	112.25	-83.1	0.373
362	0.9258	29.77	112.25	-82.5	0.3698
360	0.9207	30.73	112.25	-81.5	0.3647
358	0.9156	30.76	112.25	-81.5	0.3645
356	0.9105	30.2	112.25	-82.1	0.3675
354	0.9054	30.45	112.25	-81.8	0.3662
352	0.9003	31.14	112.25	-81.1	0.3625
350	0.8951	30.84	112.25	-81.4	0.3641

CB-C7-CB		T_{NI} (obs)	388		
T (K)	T _{red}	$\delta_{\text{CN}}^{\text{obs}}$	$\delta_{\text{CN}}^{\text{iso}}$	$\delta_{\text{CN}}^{\text{aniso}}$	S _{CN}
386	0.9948	56.83	112.04	-55.21	0.2253
384	0.9897	46.85	112.04	-65.19	0.2782
382	0.9845	42.17	112.04	-69.87	0.303
380	0.9794	39.07	112.04	-72.97	0.3194
379	0.9768	37.96	112.04	-74.08	0.3253
378	0.9742	37.13	112.04	-74.91	0.3297
377	0.9716	36.32	112.04	-75.72	0.334
376	0.9691	35.59	112.04	-76.45	0.3378
375	0.9665	33.2	112.04	-78.84	0.3505
374	0.9639	33.04	112.04	-79	0.3514
373	0.9613	32.83	112.04	-79.21	0.3525
372	0.9588	32.86	112.04	-79.18	0.3523
370	0.9536	33.01	112.04	-79.03	0.3515
368	0.9485	32.65	112.04	-79.39	0.3534
366	0.9433	33.04	112.04	-79	0.3514
364	0.9381	33.17	112.04	-78.87	0.3507
360	0.9278	34.18	112.04	-77.86	0.3453
358	0.9227	34.23	112.04	-77.81	0.345
356	0.9175	34.99	112.04	-77.05	0.341

CB-C10-CB		T_{NI} (obs)	442		
T (K)	T _{red}	$\delta_{4'}^{\text{obs}}$	$\delta_{4'}^{\text{iso}}$	$\delta_{4'}^{\text{aniso}}$	S _{4'}
420	0.9502	184.31	104	80.31	0.8243
418	0.9457	184.99	104	80.99	0.8316
416	0.9412	185.64	104	81.64	0.8386
414	0.9367	185.8	104	81.8	0.8403
412	0.9321	186.28	104	82.28	0.8455
410	0.9276	186.88	104	82.88	0.852
406	0.9186	187.31	104	83.31	0.8566
402	0.9095	187.72	104	83.72	0.8611
398	0.9005	188.41	104	84.41	0.8685

5-CB		T_{NI} (obs)	305		
T (K)	T _{red}	$\delta_{\text{CN}}^{\text{obs}}$	$\delta_{\text{CN}}^{\text{iso}}$	$\delta_{\text{CN}}^{\text{aniso}}$	S _{CN}
297	0.9738	5.02	112.01	-106.99	0.4997
298	0.977	7.86	112.01	-104.15	0.4846
299	0.9803	10.81	112.01	-101.2	0.469
300	0.9836	13.86	112.01	-98.15	0.4528
301	0.9869	18.65	112.01	-93.36	0.4275
302	0.9902	22.71	112.01	-89.3	0.4059
303	0.9934	29.56	112.01	-82.45	0.3696
304	0.9967	38.94	112.01	-73.07	0.3199

REFERENCES

- (1) Mirau, P. A. *A Practical Guide to Understanding the NMR of Polymers*; Wiley-Interscience, 2005.
- (2) Samulski, E. T. The Mesomorphic State. In *Physical Properties of Polymers*; Cambridge University Press: Cambridge, U.K., 2004; pp 316–380.
- (3) Levitt, M. H. *Spin Dynamics: Basics of Nuclear Magnetic Resonance*; Wiley, 2001.
- (4) Bovey, F. A.; Mirau, P. A. *NMR of Polymers*; Elsevier Science, 1996.
- (5) Bernal, J. D. The Bakerian Lecture, 1962. The Structure of Liquids. *Proc. R. Soc. Lond. A. Math. Phys. Sci.* **1964**, 280, pp. 299–322.
- (6) Rowlinson, J. S. *Liquids and Liquid Mixtures*; Modern aspects series of chemistry; Butterworths, 1959.
- (7) Gubbins, K. E.; Gray, C. G. Perturbation Theory for the Angular Pair Correlation Function in Molecular Fluids. *Molecular Physics*, 1972, 23, 187–191.
- (8) Hansen, J. P.; McDonald, I. R. *Theory of Simple Liquids*; Academic Press, 1986.
- (9) Barrat, J. L.; Hansen, J. P. *Basic Concepts for Simple and Complex Liquids*; Cambridge University Press: Cambridge, U.K., 2003.
- (10) Bernal, J. D. A Geometrical Approach to the Structure Of Liquids. *Nature*, 1959, 183, 141–147.
- (11) Allen, P.; Tildesley, D. J. *Computer Simulation of Liquids*; Oxford Science Publ; Clarendon Press: New York, 1989.
- (12) Frenkel, D.; Smit, B. *Understanding Molecular Simulation: From Algorithms to Applications*; Academic Press: San Diego, C.A., 2002.
- (13) González, M. A. Force Fields and Molecular Dynamics Simulations. *École thématique la Société Française la Neutron*. **2011**, 12, 169–200.

- (14) Allinger, N. L.; Yuh, Y. H.; Lii, J. H. Molecular Mechanics. The MM3 Force Field for Hydrocarbons. 1. *J. Am. Chem. Soc.* **1989**, *111*, 8551–8566.
- (15) Smith, G. D.; Jaffe, R. L. Comparative Study of Force Fields for Benzene. *J. Phys. Chem.* **1996**, *100*, 9624–9630.
- (16) Fu, C.-F.; Tian, S. X. A Comparative Study for Molecular Dynamics Simulations of Liquid Benzene. *J. Chem. Theory Comput.* **2011**, *7*, 2240–2252.
- (17) Rapaport, D. C. *The Art of Molecular Dynamics Simulation*; Cambridge University Press, 2004.
- (18) Council, N. R. *High Magnetic Field Science and Its Application in the United States: Current Status and Future Directions*; The National Academies Press: Washington, DC, 2013.
- (19) Lohman, J. A. B.; Maclean, C. Alignment Effects on High Resolution NMR Spectra, Induced by the Magnetic Field. *Chem. Phys.* **1978**, *35*, 269–274.
- (20) Lohman, J. A. B.; Maclean, C. Magnetic Field Induced Alignment Effects in ²H NMR Spectra. *Chem. Phys. Lett.* **1978**, *58*, 483–486.
- (21) Van Zijl, P. C. M.; Ruessink, B. H.; Bulthuis, J.; MacLean, C. NMR of Partially Aligned Liquids: Magnetic Susceptibility Anisotropies and Dielectric Properties. *Acc. Chem. Res.* **1984**, *17*, 172–180.
- (22) Gayathri, C.; Bothner-By, A. A.; Van Zijl, P. C. M.; Maclean, C. Dipolar Magnetic Field Effects in NMR Spectra of Liquids. *Chem. Phys. Lett.* **1982**, *87*, 192–196.
- (23) Lohman, J. A. .; MacLean, C. The Determination of Magnetic Susceptibility Anisotropies from Quadrupolar Interactions in NMR. *J. Magn. Reson.* **1981**, *42*, 5–13.
- (24) Heist, L. M.; Poon, C.-D.; Samulski, E. T.; Photinos, D. J.; Jokisaari, J.; Vaara, J.; Emsley, J. W.; Mamone, S.; Lelli, M. Benzene at 1GHz. Magnetic Field-Induced Fine Structure. *J. Magn. Reson.* **2015**, *258*, 17–24.
- (25) Oldani, M.; Bauder, A. Pure Rotational Spectrum of Benzene-d₁. *Chemical Physics Letters*, 1984, *108*, 7–10.

- (26) Jans-Bürli, S.; Oldani, M.; Bauder, A. Deuterium Quadrupole Coupling in Rotational Spectra of Benzene-D 1 and of Three Isomers of Fluorobenzene-D 1. *Mol. Phys.* **1989**, 68, 1111–1123.
- (27) Bailey, W. C. B3LYP Calculation of Quadrupole Coupling Constants in Molecules. *Chemical Physics Letters*, 1998, 292, 71–74.
- (28) Gray, C. G.; Gubbins, K. E. *Theory of Molecular Fluids: Fundamentals*; International series of monographs on chemistry; Clarendon Press, Oxford University Press: New York, 1984.
- (29) Bothner-By, A. A.; Dadok, J.; Mishra, P. K.; Van Zijl, P. C. M. High-Field NMR Determination of Magnetic Susceptibility Tensors and Angular Correlation Factors of Halomethanes. *J. Am. Chem. Soc.* **1987**, 109, 4180–4184.
- (30) Van Zijl, P. C. M.; Maclean, C.; Bothner-By, A. A. Angular Correlation and Diamagnetic Susceptibilities Studied by High Field NMR. *J. Chem. Phys.* **1985**, 83, 4410–4417.
- (31) Van Zijl, P. C. M.; Maclean, C.; Bothner-By, A. A. Angular Correlation and Diamagnetic Susceptibilities Studied by High Field NMR. II. Halobenzenes, Pyridine, and Aniline. *J. Chem. Phys.* **1985**, 83, 4978.
- (32) Bastiaan, E. W.; Maclean, C. Molecular Orientation in High-Field High-Resolution NMR. In *NMR at Very High Field*; Robert, J. B., Ed.; Springer-Verlag: Berlin, 1991; pp 17–43.
- (33) Pyykkö, P.; Elmi, F. Deuteron Quadrupole Coupling in Benzene: Librational Corrections Using a Temperature-Dependent Einstein Model, and Summary. The Symmetries of Electric Field Gradients and Conditions for $\eta = 1$. *Phys. Chem. Chem. Phys.* **2008**, 10, 3867–3871.
- (34) Kantola, A. M.; Ahola, S.; Vaara, J.; Saunavaara, J.; Jokisaari, J. Experimental and Quantum-Chemical Determination of the (2)H Quadrupole Coupling Tensor in Deuterated Benzenes. *Phys. Chem. Chem. Phys.* **2007**, 9, 481–490.
- (35) Jokisaari, J.; Hiltunen, Y. Deuteron Quadrupole Coupling Constants of Methyl Iodide and Chloroform Determined by NMR in Liquid-Crystalline Phases. *J. Magn. Reson.* **1984**, 60, 307–319.

- (36) Samulski, E. T.; Poon, C.-D.; Heist, L. M.; Photinos, D. J. Liquid-State Structure via Very High-Field Nuclear Magnetic Resonance Discriminates among Force Fields. *J. Phys. Chem. Lett.* **2015**, 3626–3631.
- (37) Lubricants, A. C. D.-2 on P. P. and. *Physical Constants of Hydrocarbons C1 to C10*; ASTM STP 109A; American Society for Testing & Materials, 1963.
- (38) Ren, P.; Wu, C.; Ponder, J. W. Polarizable Atomic Multipole-Based Molecular Mechanics for Organic Molecules. *J. Chem. Theory Comput.* **2011**, 7, 3143–3161.
- (39) Dang, L. X. Molecular Dynamics Study of Benzene–benzene and Benzene–potassium Ion Interactions Using Polarizable Potential Models. *J. Chem. Phys.* **2000**, 113, 266.
- (40) Kaminski, G. A.; Friesner, R. A.; Tirado-Rives, J.; Jorgensen, W. L. Evaluation and Reparametrization of the OPLS-AA Force Field for Proteins via Comparison with Accurate Quantum Chemical Calculations on Peptides †. *J. Phys. Chem. B* **2001**, 105, 6474–6487.
- (41) MacKerell, A. D.; Bashford, D.; Bellott, M.; Dunbrack, R. L.; Evanseck, J. D.; Field, M. J.; Fischer, S.; Gao, J.; Guo, H.; Ha, S.; et al. All-Atom Empirical Potential for Molecular Modeling and Dynamics Studies of Proteins. *J. Phys. Chem. B* **1998**, 102, 3586–3616.
- (42) Patrick, C. R.; Prosser, G. S. A Molecular Complex of Benzene and Hexafluorobenzene. *Nature* **1960**, 187, 1021–1021.
- (43) Williams, J. H. The Molecular Electric Quadrupole Moment and Solid-State Architecture. *Acc. Chem. Res.* **1993**, 26, 593–598.
- (44) Battaglia, M. R.; Buckingham, A. D.; Williams, J. H. The Electric Quadrupole-Moments of Benzene and Hexafluorobenzene. *Chem. Phys. Lett.* **1981**, 78, 420–423.
- (45) Reeves, L.; Schneider, W. Nuclear Magnetic Resonance Measurements of Complexes of Chloroform with Aromatic Molecules and Olefins. *Can. J. Chem.* **1957**.
- (46) Huntress Jr., W. A Nuclear Magnetic Resonance Study of Anisotropic Molecular Rotation in Liquid Chloroform and in Chloroform-Benzene Solution. **1969**, 79.
- (47) Rothschild, W. G. Solvation by Benzene: Molecular Dynamics Simulation of

Orientational Motion, Translational Diffusion, and Site–site Radial Distributions of the Solutes Di- and Trichloromethane (chloroform). *Mol. Phys.* **2007**, *105*, 1003–1011.

- (48) Rothschild, W. G. On Complex Formation in Equimolar Chloroform–benzene Solution: A Revisit by Molecular Dynamics Simulation and Orientational Correlation States Superposition. *J. Mol. Liq.* **2009**, *150*, 68–72.
- (49) Misawa, M.; Fukunaga, T. Structure of Liquid Benzene and Naphthalene Studied by Pulsed Neutron Total Scattering. *J. Chem. Phys.* **1990**, *93*, 3495.
- (50) Narten, a. H. X-Ray Diffraction Pattern and Models of Liquid Benzene. *J. Chem. Phys.* **1977**, *67*, 2102.
- (51) Kumar, S. *Liquid Crystals: Experimental Study of Physical Properties and Phase Transitions*; Cambridge University Press, 2001.
- (52) Vorländer, D. Die Richtung Der Kohlenstoff-Valenzen in Benzol-Abkömmlingen. *Berichte der Dtsch. Chem. Gesellschaft B* **1929**, *62*, 2831–2835.
- (53) Madsen, L. A.; Dingemans, T. J.; Nakata, M.; Samulski, E. T. Thermotropic Biaxial Nematic Liquid Crystals. *Phys. Rev. Lett.* **2004**, *92*, 145505–1.
- (54) Kimura, T.; Toriumi, H.; Watanabe, H. Mesomorphic Properties of Dimer Liquid Crystals: Low Molecular-Weight Analogues of Nematic Polymers. In *MACRO 88*; Kyoto, Japan, 1988.
- (55) Toriumi, H. *Manuscript Submitted to Liquid Crystals in 1991*.
- (56) Photinos, D. J.; Samulski, E. T.; Toriumi, H. Molecular Flexibility in Nematics: From Alkanes to Dimer Mesogens. *Journal of the Chemical Society, Faraday Transactions*, 1992, *88*, 1875.
- (57) Cestari, M.; Diez-Berart, S.; Dunmur, D. A.; Ferrarini, A.; De La Fuente, M. R.; Jackson, D. J. B.; Lopez, D. O.; Luckhurst, G. R.; Perez-Jubindo, M. A.; Richardson, R. M.; et al. Phase Behavior and Properties of the Liquid-Crystal Dimer 1'',7''-bis(4-Cyanobiphenyl-4'-Yl) Heptane: A Twist-Bend Nematic Liquid Crystal. *Phys. Rev. E - Stat. Nonlinear, Soft Matter Phys.* **2011**, *84*.
- (58) Borshch, V.; Kim, Y.-K.; Xiang, J.; Gao, M.; Jáklí, A.; Panov, V. P.; Vij, J. K.; Imrie,

- C. T.; Tamba, M. G.; Mehl, G. H.; et al. Nematic Twist-Bend Phase with Nanoscale Modulation of Molecular Orientation. *Nat. Commun.* **2013**, *4*, 2635.
- (59) Meyer, R. B. Structural Problems in Liquid Crystal Physics. In *Molecular Fluids*; Balian, R., Weil, G., Eds.; Gordon and Breach: New York, 1976; pp 273–373.
- (60) Dozov, I. On the Spontaneous Symmetry Breaking in the Mesophases of Achiral Banana-Shaped Molecules. *Europhysics Letters (EPL)*, 2001, *56*, 247–253.
- (61) Tripathi, C. S. P.; Losada-Pérez, P.; Glorieux, C.; Kohlmeier, A.; Tamba, M. G.; Mehl, G. H.; Leys, J. Nematic-Nematic Phase Transition in the Liquid Crystal Dimer CBC9CB and Its Mixtures with 5CB: A High-Resolution Adiabatic Scanning Calorimetric Study. *Phys. Rev. E - Stat. Nonlinear, Soft Matter Phys.* **2011**, *84*, 041707.
- (62) Panov, V. P.; Nagaraj, M.; Vij, J. K.; Panarin, Y. P.; Kohlmeier, A.; Tamba, M. G.; Lewis, R. A.; Mehl, G. H. Spontaneous Periodic Deformations in Nonchiral Planar-Aligned Bimesogens with a Nematic-Nematic Transition and a Negative Elastic Constant. *Phys. Rev. Lett.* **2010**, *105*.
- (63) Henderson, P. A.; Imrie, C. T. Methylene-Linked Liquid Crystal Dimers and the Twist-Bend Nematic Phase. *Liq. Cryst.* **2011**, *38*, 1407–1414.
- (64) Beguin, L.; Emsley, J. W.; Lelli, M.; Lesage, A.; Luckhurst, G. R.; Timimi, B. A.; Zimmermann, H. The Chirality of a Twist-Bend Nematic Phase Identified by NMR Spectroscopy. *J. Phys. Chem. B* **2012**, *116*, 7940–7951.
- (65) Panov, V. P.; Balachandran, R.; Vij, J. K.; Tamba, M. G.; Kohlmeier, A.; Mehl, G. H. Field-Induced Periodic Chiral Pattern in the N_x Phase of Achiral Bimesogens. *Appl. Phys. Lett.* **2012**, *101*.
- (66) Chen, D.; Porada, J. H.; Hooper, J. B.; Klitnick, A.; Shen, Y.; Tuchband, M. R.; Korblova, E.; Bedrov, D.; Walba, D. M.; Glaser, M. a; et al. Chiral Heliconical Ground State of Nanoscale Pitch in a Nematic Liquid Crystal of Achiral Molecular Dimers. *Proc. Natl. Acad. Sci. U. S. A.* **2013**, *110*, 15931–15936.
- (67) Gorecka, E.; Salamonczyk, M.; Zep, A.; Pocięcha, D.; Welch, C.; Ahmed, Z.; Mehl, G. H. Do the Short Helices Exist in the Nematic TB Phase? *Liq. Cryst.* **2015**, *42*, 1–7.

- (68) Hands, P. J. W. Introduction to liquid crystals <http://www-g.eng.cam.ac.uk/CMMPE/lcintro.html>.
- (69) Singh, S.; Dunmur, D. A. *Liquid Crystals: Fundamentals*; World Scientific, 2002.
- (70) Czarniecka, K.; Samulski, E. T. Polypeptide Liquid Crystals: A Deuterium NMR Study. *Mol. Cryst. Liq. Cryst.* **1981**, *63*, 205–214.
- (71) Lesot, P.; Aroulanda, C.; Zimmermann, H.; Luz, Z. Enantiotopic Discrimination in the NMR Spectrum of Prochiral Solutes in Chiral Liquid Crystals. *Chem. Soc. Rev.* **2015**, *44*, 2330–2375.
- (72) Hoffmann, A.; Vanakaras, A. G.; Kohlmeier, A.; Mehl, G. H.; Photinos, D. J. On the Structure of the N_x Phase of Symmetric Dimers: Inferences from NMR. *Soft Matter* **2015**, *11*, 850–855.
- (73) de Gennes, P. G.; Prost, J. *The Physics of Liquid Crystals*; International Series of Monographs on Physics; Clarendon Press, 1995.
- (74) Peroukidis, S. D.; Vanakaras, A. G.; Photinos, D. J. Molecular Simulation of Hierarchical Structures in Bent-Core Nematic Liquid Crystals. *Phys. Rev. E* **2011**, *84*, 010702.
- (75) Barnes, P. J.; Douglass, A. G.; Heeks, S. K.; Luckhurst, G. R. An Enhanced Odd-Even Effect of Liquid Crystal Dimers Orientational Order in the α,ω -bis(4'-Cyanobiphenyl-4-Yl)alkanes. *Liq. Cryst.* **1993**, *13*, 603–613.
- (76) Transition Temperatures Obtained from G. H. Mehl via DSC Experiment.
- (77) Luz, Z.; Poupko, R.; Samulski, E. Deuterium NMR and Molecular Ordering in the Cholesteryl Alkanoates Mesophases. *J. Chem. Phys.* **1981**, *74*, 5825.
- (78) Guo, W.; Fung, B. M. Determination of the Order Parameters of Liquid Crystals from Carbon-13 Chemical Shifts. *J. Chem. Phys.* **1991**, *95*, 3917.
- (79) Fung, B. M. Liquid Crystalline Samples: Carbon-13 NMR. In *Encyclopedia of Magnetic Resonance*; 2007.

- (80) Vanakaras, A. G.; Photinos, D. J. A Molecular Theory of the Nematic-Nematic Phase Transitions in Mesogenic Dimers. **2015**.
- (81) Sheiko, S. S.; Sumerlin, B. S.; Matyjaszewski, K. Cylindrical Molecular Brushes: Synthesis, Characterization, and Properties. *Prog. Polym. Sci.* **2008**, *33*, 759–785.
- (82) Li, Y.; Nese, A.; Lebedeva, N. V.; Davis, T.; Matyjaszewski, K.; Sheiko, S. S. Molecular Tensile Machines: Intrinsic Acceleration of Disulfide Reduction by Dithiothreitol. *J. Am. Chem. Soc.* **2011**, *133*, 17479–17484.
- (83) Li, Y.; Nese, A.; Matyjaszewski, K.; Sheiko, S. S. Molecular Tensile Machines: Anti-Arrhenius Cleavage of Disulfide Bonds. *Macromolecules* **2013**, *46*, 7196–7201.
- (84) Burdyńska, J.; Li, Y.; Aggarwal, A. V.; Höger, S.; Sheiko, S. S.; Matyjaszewski, K. Synthesis and Arm Dissociation in Molecular Stars with a Spoked Wheel Core and Bottlebrush Arms. *J. Am. Chem. Soc.* **2014**.
- (85) Lee, H. Il; Matyjaszewski, K.; Sherryl, Y. S.; Sheiko, S. S. Hetero-Grafted Block Brushes with PCL and PBA Side Chains. *Macromolecules* **2008**, *41*, 6073–6080.
- (86) Miyake, G. M.; Piunova, V. A.; Weitekamp, R. A.; Grubbs, R. H. Precisely Tunable Photonic Crystals from Rapidly Self-Assembling Brush Block Copolymer Blends. *Angew. Chemie - Int. Ed.* **2012**, *51*, 11246–11248.
- (87) Sveinbjornsson, B. R.; Weitekamp, R. A.; Miyake, G. M.; Xia, Y.; Atwater, H. A.; Grubbs, R. H. Rapid Self-Assembly of Brush Block Copolymers to Photonic Crystals. *Proceedings of the National Academy of Sciences*, 2012, *109*, 14332–14336.
- (88) Banquy, X.; Burdyńska, J.; Lee, D. W.; Matyjaszewski, K.; Israelachvili, J. Bioinspired Bottle-Brush Polymer Exhibits Low Friction and Amontons-like Behavior. *J. Am. Chem. Soc.* **2014**, *136*, 6199–6202.
- (89) Zhang, Y.; Costantini, N.; Mierzwa, M.; Pakula, T.; Neugebauer, D.; Matyjaszewski, K. Super Soft Elastomers as Ionic Conductors. *Polymer (Guildf)*. **2004**, *45*, 6333–6339.
- (90) Pakula, T.; Zhang, Y.; Matyjaszewski, K.; Lee, H. il; Boerner, H.; Qin, S.; Berry, G. C. Molecular Brushes as Super-Soft Elastomers. *Polymer (Guildf)*. **2006**, *47*, 7198–7206.

- (91) Neugebauer, D.; Zhang, Y.; Pakula, T.; Sheiko, S. S.; Matyjaszewski, K. Densely-Grafted and Double-Grafted PEO Brushes via ATRP. A Route to Soft Elastomers. *Macromolecules* **2003**, *36*, 6746–6755.
- (92) Pietrasik, J.; Sumerlin, B. S.; Lee, H. i.; Gil, R. R.; Matyjaszewski, K. Structural Mobility of Molecular Bottle-Brushes Investigated by NMR Relaxation Dynamics. *Polymer (Guildf)*. **2007**, *48*, 496–501.
- (93) Neugebauer, D.; Zhang, Y.; Pakula, T.; Matyjaszewski, K. PDMS-PEO Densely Grafted Copolymers. *Macromolecules* **2005**, *38*, 8687–8693.
- (94) Gao, H.; Matyjaszewski, K. Synthesis of Molecular Brushes by “Grafting onto” Method: Combination of ATRP and Click Reactions. *J. Am. Chem. Soc.* **2007**, *129*, 6633–6639.
- (95) Beers, K. L.; Gaynor, S. G.; Matyjaszewski, K.; Sheiko, S. S.; Moeller, M. Synthesis of Densely Grafted Copolymers by Atom Transfer Radical Polymerization. *Macromolecules* **1998**, *31*, 9413–9415.
- (96) Cheng, G.; Böker, A.; Zhang, M.; Krausch, G.; Müller, A. H. E. Amphiphilic Cylindrical Core-Shell Brushes via a “Grafting from” Process Using ATRP. *Macromolecules* **2001**, *34*, 6883–6888.
- (97) Börner, H. G.; Beers, K.; Matyjaszewski, K.; Sheiko, S. S.; Möller, M. Synthesis of Molecular Brushes with Block Copolymer Side Chains Using Atom Transfer Radical Polymerization. *Macromolecules* **2001**, *34*, 4375–4383.
- (98) Matyjaszewski, K.; Xia, J. Atom Transfer Radical Polymerization. *Chem. Rev.* **2001**, *101*, 2921–2990.
- (99) Matyjaszewski, K. Atom Transfer Radical Polymerization (ATRP): Current Status and Future Perspectives. *Macromolecules* **2012**, *45*, 4015–4039.
- (100) Matyjaszewski, K.; Tsarevsky, N. V. Macromolecular Engineering by Atom Transfer Radical Polymerization. *Journal of the American Chemical Society*, 2014, *136*, 6513–6533.
- (101) Abragam, A. *The Principles of Nuclear Magnetism*; International series of

monographs on physics; Clarendon Press, 1961.

- (102) Dingemans, T. High-Temperature Thermosets. In *Polymer Science: A Comprehensive Reference, 10 Volume Set*; Matyjaszewski, K., Moller, M., Eds.; Elsevier B.V.: Amsterdam, 2012; Vol. 5, pp 753–769.
- (103) Knijnenberg, A.; Weiser, E. S.; StClair, T. L.; Mendes, E.; Dingemans, T. J. Synthesis and Characterization of Aryl Ethynyl Terminated Liquid Crystalline Oligomers and Their Cured Polymers. *Macromolecules* **2006**, *39*, 6936–6943.
- (104) Mark, J. E. *Physical Properties of Polymers Handbook*; 1990.
- (105) Hartmann, S. R.; Hahn, E. L. Nuclear Double Resonance in the Rotating Frame. *Phys. Rev.* **1962**, *128*, 2042–2053.
- (106) Roberts, C. C.; Apple, T. M.; Wnek, G. E. Curing Chemistry of Phenylethynyl-Terminated Imide Oligomers: Synthesis of ¹³C-Labeled Oligomers and Solid-State NMR Studies. *J. Polym. Sci. Part A Polym. Chem.* **2000**, *38*, 3486–3497.
- (107) Veeman, W. S. Carbon-13 Chemical Shift Anisotropy. *Prog NMR Spec* **1984**, *16*, 193–235.
- (108) Pines, A.; Gibby, M. G.; Waugh, J. S. Proton-Enhanced Nuclear Induction Spectroscopy ¹³C Chemical Shielding Anisotropy in Some Organic Solids. *Chem. Phys. Lett.* **1972**, *15*, 373–376.
- (109) Dingemans, T.; Photinos, D. J.; Samulski, E. T.; Terzis, A. F.; Wutz, C. Ordering of Apolar and Polar Solutes in Nematic Solvents. *J. Chem. Phys.* **2003**, *118*, 7046.